COMPOSITIONAL HETEROGENEITY IN BIOLOGICALLY RELEVANT MEMBRANE MODELS

A Dissertation
Presented to the Faculty of the Graduate School
of Cornell University
In Partial Fulfillment of the Requirements for the Degree of
Doctor of Philosophy

by
Robin Smith Petruzielo
January 2013

COMPOSITIONAL HETEROGENEITY IN BIOLOGICALLY RELEVANT MEMBRANE MODELS

Robin Smith Petruzielo

Cornell University 2013

Lateral organization of the cellular plasma membrane promotes biological function by permitting regulation of cellular processes. Evidence now supports the hypothesis that the coexistence of a variety of lipid molecules, with different melting temperatures and acyl chain lengths, contribute to this lateral organization by forming lipid rafts, nanoscale domains with distinct biophysical properties. Phase separation into immiscible micron-sized domains is readily observed in model membranes, chemically simplified lipid mixtures that have been studied under equilibrium conditions to understand how composition and temperature affect domain properties. As lipid domains have yet to be imaged directly in live resting cells, the relevance of model membranes is uncertain.

We have focused on characterizing the biologically relevant outer leaflet membrane model brain sphingomyelin (bSM)/1-palmitoyl-2-oleoyl-*sn*-glycero-3-phosphocholine (POPC)/cholesterol (Chol) in which nanoscale domains challenge conventional imaging techniques. We have determined the temperature-dependent ternary phase diagrams for bSM/POPC/Chol and bSM/1,2-dioleoyl-*sn*-glycero-3-phosphocholine (DOPC)/Chol using Förster resonance energy transfer (FRET) and differential scanning calorimetry, and we have confirmed the biologically relevant liquid-disordered (Ld) and liquid-ordered (Lo) coexistence region using electron spin

resonance spectroscopy. We have determined that the size of coexisting Ld+Lo domains in bSM/POPC/Chol is 2-6 nm radius using FRET and small-angle neutron scattering.

Ultimately, this careful characterization of model membrane will serve as a starting point for investigating the influence of peptides on domain size and other biophysical properties. Rafts can be stabilized to form larger platforms through protein-protein and protein-lipid interactions. Understanding how these domains form, grow, and stabilize in model systems is a first step toward elucidating their roles in important membrane-mediated processes.

BIOGRAPHICAL SKETCH

Robin Smith Petruzielo was born in upstate New York and grew up near Philadelphia. The oldest of three, she inadvertently served as a decisive role model: both younger siblings studied physics in college and are currently pursuing doctoral degrees. Robin attended Swarthmore College where she received a B.A. in physics.

In 2008, she joined Professor Gerald Feigenson's laboratory at Cornell University where she has used fluorescence and electron spin resonance spectroscopy to study models of the cell membrane. In November 2011, she began a collaboration to investigate lipid phase behavior using small angle neutron scattering and differential scanning calorimetry at Oak Ridge National Laboratory.

To my family

ACKNOWLEDGMENTS

I extend a heartfelt thank you to my graduate research advisor, Prof. Gerald Feigenson, for the opportunity to do exciting research. I have learned so much from Jerry about designing scientific questions and conducting experimental research. His optimism and perseverance inspire me to keep trying when experiments fail or results seem ambiguous. He believes in me.

I thank my collaborator and former labmate Dr. Fred Heberle for helping with massive FRET data sets and introducing me to neutron scattering. Fred was always available for discussing new ideas. He patiently endured many late-night calorimetry sample changes and elaborate schemes for maximizing neutron beam time.

I thank Drs. John Katasaras and Robert Standaert for lively research discussions at Oak Ridge. I am indebted to Paul Drazba for running many calorimetry samples, helping prepare sphingomyelin samples, and hiking up the hill to refill MQ water jugs (sometimes in the middle of the night). I thank Prof. Jack Freed and Dr. Boris Dzikovski of ACERT for assisting with ESR experiments, providing spectral simulation software, and discussing results and future directions.

I very much appreciate the support of my labmate Dr. Lynda Goh who was a valuable sounding board throughout my time in the lab, especially as we simultaneously navigated the thesis writing process. She was a great support, both in the lab and beyond. I am indebted to my labmate Sarah Kim, the first undergraduate student to learn FRET techniques in our lab, and the first research student I mentored. I’ve learned so much from guiding her project and (attempting to) answer her many insightful questions. I have since begun mentoring Mary Kim and Sanjula Wickramasinghe and working with additional students including Susan Duan, Shu Wang, and Thomas Torng. I am grateful to them for discussing their work with me (especially Susan, who had to endure my many questions about her work both at home and in the lab). I have benefited from discussions with my current labmates David Ackerman, Jon Amazon, and Tatyana Konyakhina. David and Jon frequently entertained my enthusiastic yet often crazy ideas for how their molecular dynamics and coarse-grained simulations could relate to my experimental studies.

This work would not have been possible without the support of my former labmates: Nelson Morales always had a kind word and an empathetic ear, and Jing Wu helped prepare samples for a large experiment. I also thank former lab members Dr. Thalia Mills and Prof. Jeff Buboltz for lively discussions. Although I never worked with them in the lab, I wish I had. I've been grateful for their lively advice.

I extend much appreciation to my committee members Prof. Sol Gruner, Prof. James Sethna, and Prof. Carl Franck for a critical reading of this thesis.

I thank the following sources of support for this thesis work: research awards NIH R01 GM077198 and NSF MCB 0842839 to G.W. Feigenson, Oak Ridge National Laboratory, graduate fellowships from AT&T and NDSEG, research awards from Sigma Xi, and travel funding from the Cornell University Graduate School.

Thanks to my undergraduate thesis advisor, Prof. Carl Grossman. All of my Swarthmore professors and Fulbright research advisors were encouraging. I am grateful to them for suggesting I choose Cornell for graduate school. I thank my AT&T research mentor Dr. Sheri Woodward who provided valuable perspective for navigating career options.

My love and thanks to my family. My parents have made many sacrifices to further my education. I can always count on my sister Hillary for a much needed down-to-earth perspective. My brother Mitch(ie) has been especially encouraging and excited about my work. Both the Smith and Petruzielo families have been supportive during my graduate research. Thank you to my husband Frank for believing in me.

TABLE OF CONTENTS

LIST OF FIGURES

LIST OF TABLES

LIST OF ABBREVIATIONS

2θ	scattering angle
16-DSA	16-doxyl-stearic acid
16-PC	1-palmitoyl-2-(16-doxyl stearoyl) phosphatidylcholine
14-PC	1-palmitoyl-2-(14-doxyl stearoyl) phosphatidylcholine
α	domain area fraction
AFM	atomic force microscopy
BoDIPY-PC	16:0, BoDIPY-PC, 2-(4,4-difluoro-5,7-dimethyl-4-bora-3a,4a-diaza-s-indacene- 3-pentanoyl)-1-hexadecanoyl-sn-glycero-3-phosphocholine
bSM	porcine brain sphingomyelin
Chol	cholesterol
χ_A	mole fraction of component
CW-ESR	continuous wave-ESR
DHE	Ergosta-5,7,9(11),22-tetraen- 3β-ol, dehydrogerosterol
DiI-C18:0	1,1'-dioctadecyl-3,3,3',3'-tetramethylindocarbocyanine perchlorate
DiI-C18:1	1,1'-dioleoyl-3,3,3',3'-tetramethylindocarbocyanine perchlorate
DLPC	1,2-dilauroyl-*sn*-glycero-3-phosphocholine
DMPC	1,2-dimyristoyl-sn-glycero-3-phosphocholine
DOPC	1,2-dioleoyl-*sn*-glycero-3-phosphocholine
dPOPC	deuterated POPC, POPC-d31
DPhPC	1,2-diphytanoyl-*sn*-glycero-3-phosphocholine
DPPC	1,2-dipalmitoyl-*sn*-glycero-3-phosphocholine
dPSM	deuterated PSM, PSM-d31
DQ	donor quenching
DSC	differential scanning calorimetry
DSPC	1,2-distearoyl-*sn*-glycero-3-phosphocholine
E	FRET efficiency
E_{DQ}	E determined from measurements of DQ
E_{SAE}	E calculated from comparing SAE and E_{DQ} measurements
eSM	egg sphingomyelin
ESR	electron spin resonance
ESR buffer	10 mM KCl, 5 mM PIPES, and 1 mM EDTA at pH 7.0
f_D	donor fluorescence without acceptor
f_{DA}	acceptor-quenched donor quenched fluorescence
f_{SAE}	donor-excited acceptor fluorescence
FastDiO	3,3'-dilinoleyloxacarbocyanine perchlorate, DiO-C18:2
FastDiI	1,1'-dilinoleyl-3,3,3',3'-tetramethylindocarbocyanine perchlorate, DiI-C18:2
FP-FRET	finite phase separation FRET
FRET	Förster resonance energy transfer
FRET buffer	200 mM KCl, 5 mM PIPES, and 1 mM EDTA at pH 7.0
GUV	giant unilamellar vesicles

High-Tm	high melting
I	scattering intensity
Lβ	gel phase
Ld	liquid-disordered phase
Lo	liquid-ordered phase
Low-Tm	low melting
LR-DOPE	lissamine rhodamine 18:1,18:1-PE
λ	neutron wavelength
K_A	acceptor partition coefficient
K_D	donor partition coefficient
Kp	partition coefficient
MD	molecular dynamics
MLV	multilamellar vesicles (average lamellarity >2)
MOMD	microscopic order with macroscopic disorder
Pβ'	tilted ripple phase
PC	phosphatidylcholine
PE	phosphatidylethanolamine
PLV	paucilamellar vesicles (average lamellarity between 1 and 2)
POPC	1-palmitoyl-2-oleoyl-*sn*-glycero-3-phosphocholine
PM	plasma membrane
PSM	palmitoyl sphingomyelin, N-palmitoyl-D-*erythro*-sphingosylphosphorylcholine
q	scattering vector
Q	total scattered intensity, $Q=\int Iq^2dq$
R_0	Förster distance
$R\perp$	rotational diffusion parameter for diffusion perpendicular to the bilayer normal
$R\|\|$	rotational diffusion parameter for diffusion parallel to the bilayer normal
REE	region of enhanced efficiency
RRE	region of reduced efficiency
RSE	rapid solvent exchange
S_{Lo}	mole fraction of Lo phase
S_0	ESR order parameter
SANS	small-angle neutron scattering
SAE	sensitized acceptor emission
SDD	sample-to-detector distance
SLD	scattering length density
SM	sphingomyelin
SSM	stearoyl sphingomyelin, N-stearoyl-D-*erythro*-sphingosylphosphorylcholine
SOPC	1-stearoyl-2-oleoyl-*sn*-glycero-3-phosphocholine
SP-FRET	steady-state probe-partitioning FRET
TLC	thin-layer chromatography
Tm	melting or main chain transition temperature

tPA	*trans*-parinaric acid
ULV	unilamellar vesicle
χ_A	mole fraction of component
ξ	correlation length

Chapter 1:
Introduction

Portions of this chapter appear in the following review article which was invited for publication in *Chemistry and Physics of Lipids*: Jianjun Pan, Frederick A. Heberle, Robin S. Petruzielo, John Katsaras. The Usage of Small-Angle Neutron Scattering in Exploiting Nanoscopic Lipid Domains. *In preparation* (2013).

1.1 OVERVIEW

This work focuses on determining temperature-dependent phase behavior and domain sizes in the liquid coexistence region for the biologically relevant ternary lipid mixture brain sphingomyelin (bSM)/1-palmitoyl-2-oleoyl-*sn*-glycero-3-phosphocholine (POPC)/cholesterol (Chol). This mixture models the outer leaflet of the mammalian plasma membrane (PM).

The PM is a complex mixture comprising proteins, hydrophobic sterols, and amphiphilic lipids. The lipid raft hypothesis ascribes an active role for lipid heterogeneities in lateral organization that promotes functions in the mammalian PM. These heterogeneities include preferential sphingomyelin (SM) and Chol association that can compartmentalize the PM into ordered and disordered regions, separating proteins based on preferential interaction with certain lipids. Rafts continue to generate controversy, as reported sizes and lifetimes vary with experimental techniques, many of which affect the native membrane state.

Chemically simplified model systems with well-defined lipid compositions are powerful tools for elucidating the thermodynamics governing lateral heterogeneity of membrane lipids. Model membranes exhibit lateral segregation of liquid-disordered (Ld) and liquid-ordered (Lo) phases at certain compositions and temperatures.

Determining the phase diagrams of model systems aids in understanding lipid-lipid interactions.

As rafts are now considered to be nanoscale assemblies [1], the relevance of ternary lipid mixtures that exhibit nanoscopic domains is heightened. In this work, we tackle the most biologically relevant ternary mixture bSM/POPC/Chol, using a variety of techniques to confirm Ld+Lo heterogeneity, solve the temperature-dependent phase diagram, and measure the sizes of coexisting liquid domains.

In this chapter, we provide background and motivation for the work presented in Chapters 2-4. We describe lipids, track development of the raft model, introduce lipid bilayer phase behavior, and survey studies on outer leaflet model membranes. This chapter ends by describing the historical evolution of work presented in this thesis.

1.2 LIPIDS

The three main classes of lipids relevant to this work include glycerophospholipids, sphingolipids, and sterols [2]. Lipids are amphiphilic molecules with a hydrophilic headgroup and hydrophobic fatty acid or acyl chains. They are classified according to headgroup, chain lengths, and degree/location of unsaturation. Glycerophospholipids have a three-carbon glycerol backbone, while sphingolipids have a sphingosine backbone that includes a long unsaturated hydrocarbon chain. Sphingosine was named in 1884 after the Sphinx, a Greek mythological creature, due to its enigmatic nature [3,4]. The most ubiquitous sphingolipid in mammalian cells, SM has a phosphocholine headgroup like POPC and other phosphatidylcholine (PC) lipids used in these studies.

Less polar than lipids, sterols have a planar hydrophobic structure of four rings and hydroxyl group (-OH). The PM contains 30-40 mole% of the sterol Chol [5]. Chol is oriented in the membrane with its hydroxyl group facing toward the aqueous boundaries and the planar ring structures in the hydrophobic region.

1.2.1 Lyotropic Phases

In aqueous solution, amphiphilic lipids spontaneously organize to orient the polar headgroups toward water and protect the hydrophobic hydrocarbon tails from water. The resulting structural configurations depend on the temperature and intrinsic lipid curvature (relative size of the headgroup and tails) [6]. The most biologically relevant structure is the bilayer, which comprises two lipid layers called leaflets. In the bilayer, the leaflets are arranged such that the acyl chain regions face each other, and the headgroups face the aqueous solution. Model lipid mixtures can be prepared in different structural models, including monolayers, planar bilayers, and freely suspended bilayers that consist of multilamellar, paucilamellar, and unilamellar vesicles of various sizes, ranging from giant unilamellar vesicles (10-50 μm diameter) to smaller 60 nm diameter vesicles.

1.2.2 Plasma Membrane Lipid Composition

The bilayer structure of the plasma membrane was first proposed in 1925 [7]. The distribution of lipids is asymmetric across the two leaflets of the mammalian plasma membrane [8–10]. Neutral species including SM and PC are found in the outer leaflet, while phosphatidylethanolamine and negatively charged lipids including phosphatidylserine and phosphatidylinsositol are found in the inner leaflet [11]. Chol is approximately equally distributed between the two leaflets and comprises 10 to 40 mol% of the mammalian plasma membrane [5,12].

Lipids in the outer leaflet can be divided into three categories: Chol, and two lipid categories divided based on their fluidity at ambient temperature. High-melting (high-Tm) lipids including SM undergo a transition from gel to fluid phase around or above physiological temperatures. Low-Tm lipids in the outer leaflet are fluid at ambient temperature. Among the most abundant lipids in the plasma membrane, low-Tm PC's account for about 50% of the outer leaflet [13]. A ternary model for the cell membrane outer leaflet can be constructed using one component from each of these three categories.

Sterols and sphingolipids play important structural roles in the membrane and have been implicated in the regulation of membrane trafficking [14]. Chol influences fluidity and permeability of membranes *in vitro* [15] and *in vivo* [16].

Aside from lipids, proteins are the other major component of the PM. The protein concentration in the bilayer varies from 18 to 76% by weight [12] and is often quoted to be 50% by weight. However, much of this weight is outside the membrane. Considering this, protein accounts for only 10 to 20% of the bilayer mass in the region between lipid headgroups [17]. Proteins interact with membrane in different ways: they can span the bilayer, insert into one leaflet, or interact peripherally via lipid headgroups or other proteins. Proteins in the membrane also serve as cytoskeletal anchors [18,19].

1.3 HISTORY OF LIPID RAFTS

1.3.1 Fluid Mosaic Model

In 1972, Singer and Nicholson proposed the fluid mosaic model in which they postulated that the lipid bilayer that makes up the PM is a homogenous, relatively inert fluid sea which provides a medium for protein diffusion and a substrate for protein interaction and protein-dominated processes [20]. Lipids were considered to be passive structural components, and proteins were thought to control membrane architecture and organization, possibly through interactions with the cytoskeleton.

1.3.2 Ordered Lipid Clusters

Soon after, clusters of lipids were proposed to exist in the membrane, based on the effects of temperature on membrane behavior [21]. The clusters were suggested to be an ordered fluid state [22] relative to surrounding disordered liquid crystalline lipids. Karnovsky and coworkers formalized the idea of membrane lipid domains in 1982 [23] after observing heterogeneity in fluorescence lifetime decay. They proposed several lines of inquiry still being investigated today, including the forces behind the formation, maintenance, and fluctuation of lipid domains.

Interest in the roles of lipids and sterols in lateral organization and chemical functions of the PM followed these observations. Sphingolipids and Chol were found to be enriched in apical membranes of epithelial cells [24]. It was also observed that protein partitioning and function is affected by lipid composition in model systems [25,26]. Brown and Rose found certain proteins localized with Chol and sphingolipids in detergent-resistant membrane domains [27]. Liquid-liquid immiscibility in model mixtures from ternary lipid systems was first reported in 1996 [28].

1.3.3 Raft Hypothesis

These findings from both biological studies of the PM and physical chemistry studies of model membranes led to the lipid raft description of the PM [29,30]. The raft hypothesis postulated that the PM is organized into functional domains called rafts. Rafts were suggested to have different composition (due to preferential SM and Chol association) from the bulk lipids, and actively participate in protein organization and function by influencing protein diffusion and local concentration. Analysis of lipids by mass spectrometry has elucidated the lipid composition of rafts compared to the bulk PM: SM levels are elevated by 50% [31], Chol levels are double [32], and PC levels are similar in rafts and bulk PM.

1.3.4 Raft Functions

Many cellular functions have been associated with lateral heterogeneity of lipid composition in the PM, including cell signaling pathways [33,34], protein sorting [35], modulation of protein activity [36], and cytoskeletal connections [37].

1.3.5 Comparing Rafts with Model Membrane Heterogeneity

When lipid rafts are described as coexisting liquid-disordered (Ld) and liquid-ordered (Lo) domains, useful connections can be drawn with model studies to elucidate relevant intermolecular interactions. However, some discrepancies exist. Some transmembrane proteins that prefer raft phase in cells are excluded from the Lo phase in model studies [38]. Intermediate between live cell and model studies are membrane preparations from cellular PM's in the form of giant plasma membrane vesicles [39] or plasma membrane spheres [40] that contain membrane proteins and lipids but no cytoskeleton attachment. These studies find macroscopic fluid phase separation, suggesting that nanoscale heterogeneity may exist in the native cellular

PM. However, these results find less distinction between Ld and Lo phases in plasma membrane spheres than in model membranes [41]. The Lo phase is proposed to be different in model membranes compared to cell plasma membranes, as there may be a wider range of conformational and positional orders that are modulated by both lipids in proteins in cells than in model systems [42].

Developing model systems which are more biologically relevant means finding those that have more similar Ld and Lo phases, perhaps more similar in composition or in relevant properties such as order. Our bSM/POPC/Chol studies are promising for relevance to the PM, given that we find the order is more similar between Ld and Lo phases (Chapter 3), and the sizes of coexisting domains are 2-6 nm (Chapter 2).

1.3.6 Raft Definitions

Physical definitions of rafts have varied, depending on the system observed and the measurement made. Rafts are now considered to be a heterogeneous collection of domains with diverse protein and lipid compositions, and varied temporal stability. According to the lipid raft definition from the 2006 Keystone Symposium on Lipid Rafts and Cell Function, ‘Lipid rafts are small (10-200 nm), heterogeneous, highly dynamic, sterol- and sphingolipid-enriched domains that compartmentalize cellular processes. Small rafts can sometimes be stabilized to form larger platforms through protein-protein and protein-lipid interactions’ [43]. To unify raft observations, it is important to understand how different preparation and measurement conditions affect the native membrane state, and there is more to learn from thermodynamics of lipid mixtures in bilayer membranes.

1.3.7 Rafts as Transient, Nanoscale Assemblies

As native cells do not display macroscopic domains, rafts are now thought to be nanoscale ordered regions of the PM. Rafts are likely transient assemblies including sphingolipids, Chol, and some proteins that can coalesce to form more stable platforms that exclude certain proteins [1].

Evidence for nanoscale heterogeneities in the cellular PM is accumulating. Sharma and coworkers used homo and hetero-FRET to detect < 5nm clusters of particular proteins in the PM [44]. FRET between fluorescent lipid analogs in the PM outer leaflet revealed nanoscale heterogeneity in cells [45]. Electron spin resonance studies in live cells evidenced order and rotational diffusion parameters consistent with distinct Lo and Ld phases [46].

New tools are proving helpful [47]. Super resolution microscopy methods including fluorescence photoactivation localization microscopy (FPALM) detect nanoscale heterogeneities in cells [48]. Stimulated emission depletion (STED) far-field nanoscopy inferred nanoscopic domains in live cells by detection of sphingolipids with hindered diffusion [49].

1.3.8 Need for Model Studies

Progress has been made defining lipid and protein constituents of rafts, but it is still not well understood how these constituents work together to generate and maintain lipid domains in the PM. Model studies suggest that PM lipids have an underlying propensity to phase separate, but this behavior is likely modulated by proteins in the PM [50]. Indeed, the many protein-lipid interactions make it difficult to determine how the cellular PM achieves compartmentalization of components.

The PM could be close to a transition temperature for phase separation [51] or close to a critical point, with nanodomains as critical fluctuations (Veatch 2008, Honerkamp-Smith 2009). However, thermal regulation of rafts would not permit selective control of domain size for particular cell functions [52]. This points instead to modulation of local lipid composition. Model studies with well-defined, chemically simplified compositions provide a guide to possible mixing phenomena that may occur in the cellular PM. It is also possible that cytoskeletal attachments could regulate raft size [53,54]. In addition, transmembrane proteins could promote compartmentalization [1,19]. The sizes of detected heterogeneities often depend on the measurement technique used and the system studied. Better results are achieved by probing multiple temporal and spatial scales with minimally perturbative methods.

1.4 LIPID PHASES

1.4.1 Order Parameters

In a given lyotropic phase, lipids exist in various thermotropic phases depending on temperature and composition. These phases are distinguished by several order parameters including positional order and chain order. Positional order describes the lateral mobility of lipids within a leaflet and is quantified with the translational diffusion coefficient, while chain order is described by the degree of conformational order experienced by the acyl chains [55]. Positional order also relates to the lateral packing density of lipids, as described by the molecular area (area per lipid) perpendicular to the bilayer normal.

Conformation and chain orientational order can be segmental in referring to one C-C bond or spatially averaged to give the ratio of trans to gauche isomers in the

C-C bonds in the hydrocarbon chain. The measured chain order depends on the spatial and temporal resolution of the method employed. In the ESR studies described for Ld and Lo phase lipid bilayers (Chapter 3), the whole- chain order parameter *S* refers to the orientation of the lipid with respect to the bilayer normal [56]. The dynamic parameters $R_\perp$ and $R_\|$ describe the motion of the spin-label assuming axial symmetry where $R_\|$ describes the rotational rate around the long axis of the molecule and $R_\perp$ gives the rotational rate around an axis perpendicular to the long axis of the molecule [57].

1.4.2 Single-Lipid Phases

Pure lipids may exist in gel or liquid-disordered (Ld) phases. The gel or solid-ordered (Lβ) phase is characterized by tight, regular packing of acyl chains. At room temperature, lipids with long (16 or more carbons), fully saturated acyl chains are in the Lβ phase. The chains are elongated, so each lipid has a minimal area per lipid. Some lipids exhibit distinct gel phases with different degrees of order. For example, sphingomyelin can exhibit the Pβ' phase which exists as a pretransition between the main chain transition from Lβ to Ld upon heating [58]. This phase is characterized by rippling of the bilayer and a net tilt of the molecular axis relative to the bilayer normal [59,60].

The melting or main chain transition temperature (Tm) characterizes the transition from Lβ phase to liquid-disordered phase (Lα or Ld). Unsaturated or short chain saturated lipids exhibit Ld phase at room temperature. This fluid phase is distinguished by lateral mobility of lipids and conformational freedom of chains, due to low positional and conformational orders.

The diffusion coefficient is about 10^{-11} to 10^{-10} cm^2/s at 25°C in the Lβ phase and three orders of magnitude faster in the Ld phase [61]. The area per lipid for lipids in Ld phase is generally 1.2 to 1.4 times larger than in gel phase. For example, the area per lipid for bSM is 50 $Å^2$ in gel phase and 60 $Å^2$ in Ld phase [62].

1.4.3 Liquid-Ordered Phase

The liquid-ordered (Lo) phase can be formed from Lβ or Ld phases upon addition of Chol. First named by Ipsen in 1987 [63], the Lo phase is characterized by the low positional order of the Ld phase and the high chain order of the Lβ phase. The diffusion coefficient for the Lo phase is about two to three times slower than for the Ld phase, approximately 10^{-9} cm^2/s at 25°C [64]. Lo phase forms from Lβ phase when more than 10% Chol is added [65]. For several saturated chain lipids, this value seems to be around 15-17% Chol [66,67].

The formation of Lo phase is consistent with lipid headgroups acting as umbrellas to shield hydrophobic Chol from water outside the bilayer [68]. This forces the acyl chains of lipids to straighten and assume all-trans conformations, leading to high conformational order (similar to the Lβ phase) while retaining fast translational diffusion (nearly comparable to the Ld phase). When Lo phase forms upon addition of Chol to saturated lipids in Lβ phase, Chol disrupts chain packing, thereby decoupling translational order from acyl chain order [63]. When Lo phase forms upon addition of Chol to unsaturated lipids in Ld phase, van der Waals interactions between Chol and the lipid acyl chains cause the chains to adopt all-trans conformational order. As a result, lipid chains are more ordered in the Lo than Ld phase, and the bilayer is thicker

[69]. The Lo phase is often correlated with rafts in the cellular PM, but the connections may not be direct [41].

1.5 PHASE SEPARATION IN LIPID MIXTURES

1.5.1 Binary Systems

Phase diagrams for binary systems including Chol and gel phase lipids offer evidence for coexisting Lo and gel phases below optical resolution [65]. In contrast, no Ld+Lo phase separation is observed for Chol and PC lipids with an unsaturation in each chain such as DOPC (1,2-dioleoyl-*sn*-glycero-3-phosphocholine) [70]. Instead, a gradual increase in chain order occurs as Chol stiffens the Ld phase [71], resulting in a gradual change from Ld to Lo phase as Chol is added. Some controversy exists regarding possible Ld+Lo coexistence for binary systems of Chol and lipids with mixed acyl chains, such as POPC (1-palmitoyl-2-oleoyl-*sn*-glycero-3-phosphocholine) and SOPC (1-stearoyl-2-oleoyl-*sn*-glycero-3-phosphocholine). Some evidence suggests Ld+Lo coexistence in SOPC/Chol [72] and POPC/Chol binary mixtures [73,74]; others, including our work in Chapter 2, suggest a gradual transition from Ld to Lo phase without Ld+Lo phase coexistence [75].

1.5.2 Ternary Systems

Silvius and coworkers first detected Ld+Lo phase coexistence in ternary mixtures of Chol with high- and low-melting lipids [28]. In the Ld+Lo coexistence region, they found that the Lo phase is enriched in the high-melting lipid and Chol, consistent with detection of rafts in the PM. Using fluorescence microscopy imaging of fluorescent lipid analogs, Korlach and coworkers detected coexisting phases in giant unilamellar vesicles (GUVs) prepared from various ternary mixtures [76].

1.5.2.1 Macroscopic Phase Separation

The first observations of micron-sized coexisting Ld+Lo phases were reported in bSM/DOPC/Chol [77] and egg-SM (eSM)/DOPC/Chol [78]. Subsequently, macroscopic coexistence of Ld+Lo phases was found in other ternary mixtures, often including lipids such as DOPC and DPhPC (1,2-diphytanoyl-*sn*-glycero-3-phosphocholine) chosen for their poor mixing properties. Examples of ternary phase diagrams with macroscopic Ld+Lo phase coexistence include DPPC (1,2-dipalmitoyl-*sn*-glycero-3-phosphocholine)/DOPC/Chol [79], PSM (N-palmitoyl-D-*erythro*-sphingosylphosphorylcholine)/DOPC/Chol [80], DPPC/DPhPC/Chol [81], DSPC (1,2-distearoyl-*sn*-glycero-3-phosphocholine)/DOPC/Chol [67,82] and SSM(N-stearoyl-D-*erythro*-sphingosylphosphorylcholine)/DOPC/Chol [83].

1.5.2.2 Nanoscale Phase Separation

Ld+Lo coexistence regions undetectable by fluorescence microscopy were inferred from FRET measurements in DPPC/DLPC (1,2-dilauroyl-*sn*-glycero-3-phosphocholine)/Chol in the first report of nanoscopic Ld+Lo domains [66]. Further studies employed spectroscopic techniques with nanoscale resolution to investigate Ld+Lo phase coexistence in ternary systems replacing the low-melting lipid DOPC with the more biologically relevant POPC. Phase diagrams were reported for DSPC/POPC/Chol [82], PSM/POPC/Chol [73–75,80], and bSM/POPC/Chol [84].

BSM/POPC/Chol is considered to be the most biologically relevant ternary model system, due to the abundance of these lipids in the PM outer leaflet. Systems with nanoscopic heterogeneity better model the cellular PM, and studies in these systems are important for gaining clues about mechanisms responsible for the stability of nanoscale domains [85]. Consistency of results from several studies suggests that nanoscopic assembles exist in cells, but their stability and lifetimes are not known.

As with macroscopic phase separation in model membrane mixtures, it is useful to employ equilibrium thermodynamics while carefully controlling lipid composition and temperature to examine how phase behavior and domain size vary with composition and temperature in biologically relevant outer leaflet models. Proposed mechanisms for the formation and maintenance of nanoscopic heterogeneity can be refined by model and live cell studies as well as theoretical treatments. As a first step, the disparate measurements of intrinsic sizes of nanoscale Ld+Lo domains in model systems and rafts in cells must be reconciled through studies combining multiple, minimally disruptive techniques with different spatial sensitivities.

1.6 DISSERTATION SUMMARY

1.6.1 A Historical Perspective

The overall motivation of this work is to conclusively establish and characterize Ld+Lo heterogeneity in the ternary model membrane mixture bSM/POPC/Chol as a function of temperature. Prior studies have investigated heterogeneity in SM/POPC/Chol and reported widely varying results regarding the compositions at which Ld+Lo heterogeneity exists in this most biologically relevant ternary mixture [73–75,80,84]. In addition, the reported sizes of coexisting domains in bSM/POPC/Chol vary from a few nanometers [86] to several hundred nanometers [87], likely due in part to the sensitivity of this mixture to perturbations that induce domain coalescence [88].

Making comparisons between high-resolution FRET surface studies for bSM/POPC/Chol and the related system bSM/DOPC/Chol, we concluded that bSM/POPC/Chol exhibits Ld+Lo phase coexistence in the central region of the phase diagram (Chapter 2). However, with FRET results alone we could not rule out weak partitioning of fluorescent lipid analogs being responsible for little variation of FRET efficiency within the Ld+Lo phase coexistence region. We pursued several approaches for further confirmation of Ld+Lo heterogeneity in bSM/POPC/Chol. These approaches included employing a technique sensitive to smaller distance scales, establishing the ternary phase diagram, and measuring the sizes of coexisting domains.

We used electron spin resonance (ESR), a technique in which a spin probe in the hydrocarbon region of the bilayer partitions equally between Ld and Lo phases, reporting on order and dynamics in both phases (Chapter 3). Comparisons between these parameters for bSM/POPC/Chol and DOPC-containing systems with well established Ld+Lo phase coexistence supported Ld+Lo heterogeneity for bSM/POPC/Chol.

With this additional evidence for Ld+Lo phase coexistence in bSM/POPC/Chol, we determined the compositional extent of the Ld+Lo phase coexistence region by solving the ternary phase diagram (Chapter 2). Only one partial phase diagram had been reported for this system [84], and considerable discrepancy exists between phase diagrams for the related system PSM/POPC/Chol [73–75,80]. We employed differential scanning calorimetry (DSC) to determine phase boundaries at 0 and 10% Chol. Further examination of FRET surface results, including comparison of FRET efficiency at 15 and 25°C with results indicative of miscibility at high temperature, supported establishing phase boundaries for the Ld+Lo phase coexistence region. The resulting phase diagrams were very similar for bSM/DOPC/Chol and bSM/POPC/Chol, highlighting the fact that phase diagrams do not contain information about the sizes of coexisting domains.

We then employed small-angle neutron scattering (SANS), using model-independent analysis to investigate Ld+Lo phase coexistence for bSM/POPC/Chol and the closely related system PSM/POPC/Chol (Chapter 2). SANS revealed coexisting domains for PSM/POPC/Chol but not bSM/POPC/Chol. Using a limit of detection argument, we determined that coexisting Ld+Lo domains in bSM/POPC/Chol must be smaller than the 7 nm SANS detection limit, but larger than the 2 nm FRET detection limit. We then began developing experimental FRET methods for more accurately determining nanodomain sizes (Chapter 4).

These results conclusively establish phase behavior for bSM/POPC/Chol and narrow the range of possible domain radius to 2-6 nm in the Ld+Lo phase coexistence region. We also found that domain sizes vary with SM species, suggesting raft size may be varied by adjustment of local concentrations of various SM species in the mammalian PM (Chapter 5).

1.6.2 Key Results

Determining the bSM/POPC/Chol phase diagram was the most challenging and most important aspect of this work. This phase diagram for this biologically relevant ternary lipid mixture will provide a starting point for investigating mechanisms influencing phase behavior and domain sizes in systems increasingly resembling the outer leaflet of the live cell membrane.

In particular, we note several points of importance regarding the bSM/POPC/Chol phase diagram.

1. The phase diagram enabled us to determine on which compositions to focus for investigating the sizes of coexisting domains.
2. This phase diagram resolves considerable discrepancies in the literature regarding the phase behavior of SM-containing lipid mixtures.
3. Determining this phase diagram reconfirms our ability to solve ternary phase diagrams despite the existence of small domains.
4. We note similarities between the bSM/DOPC/Chol and bSM/POPC/Chol despite considerable differences in the sizes of coexisting liquid domains in these two mixtures. This is a significant and novel result.
5. This phase diagram asserts the importance of using multiple techniques with different spatial resolution and different contrast mechanisms (fluorescent lipid analogs vs. deuterated lipid species) to determine phase behavior in systems exhibiting nanoscale heterogeneity.
6. This phase diagram was solved at several temperatures. The comparison of FRET data between different lipid mixtures at temperatures exhibiting coexisting liquid phase and random mixing strengthened conclusions regarding phase behavior in bSM/POPC/Chol.
7. The phase diagram contains important information regarding the compositions of phases within the liquid coexistence region. These compositions are needed for studies investigating thickness differences between Ld and Lo phases via SANS [69] and quantitatively determining the

sizes of coexisting liquid domains via FRET (Chapter 2) and SANS [69,89]. Determining these physical properties of coexisting liquid phases is important for investigating the mechanisms responsible for the stability of nanoscale phase domains.

1.7 REFERENCES

[1] D. Lingwood, K. Simons, Lipid rafts as a membrane-organizing principle, Science, 327 (2010) 46–50.

[2] J. Berg, J. Tymoczko, L. Stryer, Biochemistry, 5th ed., W. H. Freeman, New York, 2002.

[3] J.L.W. Thudichum, A Treatise on the Chemical Constitution of Brain, Bailliere, Tindall and Cox, London, 1884.

[4] S. Spiegel, S. Milstien, Sphingosine-1-phosphate: an enigmatic signalling lipid, Nature Reviews Molecular Cell Biology, 4 (2003) 397–407.

[5] S. Takamori, M. Holt, K. Stenius, E.A. Lemke, M. Grønborg, D. Riedel, H. Urlaub, S. Schenck, B. Brügger, P. Ringler, S.A. Müller, B. Rammner, F. Gräter, J.S. Hub, B.L. De Groot, G. Mieskes, Y. Moriyama, J. Klingauf, H. Grubmüller, J. Heuser, et al., Molecular anatomy of a trafficking organelle, Cell, 127 (2006) 831–46.

[6] P.M. Chaikin, T.C. Lubensky, Principles of Condensed Matter Physics, Cambridge University Press, New York, 1995.

[7] E. Gorter, F. Grendel, On bimolecular layers of lipoids on the chromocytes of the blood, Journal of Experimental Medicine, 41 (1925) 439–443.

[8] M.S. Bretscher, Asymmetrical Lipid Bilayer Structure for Biological Membranes, Nature New Biology, 236 (1972) 11.

[9] A.J. Verkleij, R.F.A. Zwaal, B. Roelofsen, P. Comfurius, D. Kastelijn, L.L.M. van Deenen, The asymmetric distribution of phospholipids in the human red cell membrane: A combined study using phospholipases and freeze-etch electron microscopy, Biochimica Et Biophysica Acta, 323 (1973) 178–193.

[10] P.F. Devaux, Static and Dynamic Lipid Asymmetry in Cell Membranes, Biochemistry, 30 (1991) 1163–1173.

[11] V. Kiessling, C. Wan, L.K. Tamm, Domain coupling in asymmetric lipid bilayers, Biochimica Et Biophysica Acta, 1788 (2009) 64–71.

[12] H. Lodish, A. Berk, S.L. Zipursky, P. Matsudaira, D. Baltimore, J. Darnell, Molecular Cell Biology, 5th ed., W. H. Freeman and Company, New York, 2004.

[13] R.B. Gennis, Biomembranes: Molecular Structure and Function, Springer-Verlag, New York, 1989.

[14] J.T. Hannich, K. Umebayashi, H. Riezman, Distribution and Functions of Sterols and Sphingolipids, Cold Spring Harbor Perspectives in Biology, a004762 (2011).

[15] T.H. Haines, Do sterols reduce proton and sodium leaks through lipid bilayers?, Progress in Lipid Research, 40 (2001) 299–324.

[16] R. Emter, A. Heese-Peck, A. Kralli, ERG6 and PDR5 regulate small lipophilic drug accumulation in yeast cells via distinct mechanisms, FEBS Letters, 521 (2002) 57–61.

[17] M. Sheetz, Glycoprotein motility and dynamic domains in fluid plasma membranes, Annual Review of Biophysics and Biomolecular Structure, 22 (1993) 417–431.

[18] K. Murase, T. Fujiwara, Y. Umemura, K. Suzuki, R. Iino, H. Yamashita, M. Saito, H. Murakoshi, K. Ritchie, A. Kusumi, Ultrafine membrane compartments for molecular diffusion as revealed by single molecule techniques, Biophysical Journal, 86 (2004) 4075–93.

[19] A. Kusumi, C. Nakada, K. Ritchie, K. Murase, K. Suzuki, H. Murakoshi, R.S. Kasai, J. Kondo, T. Fujiwara, Paradigm shift of the plasma membrane concept from the two-dimensional continuum fluid to the partitioned fluid: high-speed single-molecule tracking of membrane molecules, Annual Review of Biophysics and Biomolecular Structure, 34 (2005) 351–78.

[20] S.J. Singer, G.L. Nicolson, The fluid mosaic model of the structure of cell membranes, Science, 175 (1972) 720–31.

[21] A.G. Lee, N.J. Birdsall, J.C. Metcalfe, P.A. Toon, G.B. Warren, Clusters in lipid bilayers and the interpretation of thermal effects in biological membranes, Biochemistry, 13 (1974) 3699–705.

[22] F. Wunderlich, W. Kreutz, P. Mahler, A. Ronai, G. Heppeler, Thermotropic Fluid Ordered “Discontinuous” Phase Separation in Microsomal Lipids of Tetrahymena: An X-Ray Diffraction Study, Biochemistry, 17 (1978) 2005.

[23] M.J. Karnovsky, a M. Kleinfeld, R.L. Hoover, R.D. Klausner, The concept of lipid domains in membranes, The Journal of Cell Biology, 94 (1982) 1–6.

[24] K. Simons, G. van Meer, Lipid Sorting in Epithelial Cells, Biochemistry, 27 (1988) 6197–6202.

[25] K.I. Florine, G.W. Feigenson, Protein redistribution in model membranes: clearing of M13 coat protein from calcium-induced gel-phase regions in phosphatidylserine/phosphatidylcholine multilamellar vesicles, Biochemistry, 26 (1987) 2978–83.

[26] A.R.G. Dibble, M.D. Yeager, G.W. Feigenson, Partitioning of gramicidin A' between coexisting fluid and gel phospholipid phases, Biochimica Et Biophysica Acta, 1153 (1993) 155–62.

[27] D.A. Brown, J.K. Rose, Sorting of GPI-anchored proteins to glycolipid-enriched membrane subdomains during transport to the apical cell surface, Cell, 68 (1992) 533.

[28] J.R. Silvius, D. del Giudice, M. Lafleur, Cholesterol at different bilayer concentrations can promote or antagonize lateral segregation of phospholipids of differing acyl chain length, Biochemistry, 35 (1996) 15198–208.

[29] S.N. Ahmed, D.A. Brown, E. London, On the origin of sphingolipid/cholesterol-rich detergent-insoluble cell membranes: physiological concentrations of cholesterol and sphingolipid induce formation of a detergent-insoluble, liquid-ordered lipid phase in model membranes, Biochemistry, 36 (1997) 10944–53.

[30] K. Simons, E. Ikonen, Functional rafts in cell membranes, Nature, 387 (1997) 569–572.

[31] E.K. Fridriksson, P.A. Shipkova, E.D. Sheets, D. Holowka, B. Baird, F.W. McLafferty, Quantitative analysis of phospholipids in functionally important membrane domains from RBL-2H3 mast cells using tandem high-resolution mass spectrometry, Biochemistry, 38 (1999) 8056–63.

[32] L.J. Pike, X. Han, K.-N. Chung, R.W. Gross, Lipid rafts are enriched in arachidonic acid and plasmenylethanolamine and their composition is independent of caveolin-1 expression: a quantitative electrospray ionization/mass spectrometric analysis, Biochemistry, 41 (2002) 2075–88.

[33] K. Simons, D. Toomre, Lipid rafts and signal transduction, Nature Reviews Molecular Cell Biology, 1 (2000) 31–9.

[34] L.J. Foster, C.L. De Hoog, M. Mann, Unbiased quantitative proteomics of lipid rafts reveals high specificity for signaling factors, Proceedings of the National Academy of Sciences, 100 (2003) 5813–8.

[35] R.G.W. Anderson, K. Jacobson, A role for lipid shells in targeting proteins to caveolae, rafts, and other lipid domains, Science, 296 (2002) 1821–5.

[36] M.Ø. Jensen, O.G. Mouritsen, Lipids do influence protein function-the hydrophobic matching hypothesis revisited, Biochimica Et Biophysica Acta, 1666 (2004) 205–26.

[37] B. Su, L. Gao, F. Meng, L.-W. Guo, J. Rothschild, I.H. Gelman, Adhesion-mediated cytoskeletal remodeling is controlled by the direct scaffolding of Src from FAK complexes to lipid rafts by SSeCKS/AKAP12, Oncogene, (2012) 1–11.

[38] M.E. Fastenberg, H. Shogomori, X. Xu, D. a Brown, E. London, Exclusion of a transmembrane-type peptide from ordered-lipid domains (rafts) detected by fluorescence quenching: extension of quenching analysis to account for the effects of domain size and domain boundaries, Biochemistry, 42 (2003) 12376–90.

[39] T. Baumgart, A.T. Hammond, P. Sengupta, S.T. Hess, D.A. Holowka, B.A. Baird, W.W. Webb, Large-scale fluid/fluid phase separation of proteins and lipids in giant plasma membrane vesicles, Proceedings of the National Academy of Sciences, 104 (2007) 3165–70.

[40] D. Lingwood, J. Ries, P. Schwille, K. Simons, Plasma membranes are poised for activation of raft phase coalescence at physiological temperature, Proceedings of the National Academy of Sciences, 105 (2008) 10005–10.

[41] H.-J. Kaiser, D. Lingwood, I. Levental, J.L. Sampaio, L. Kalvodova, L. Rajendran, K. Simons, Order of lipid phases in model and plasma membranes, Proceedings of the National Academy of Sciences, 106 (2009) 16645–50.

[42] I. Levental, M. Grzybek, K. Simons, Raft domains of variable properties and compositions in plasma membrane vesicles, Proceedings of the National Academy of Sciences, 108 (2011) 11411–6.

[43] L.J. Pike, Rafts defined: a report on the Keystone Symposium on Lipid Rafts and Cell Function, Journal of Lipid Research, 47 (2006) 1597–8.

[44] P. Sharma, R. Varma, R.C. Sarasij, Ira, K. Gousset, G. Krishnamoorthy, M. Rao, S. Mayor, Nanoscale organization of multiple GPI-anchored proteins in living cell membranes, Cell, 116 (2004) 577–89.

[45] P. Sengupta, D. Holowka, B. Baird, Fluorescence resonance energy transfer between lipid probes detects nanoscopic heterogeneity in the plasma membrane of live cells, Biophysical Journal, 92 (2007) 3564–74.

[46] M.J. Swamy, L. Ciani, M. Ge, A.K. Smith, D. Holowka, B. Baird, J.H. Freed, Coexisting domains in the plasma membranes of live cells characterized by spin-label ESR spectroscopy, Biophysical Journal, 90 (2006) 4452–65.

[47] K. Simons, M.J. Gerl, Revitalizing membrane rafts: new tools and insights, Nature Reviews Molecular Cell Biology, 11 (2010) 688–699.

[48] S.T. Hess, T.P.K. Girirajan, M.D. Mason, Ultra-high resolution imaging by fluorescence photoactivation localization microscopy, Biophysical Journal, 91 (2006) 4258–72.

[49] C. Eggeling, C. Ringemann, R. Medda, G. Schwarzmann, K. Sandhoff, S. Polyakova, V.N. Belov, B. Hein, C. von Middendorff, A. Schönle, S.W. Hell, Direct observation of the nanoscale dynamics of membrane lipids in a living cell, Nature, 457 (2009) 1159–62.

[50] L.J. Pike, The challenge of lipid rafts, Journal of Lipid Research, 50 (2009) S323–8.

[51] A.J. García-Sáez, S. Chiantia, P. Schwille, Effect of line tension on the lateral organization of lipid membranes, The Journal of Biological Chemistry, 282 (2007) 33537–44.

[52] S. Mayor, M. Rao, Rafts: scale-dependent, active lipid organization at the cell surface, Traffic, 5 (2004) 231–40.

[53] J. Ehrig, E.P. Petrov, P. Schwille, Near-critical fluctuations and cytoskeleton-assisted phase separation lead to subdiffusion in cell membranes, Biophysical Journal, 100 (2011) 80–9.

[54] B.B. Machta, S. Papanikolaou, J.P. Sethna, S.L. Veatch, Minimal model of plasma membrane heterogeneity requires coupling cortical actin to criticality, Biophysical Journal, 100 (2011) 1668–77.

[55] K. Simons, W.L.C. Vaz, Model systems, lipid rafts, and cell membranes, Annual Review of Biophysics and Biomolecular Structure, 33 (2004) 269–95.

[56] Y.-W. Chiang, Y. Shimoyama, G.W. Feigenson, J.H. Freed, Dynamic molecular structure of DPPC-DLPC-cholesterol ternary lipid system by spin-label electron spin resonance, Biophysical Journal, 87 (2004) 2483–96.

[57] A.K. Smith, J.H. Freed, Dynamics and ordering of lipid spin-labels along the coexistence curve of two membrane phases: An ESR study, Chemistry and Physics of Lipids, 165 (2012) 348–361.

[58] K.P. Shaw, N.J. Brooks, J.A. Clarke, O. Ces, J.M. Seddon, R. V. Law, Pressure–temperature phase behaviour of natural sphingomyelin extracts, Soft Matter, 8 (2012) 1070.

[59] A. Tardieu, V. Luzzati, F.C. Reman, Structure and polymorphism of the hydrocarbon chains of lipids: a study of lecithin-water phases, Journal of Molecular Biology, 75 (1973) 711–33.

[60] O. Lenz, F. Schmid, Structure of Symmetric and Asymmetric "Ripple" Phases in Lipid Bilayers, Physical Review Letters, 98 (2007) 058104.

[61] P.F. Fahey, W.W. Webb, Lateral diffusion in phospholipid bilayer membranes and multilamellar liquid crystals, Biochemistry, 17 (1978) 3046–53.

[62] G.G. Shipley, L.S. Avecilla, D.M. Small, Phase behavior and structure of aqueous dispersions of sphingomyelin, Journal of Lipid Research, 15 (1974) 124–31.

[63] J.H. Ipsen, G. Karlstrom, O.G. Mouritsen, H. Wennerstrom, M.J. Zuckermann, Phase equilibria in the phosphatidylcholine-cholesterol system, Biochimica Et Biophysica Acta, 905 (1987) 162–172.

[64] P.F. Almeida, W.L. Vaz, T.E. Thompson, Lateral diffusion in the liquid phases of dimyristoylphosphatidylcholine/ cholesterol lipid bilayers: a free volume analysis, Biochemistry, 31 (1992) 6739–47.

[65] M.R. Vist, J.H. Davis, Phase equilibria of cholesterol/ dipalmitoylphosphatidylcholine mixtures: 2H nuclear magnetic resonance and differential scanning calorimetry, Biochemistry, 29 (1990) 451–64.

[66] G.W. Feigenson, J.T. Buboltz, Ternary Phase Diagram of Dipalmitoyl-PC/Dilauroyl-PC/Cholesterol: Nanoscopic Domain Formation Driven by Cholesterol, Biophysical Journal, 80 (2001) 2775–2788.

[67] J. Zhao, J. Wu, F.A. Heberle, T.T. Mills, P. Klawitter, G. Huang, G. Costanza, G.W. Feigenson, Phase studies of model biomembranes: complex behavior of DSPC/DOPC/cholesterol, Biochimica Et Biophysica Acta, 1768 (2007) 2764–76.

[68] J. Huang, G.W. Feigenson, A Microscopic Interaction Model of Maximum Solubility of Cholesterol in Lipid Bilayers, Biophysical Journal, 76 (1999) 2142–2157.

[69] F.A. Heberle, R.S. Petruzielo, J. Pan, P. Drazba, N. Kucerka, R.F. Standaert, G.W. Feigenson, J. Katsaras, Bilayer thickness mismatch controls raft size in model membranes, Submitted, (2012).

[70] J. Pan, T. Mills, S. Tristram-Nagle, J. Nagle, Cholesterol Perturbs Lipid Bilayers Nonuniversally, Physical Review Letters, 100 (2008) 198103.

[71] L.R. Arriaga, I. López-Montero, F. Monroy, G. Orts-Gil, B. Farago, T. Hellweg, Stiffening effect of cholesterol on disordered lipid phases: a combined neutron spin echo + dynamic light scattering analysis of the bending elasticity of large unilamellar vesicles, Biophysical Journal, 96 (2009) 3629–37.

[72] I. V. Polozov, K. Gawrisch, Characterization of the liquid-ordered state by proton MAS NMR, Biophysical Journal, 90 (2006) 2051–61.

[73] K.K. Halling, B. Ramstedt, J.H. Nyström, J.P. Slotte, T.K.M. Nyholm, Cholesterol interactions with fluid-phase phospholipids: effect on the lateral organization of the bilayer, Biophysical Journal, 95 (2008) 3861–71.

[74] R.F.M. de Almeida, A. Fedorov, M. Prieto, Sphingomyelin/ phosphatidylcholine/ cholesterol phase diagram: boundaries and composition of lipid rafts, Biophysical Journal, 85 (2003) 2406–16.

[75] I. V. Ionova, V.A. Livshits, D. Marsh, Phase Diagram of Ternary Cholesterol/ Palmitoylsphingomyelin/ Palmitoyloleoyl-Phosphatidylcholine Mixtures: Spin-Label EPR Study of Lipid-Raft Formation, Biophysical Journal, 102 (2012) 1856–1865.

[76] J. Korlach, P. Schwille, W.W. Webb, G.W. Feigenson, Characterization of lipid bilayer phases by confocal microscopy, Proceedings of the National Academy of Sciences, 96 (1999) 8461–8466.

[77] C. Dietrich, L.A. Bagatolli, Z.N. Volovyk, N.L. Thompson, M. Levi, K. Jacobson, E. Gratton, Lipid rafts reconstituted in model membranes, Biophysical Journal, 80 (2001) 1417–28.

[78] A. V. Samsonov, I. Mihalyov, F.S. Cohen, Characterization of cholesterol-sphingomyelin domains and their dynamics in bilayer membranes, Biophysical Journal, 81 (2001) 1486–500.

[79] S.L. Veatch, S.L. Keller, Separation of Liquid Phases in Giant Vesicles of Ternary Mixtures of Phospholipids and Cholesterol, Biophysical Journal, 85 (2003) 3074–3083.

[80] S.L. Veatch, S.L. Keller, Miscibility Phase Diagrams of Giant Vesicles Containing Sphingomyelin, Physical Review Letters, 94 (2005) 148101.

[81] S.L. Veatch, K. Gawrisch, S.L. Keller, Closed-loop miscibility gap and quantitative tie-lines in ternary membranes containing diphytanoyl PC, Biophysical Journal, 90 (2006) 4428–36.

[82] F.A. Heberle, J. Wu, S.L. Goh, R.S. Petruzielo, G.W. Feigenson, Comparison of three ternary lipid bilayer mixtures: FRET and ESR reveal nanodomains, Biophysical Journal, 99 (2010) 3309–3318.

[83] E.R. Farkas, W.W. Webb, Precise and millidegree stable temperature control for fluorescence imaging: application to phase transitions in lipid membranes, The Review of Scientific Instruments, 81 (2010) 093704.

[84] A. Pokorny, L.E. Yandek, A.I. Elegbede, A. Hinderliter, P.F.F. Almeida, Temperature and composition dependence of the interaction of delta-lysin with ternary mixtures of sphingomyelin/cholesterol/POPC, Biophysical Journal, 91 (2006) 2184–97.

[85] E.L. Elson, E. Fried, J.E. Dolbow, G.M. Genin, Phase separation in biological membranes: integration of theory and experiment, Annual Review of Biophysics, 39 (2010) 207.

[86] P. Pathak, E. London, Measurement of Lipid Nanodomain (Raft) Formation and Size in Sphingomyelin/POPC/Cholesterol Vesicles Shows TX-100 and Transmembrane Helices Increase Domain Size by Coalescing Preexisting Nanodomains But Do Not Induce Domain Formation, Biophysical Journal, 101 (2011) 2417–2425.

[87] M.L. Frazier, J.R. Wright, A. Pokorny, P.F.F. Almeida, Investigation of domain formation in sphingomyelin/cholesterol/POPC mixtures by fluorescence resonance energy transfer and Monte Carlo simulations, Biophysical Journal, 92 (2007) 2422–33.

[88] J. Zhao, J. Wu, H. Shao, F. Kong, N. Jain, G. Hunt, G.W. Feigenson, Phase studies of model biomembranes: macroscopic coexistence of Lalpha+Lbeta, with light-induced coexistence of Lalpha+Lo Phases, Biochimica Et Biophysica Acta, 1768 (2007) 2777–86.

[89] J. Pan, F.A. Heberle, R.S. Petruzielo, J. Katsaras, The Usage of Small-Angle Neutron Scattering in Exploiting Nanoscopic Lipid Domains, Chemistry and Physics of Lipids, (2013).

Chapter 2
Phase Behavior and Domain Size in Sphingomyelin-Containing Lipid Bilayers

This chapter has been accepted for publication in *BBA Biomembranes*: Robin S. Petruzielo, Frederick A. Heberle, Paul Drazba, John Katsaras, and Gerald W. Feigenson. Phase Behavior and Domain Size in Sphingomyelin-Containing Lipid Bilayers. *Accepted* (2013). The referenced Appendices appear as the Supplementary Material.

2.1 ABSTRACT

Membrane raft size measurements are crucial to understanding the stability and functionality of rafts in cells. The challenge of accurately measuring raft size is evidenced by the disparate reports of domain sizes, which range from nanometers to microns for the ternary model membrane system sphingomyelin (SM)/1-palmitoyl-2-oleoyl-*sn*-glycero-3-phosphocholine (POPC)/cholesterol (Chol). Using Förster resonance energy transfer (FRET) and differential scanning calorimetry (DSC), we established phase diagrams for porcine brain SM (bSM)/dioleoyl-*sn*-glycero-3-phosphocholine (DOPC)/Chol and bSM/POPC/Chol at 15 and 25°C. By combining two techniques with different spatial sensitivities, namely FRET and small-angle neutron scattering (SANS), we have significantly narrowed the uncertainty in domain size estimates for bSM/POPC/Chol mixtures. Compositional trends in FRET data revealed coexisting domains at 15 and 25°C for both mixtures, while SANS measurements detected no domain formation for bSM/POPC/Chol. Together these results indicate that liquid domains in bSM/POPC/Chol are between 2 and 7 nm in radius at 25°C: that is, domains must be on the order of the 2–6 nm Förster distance of the FRET probes, but smaller than the ~7 nm minimum cluster size detectable with SANS. However, for palmitoyl SM (PSM)/POPC/Chol at a similar composition, SANS detected coexisting liquid domains. This increase in domain size upon replacing the natural SM component (which consists of a mixture of chain lengths)

with synthetic PSM, suggests a role for SM chain length in modulating raft size *in vivo*.

2.2 INTRODUCTION

The membrane raft model posits that lipids in cell membranes self-organize into compositionally distinct domains, differentiated primarily by hydrocarbon chain order [1,2]. Rafts are thought to organize membrane-associated proteins through selective partitioning, thereby influencing diverse processes including protein transport and signaling. Raft-based explanations for cellular phenomena are often controversial, as rafts cannot be observed directly in resting cells using conventional fluorescence microscopy. Significant effort has gone toward developing techniques capable of detecting nanometer-scale rafts. As these techniques improve, the emerging consensus is that rafts are small, transient clusters of lipids and proteins that can coalesce upon external stimulus to spatially reorganize membrane components and produce functional consequences for the cell [3–6]. To further understand mechanisms responsible for raft stability and functionality in cells at the level of lipid-lipid and lipid-protein interactions, raft sizes must be measured.

Though biological membranes are complex mixtures, substantial progress has been made by studying chemically simplified models for the mammalian outer leaflet, where rafts are implicated in processes including virus entry and exit, and transmembrane signaling. Mixtures comprising three lipid components—a high melting (high-Tm) lipid (di-saturated phosphatidylcholine or SM), a low-Tm lipid (*i.e.*, containing at least one chain unsaturation), and Chol—exhibit key properties associated with rafts [7]. These minimal systems mimic the composition of specific biological membranes and reproduce a variety of complex phenomena, including the coexistence of liquid-ordered (Lo) and liquid-disordered (Ld) domains, yet their compositional simplicity makes them amenable to studies of composition- and temperature-dependent behavior.

Recent work has revealed an important role for the low-Tm lipid (*e.g.*, DOPC or POPC) in the mesoscale control of membrane domain size [8–10]. DOPC is not typically found in cell membranes but has enjoyed popularity in model membrane experiments due to its propensity to induce micron-sized fluid domains in ternary mixtures [11]. In contrast, POPC is an abundant, low-Tm lipid in the outer leaflet of the plasma membrane[12] and has been studied in ternary mixtures using techniques sensitive to submicron length scales [8,13–23]. Ternary mixtures containing POPC together with a high-Tm lipid and Chol seem to exclusively exhibit *nanoscale* Ld+Lo heterogeneity [24], as opposed to the micron-sized domains observed in DOPC-containing mixtures.

Di-saturated phosphatidylcholine lipids (*e.g.*, DPPC and DSPC) are commonly chosen as high-Tm lipids for bilayer phase studies, despite their relative scarcity in mammalian plasma membrane. While much is now known about the phase behavior of these lipids in raft mixtures, the influence of SM, an abundant outer leaflet lipid, on raft properties remains poorly understood. Unlike glycerol-based lipids, SM is capable of forming both inter- and intra-molecular hydrogen bonds because it possesses both hydrogen bond donors and acceptors in its sphingosine backbone. The hydrogen-bonding capability of SM might contribute to the intrinsically high order of this class of lipids. This, or other charge-pairing and hydrophobic effects, may play an important role in raft formation through SM-Chol interactions [25].

Macroscopic coexisting Ld+Lo domains have been observed in the mixture SM/DOPC/Chol using fluorescence microscopy of giant unilamellar vesicles (GUVs) [26–31]. A more biologically relevant model system would replace DOPC with POPC. Zhao et al. found that in mixtures with POPC and Chol, a variety of SM species suffer from domain artifacts due to photo-induced lipid modification, including peroxidation or cross-linking, which are directly related to the presence of fluorophores [32]. By using dilute probe concentrations, limiting the illumination intensity and duration, and carefully observing the time dependence of domain formation, it was concluded that no *macroscopic* Ld+Lo phase coexistence occurs in SM/POPC/Chol [32]. This result implies that if rafts exist in these biologically important systems, they must be smaller than the ~200 nm resolution limit of light microscopy.

Using techniques with sensitivity to nanometer length scales, researchers have published phase diagrams for ternary mixtures of SM/POPC/Chol that include large regions of Ld+Lo phase coexistence [14,16,19,23,29], albeit with large discrepancies in the locations of phase boundaries and the topology of the phase diagrams. These discrepancies may be related, in part, to the widespread use of fluorescence techniques for establishing phase boundaries, in combination with excessive fluorophore concentration [32–35]. For these biologically important mixtures, we turn to alternative techniques including FRET with very low probe concentrations, and probe-free approaches including SANS and DSC. We report on the phase behavior of bSM/DOPC/Chol and bSM/POPC/Chol from 15–35°C, including detection of Ld+Lo phase separation in bSM/POPC/Chol with FRET, but not with SANS. Taking into account the different spatial sensitivities of these techniques, we conclude that nanodomains are present in bSM/POPC/Chol, but not larger than ~ 7 nm radius.

2.3 MATERIALS and METHODS

2.3.1 Materials

Sphingolipids and glycerophospholipids were purchased from Avanti Polar Lipids (Alabaster, AL) as lyophilized powder (PSM, PSM-d31, POPC-d31) or stock solutions in chloroform (bSM, DOPC, POPC). Lipid stock solutions were prepared in

HPLC grade chloroform with concentration determined to < 1% by inorganic phosphate assay. SM stocks included 0.5% methanol by volume to prevent precipitation during humid weather. Chol was obtained from Nu Chek Prep (Elysian, MN) and prepared in chloroform with standard gravimetric methods to 0.2%. Ultrapure H_2O from purification systems (EMD Millipore, Billerica, MA or Barnstead, Dubuque, IA) was used for all aqueous sample preparations. D_2O of 99.8% purity was purchased from Alfa Aesar (Ward Hill, MA).

The fluorescent lipid analogs dehydrogerosterol (DHE, Sigma-Aldrich, St. Louis, MO), 16:0,BoDIPY-PC (BoDIPY-PC, Invitrogen, Carlsbad, CA), and lissamine rhodamine 18:1,18:1-PE (LR-DOPE, Avanti) were prepared in chloroform. Probe concentrations were determined in methanol by absorption spectroscopy using an HP 8452A spectrophotometer (Hewlett-Packard, Palo Alto, CA). Probe extinction coefficients were obtained from lot certificates of analysis: 91800 $M^{-1}cm^{-1}$ at 504 nm for BoDIPY-PC, 75000 $M^{-1}cm^{-1}$ at 560 nm for LR-DOPE, and 12900 $M^{-1}cm^{-1}$ at 324 nm for DHE. Purity to > 99% was confirmed using thin-layer chromatography (TLC) on washed, activated Adsorbosil TLC plates (Alltech, Deerfield, IL) developed with: chloroform/methanol/water (65/24/4) for all sphingolipids and phospholipids including BoDIPY-PC; chloroform/methanol (9/2) for LR-DOPE; and petroleum ether/diethyl ether/chloroform (7/3/3) for DHE and Chol.

For all sample preparation described below, chloroform mixtures of lipids and probes were prepared in glass culture tubes using a glass syringe (Hamilton USA, Reno, NC). For FRET and DSC measurements, paucilamellar vesicles (PLVs) were prepared from these mixtures using rapid solvent exchange (RSE) [36]. For SANS measurements, PLVs were prepared by dry film hydration. For FRET samples, the aqueous buffer contained 200 mM KCl, 5 mM PIPES, and 1 mM EDTA at pH 7.0. DSC and SANS samples were prepared in water: H_2O for DSC, and an appropriate

D_2O/H_2O mixture for SANS. TLC analysis of randomly selected samples exhibited no evidence of lipid breakdown after measurement.

2.3.2 Forster Resonance Energy Transfer (FRET)

Phase diagrams for bSM/DOPC/Chol and bSM/POPC/Chol were determined with FRET using the experimental methodology of preparing samples at regular increments over the composition space, as described previously [8,37]. Samples were prepared at 3.6 mol% compositional increments, up to 66 mol% Chol. Fluorescent probes were combined in a single chloroform stock to obtain a desired probe ratio, and all samples received a fixed volume of this stock. Samples contained three probes comprising two donor/acceptor FRET pairs: DHE/BoDIPY-PC and BoDIPY-PC/LR-DOPE. Probe concentrations (expressed as probe/lipid ratio) were 1/100 for DHE, and 1/1500 for BoDIPY-PC and LR-DOPE. In addition to FRET samples containing all dyes, three sets of controls containing a single dye were prepared at 10 mol% compositional increments, with concentrations 1/100 (DHE) and 1/1000 (BoDIPY-PC and LR-DOPE). Samples containing only lipid (*i.e.*, no probe) were prepared at representative Lo, Ld, and gel phase compositions. Single-dye and lipid-only controls were used to correct raw FRET signals as described previously [38].

FRET measurements were performed with a Hitachi F-7000 spectrofluorimeter (Hitachi High Technologies America, Schaumburg, IL) equipped with a temperature-controlled cuvette holder (Quantum Northwest, Inc.). Measurements were performed at 15, 25, 35, and 45°C for bSM/DOPC/Chol, and at 5, 15, 25, and 35°C for bSM/POPC/Chol. (Procedures for maintaining sample temperatures within 1°C throughout the measurement process are described in Appendix A.2.) Samples were diluted into buffer gently stirring in the cuvette for a final concentration of 32 μM (total lipid). Intensity measurements were made using 5 and 10 nm excitation and emission slits, respectively, and a 2.0 s integration time, at six pairs of excitation and emission wavelengths (ex/em in nm). While only two channels are sensitized acceptor emission (SAE) FRET signals [39], the remaining channels are necessary to correct for donor and acceptor bleedthrough, and scattering of the excitation light [38]. The six channels include DHE fluorescence (327/393), BoDIPY-PC SAE (327/520), BoDIPY-PC fluorescence (500/520), LR-DOPE SAE (500/587), LR-DOPE fluorescence (565/587), and vesicle scattering (440/428). A full measurement for each sample was acquired in ~ 1.5 min.

2.3.3 Differential Scanning Calorimetry (DSC)

PLVs prepared by RSE were centrifuged for one hour at 9000 rpm (11726g) at 10°C in a Sorvall RC 5B Plus using an SA-600 rotor. The supernatant was removed, and the remaining PLV samples had concentrations of 8 mg/mL (for 0 mol% Chol samples) or 15 mg/mL (for 10 mol% Chol compositions). Samples were stored at 4°C until measurement. Thermograms were acquired on a Nano Differential Scanning Calorimeter with active temperature control for both heating and cooling scans (TA Instruments, Waters LLC, New Castle, DE). Alternate fast heating and cooling scans at a scan rate of 2°C/min were performed twice (a total of 4 scans) to equilibrate samples before performing slow heating and cooling scans at a scan rate of 0.2 °C/min. Only the slow scans were used for data analysis.

Data analysis was performed using Mathematica v7. A baseline was subtracted, and the temperatures of phase coexistence onset and completion were determined using the model-free tangent construction method [40,41]. Additional analysis details are found in Appendix B.

2.3.4 Small-Angle Neutron Scattering (SANS)

Chloroform mixtures of lipids were evaporated under a gentle N_2 stream followed by drying *in vacuo* for > 12 h. PLVs were prepared by dry film hydration. Briefly, the dry films was hydrated with an appropriate D_2O/H_2O mixture preheated to

50°C, then mechanically agitated to disperse the lipid. In some cases, brief (< 5 s) sonication was necessary to remove all lipid from the tube walls. The PLV suspension was then incubated for 1 h at 50°C, followed by 5 freeze/thaw cycles between -80°C and 50°C. PLVs were stored at -80°C and extruded < 24 h prior to measurement. Unilamellar vesicles (ULVs) were prepared by passing the sample 41 times through a single 50 nm diameter pore size filter, using a hand-held mini extruder (Avanti Polar Lipids, Alabaster, AL). Final sample concentrations were 10–15 mg/mL, a concentration that ensures sufficient water between vesicles to eliminate the interparticle structure factor, thereby simplifying data analysis [42].

SANS experiments were performed at Oak Ridge National Laboratory (ORNL) at both the High Flux Isotope Reactor (HFIR) on the CG-3 Bio-SANS instrument and the Spallation Neutron Source (SNS) on the BL-6 extended Q-range small-angle neutron scattering (EQ-SANS) instrument. ULV suspensions were loaded into 1 mm path length quartz banjo cells (Hellma USA, Plainview, NY) and mounted in a temperature controlled cell holder with 1°C accuracy. All samples were incubated at the desired temperature for > 30 min prior to measurement. Bio-SANS data were acquired using neutrons of wavelength (λ) 6 Å with a $\Delta\lambda/\lambda$ of 15%. With sample-to-detector distances (SDD) 1.7 and 14.5 m, the resulting scattering vector (q) range was $0.005 < q < 0.3$ Å^{-1}. EQ-SANS data were acquired with a 6–10 Å wavelength band and SDD 4.0 m, resulting in a q range $0.005 < q < 0.2$ Å^{-1}. A two-dimensional (1 m × 1 m) ^{3}He position-sensitive detector (ORDELA, Inc., Oak Ridge, TN) with 192 × 192 pixels (Bio-SANS) or 256 × 192 pixels (EQ-SANS) was used to collect scattered neutrons.

Software provided by ORNL was used to reduce the 2D data, correcting for detector pixel sensitivity, dark current, and sample transmission. Background scattering due to water was subtracted. Radial averaging of the corrected 2D data yielded the 1D scattering intensity I vs. q, where q is calculated as $q = 4\pi \sin(\theta)/\lambda$ for neutron wavelength λ and scattering angle 2θ relative to the incident beam. Additional analysis details are found in Appendix C.

2.4 RESULTS

2.4.1 Steady-State Probe-Partitioning FRET (SP-FRET)

We used FRET between fluorescent lipids to examine the composition- and temperature-dependent phase behavior of bSM/DOPC/Chol and bSM/POPC/Chol. FRET is sensitive to changes in the distribution of donor/acceptor distances that accompany phase separation [43]. Briefly, when a single phase is present, probes are distributed in the plane of the bilayer such that FRET efficiency varies only gradually with composition. Relative to this baseline behavior, FRET efficiency changes dramatically upon crossing into regions of phase coexistence, depending on the relative partitioning behavior of the probes. FRET efficiency is enhanced in composition regions where both probes prefer the same phase, and reduced where probes prefer different phases. Compositional regions exhibiting these two classes of behavior are termed “regions of enhanced or reduced efficiency” (REE or RRE, respectively). To obtain reliable measurements at low probe concentrations where absolute FRET efficiencies are low, we measured SAE while exciting the donor [39]. We used two Ld-preferring probes, BoDIPY-PC and LR-DOPE, which exhibit REE behavior in coexistence regions containing Ld phase. In addition, samples contained the fluorescent cholesterol analog DHE, which partitions modestly into ordered phases [44], forming an RRE pair with BoDIPY-PC.

2.4.1.1 bSM/DOPC/Chol

The upper panels of Fig. 2.1 show FRET from BoDIPY-PC to LR-DOPE at 15, 25, and 35°C. The dominant feature in the 15 and 25°C data is a pair of peaks of enhanced FRET on the right side of the phase diagram (*i.e.*, low DOPC concentration).

Close to the binary bSM/Chol axis, the REE corresponds to colocalization of probes in the Lo phase, likely in coexistence with Lβ gel [45]. In contrast, on the DOPC/Chol binary axis, modest FRET variation indicates complete miscibility and continuous changes with increasing Chol. The second FRET peak, located at ~ 60 mol% bSM and 30 mol% Chol, marks the right-hand boundary of the Ld+Lo region. In the vicinity of this peak, the disorder-preferring probes are concentrated in the minority Ld phase due to strong partitioning, and the reduced average donor-acceptor separation distance results in enhanced FRET efficiency. The upper boundary of the Ld+Lo region at ~ 40 mol% Chol is clearly observed as an abrupt change in FRET. Enhanced FRET in single-phase compositions just above the Ld+Lo region persists at 45°C (Fig. A.1), suggesting a critical point at bSM/DOPC/Chol ~ 0.30/0.33/0.37 [8].

The lower panels of Fig. 2.1 show FRET from DHE to BoDIPY-PC at 15, 25, and 35°C. The most prominent feature in the 15 and 25°C data is a valley of reduced FRET efficiency in the Ld+Lo coexistence region due to segregation of DHE and BoDIPY-PC between the Lo and Ld phase, respectively. The deepest part of this valley seems to correspond to the tieline with the largest compositional separation between the Ld and Lo phases (*i.e.*, the most compositionally distinct coexisting phases). Following this logic, the Ld+Lo FRET peak (Fig. 2.1, upper panels) corresponds to the same tieline. Connecting the FRET peak and valley therefore gives an estimate of the direction of Ld+Lo tielines. FRET along this tieline is shown in Fig. 2.2. The positive tieline slope (33°) indicates greater Chol concentration in the Lo phase.

Focusing on the temperature dependence of the features described above, the RRE and REE decrease in magnitude, and the range of compositions over which these features persist contracts slightly upon increasing the temperature from 15 to 25°C. FRET is nearly homogeneous at 35°C, as bSM mixes to a greater extent with DOPC.

The absence of enhanced and reduced FRET regions at 35°C indicates lipid miscibility, despite the persistence of modest FRET trends. These trends are even less pronounced at 45°C (Fig. A.1), above the bSM melting temperature.

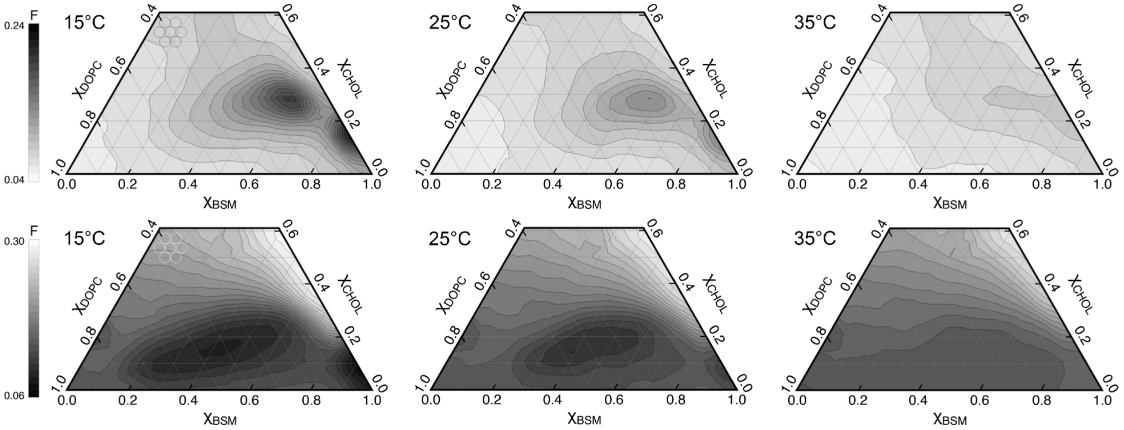

Figure 2.1 FRET reveals phase coexistence regions in bSM/DOPC/Chol. Contour plots constructed from FRET measurements at 360 compositions for three temperatures, using the probe pairs BoDIPY-PC/LR-DOPE (upper panel) and DHE/BoDIPY-PC (lower panel). Regions of enhanced (upper panel) or reduced (lower panel) FRET efficiency result from non-uniform probe partitioning in phase coexistence regions. Data were smoothed with nearest-neighbor averaging. Open circles on 15°C plots show the compositional resolution of the data.

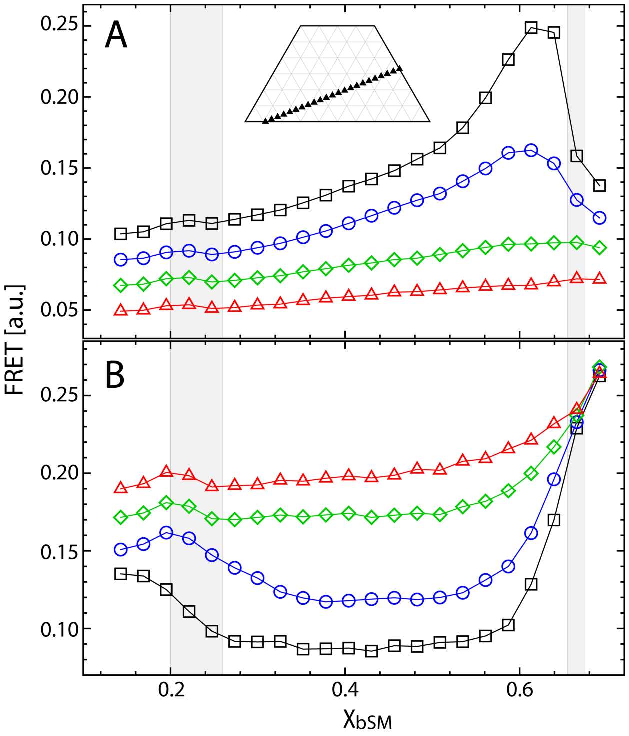

Figure 2.2 Tieline slices through the FRET surfaces of bSM/DOPC/Chol indicate the presence of phase boundaries. Slices along the tieline trajectory (inset) reveal enhanced FRET efficiency for BoDIPY-PC/LR-DOPE (*A*) and reduced FRET efficiency for DHE/BoDIPY-PC (*B*) at 15°C (squares), 25°C (circles), 35°C (diamonds), and 45°C (triangles). Phase boundaries and uncertainty at 15-25°C are indicated by gray vertical lines. A small change in FRET from 35-45°C indicates a miscibility transition between 35-45°C. Trajectories are offset for clarity.

2.4.1.2 bSM/POPC/Chol

Unlike bSM/DOPC/Chol, bSM/POPC/Chol does not exhibit macroscopic Ld+Lo phase coexistence in GUVs examined by fluorescence microscopy [32]. However, the sensitivity of FRET to nanometer distance scales could reveal heterogeneity in bSM/POPC/Chol, similar to the FRET peak and valley described above for bSM/DOPC/Chol. The upper panels of Fig. 2.3 show FRET from BoDIPY-PC to LR-DOPE at 15, 25, and 35°C. In contrast to bSM/DOPC/Chol, only the FRET peak located on the binary bSM/Chol axis is observed. However, a ridge of enhanced FRET originates at this peak and extends across the ternary composition space at ~ 20 mol% Chol, such that slices through the data (Fig. 2.4*A*) exhibit characteristic REE behavior, albeit reduced in magnitude, relative to corresponding slices in bSM/DOPC/Chol (Fig. 2.2*A*). This behavior is consistent with coexisting Ld+Lo domains with average radii close to the ~ 6 nm R_0 of this probe pair. With increasing POPC fraction, the height of this ridge decreases; along the POPC/Chol binary axis, only a gradual increase in FRET occurs with increasing Chol, indicating nearly uniform mixing.

The lower panels of Fig. 2.3 show FRET from DHE to BoDIPY-PC. In the 15 and 25°C data, a region of reduced FRET efficiency consistent with Ld+Lo coexistence is seen in trajectory slices (Fig. 2.4*B*). Given that the R_0 of the DHE/BoDIPY-PC pair is ~ 2 nm, it is reasonable to conclude that coexisting Ld+Lo domains have average radii between 2–6 nm at 15 and 25°C. For both probe pairs, nearly uniform mixing is observed at 35°C.

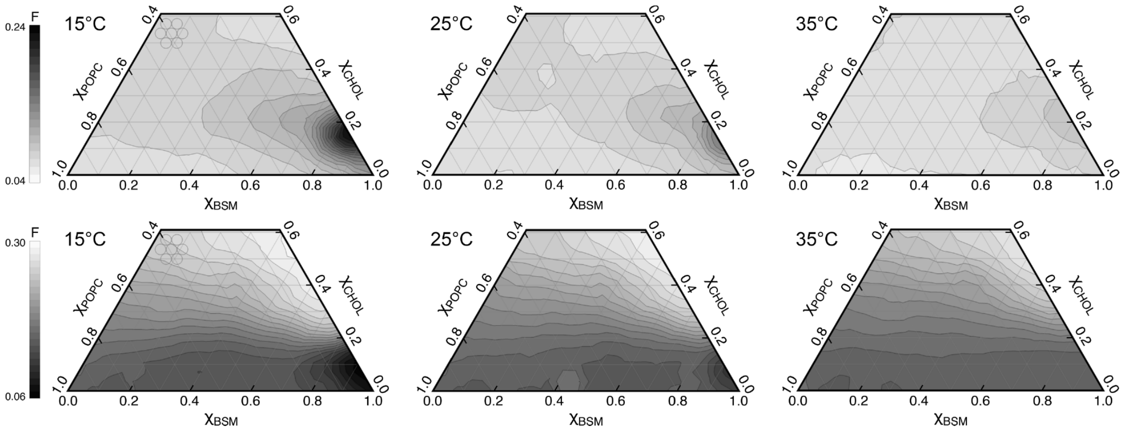

Figure 2.3 FRET reveals phase coexistence regions in bSM/POPC/Chol. Contour plots constructed from FRET measurements at 360 compositions for three temperatures, using the probe pairs BoDIPY-PC/LR-DOPE (upper panel) and DHE/BoDIPY-PC (lower panel). Regions of enhanced (upper panel) or reduced (lower panel) FRET efficiency result from non-uniform probe partitioning in phase coexistence regions. Data were smoothed with nearest-neighbor averaging. Open circles on 15°C plots show the compositional resolution of the data.

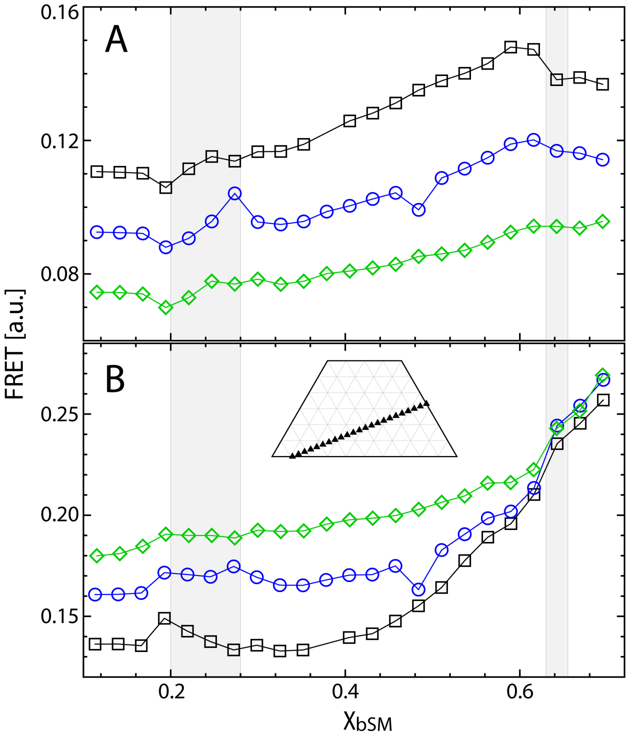

Figure 2.4 Tieline slices through the FRET surfaces of bSM/POPC/Chol weakly indicate the presence of phase boundaries. Slices along the tieline trajectory (inset) reveal enhanced FRET efficiency for BoDIPY-PC/LR-DOPE (*A*) and reduced FRET efficiency for DHE/BoDIPY-PC (*B*) at 15°C (squares), 25°C (circles), and 35°C (diamonds). Phase boundaries and uncertainty at 15-25°C are indicated by gray vertical lines. Trajectories are offset for clarity.

2.4.2 DSC

We used DSC to investigate bSM/DOPC and bSM/POPC phase behavior at low Chol concentration, where gel phases are present. Figure 2.5 shows a complete binary phase diagram for bSM/POPC, (Fig. 2.5, squares) and partial phase diagrams for both bSM/POPC+10 mol% Chol (Fig. 2.5, circles) and bSM/DOPC (Fig. 2.5, triangles), determined from baseline-corrected thermograms shown in Figs. B.1-B.3. At 15°C, the Ld+Lβ region ranges from $0.10<\chi_{bSM}<0.80$ for bSM/DOPC, $0.11<\chi_{bSM}<0.80$ for bSM/POPC, and $0.10<\chi_{bSM}<0.80$ for bSM/POPC+10 mol% Chol. At 25°C, these ranges shift to $0.20<\chi_{bSM}<0.97$ for bSM/DOPC, $0.28<\chi_{bSM}<0.97$ for bSM/POPC, and $0.20<\chi_{bSM}<0.90$ for bSM/POPC+ 10 mol% Chol. We estimate that all boundaries are subject to an uncertainty in χ_{bSM} of ~ ±0.03.

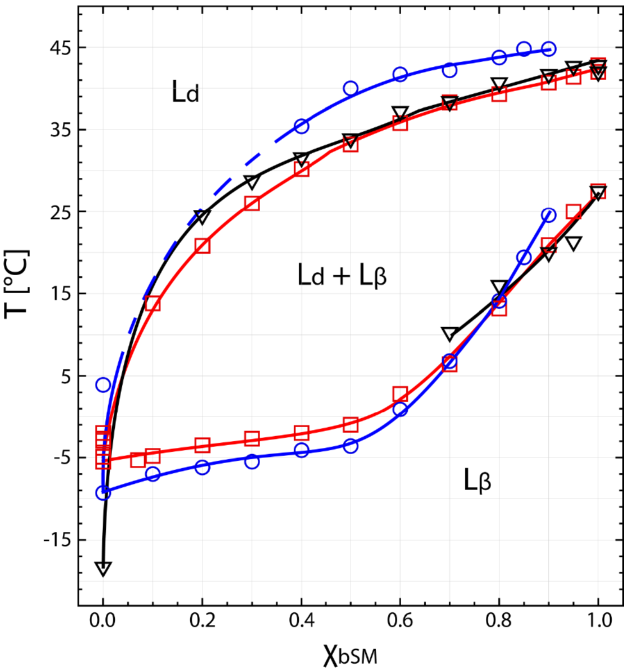

Figure 2.5 DSC provides phase boundaries for binary bSM/PC/Chol mixutres. Onset and completion temperatures for bSM/DOPC (triangles), bSM/POPC (squares), and bSM/POPC with 10 mol% Chol (circles). Phase boundaries at 15 and 25°C were used in constructing the phase diagrams in Fig. 2.6. The transition temperature for DOPC is taken to be the literature value -18.3 +/- 3.5°C [46]. Dashed lines indicate interpolated phase boundaries. Thermograms used to construct these phase diagrams appear in Figs. B.1-B.3.

2.4.3 Phase Diagrams

Figure 2.6 shows phase diagrams for bSM/DOPC/Chol (top) and bSM/POPC/Chol (bottom), constructed from FRET and DSC data. DSC data (Fig. 2.5) were used to determine the Ld+Lβ boundaries on the binary bSM/DOPC and bSM/POPC axes, and FRET data (Figs. 2.1 and 2.3) were used to determine the boundary of the Ld+Lo coexistence region. Slices through the surface data, like those shown in Figs. 2.2 and 2.4, were taken, and additional DHE/BoDIPY-PC FRET trajectories at ~ 0.5 mol% compositional resolution were employed (data not shown). Phase boundaries were estimated where the FRET signal exhibits a change in slope as a function of composition along the slice [38], with typical uncertainties shown in Figs. 2.2 and 2.4 (gray vertical shading). Difference FRET surfaces (Figs. A.2-A.3) obtained by subtracting the highest temperature data from lower temperature data were also used to better detect temperature-dependent changes, as described in Appendix A.2. Similarities between the bSM/DOPC/Chol and bSM/POPC/Chol phase diagrams indicate that changing the low-Tm lipid from DOPC to POPC does not significantly alter the phase diagram.

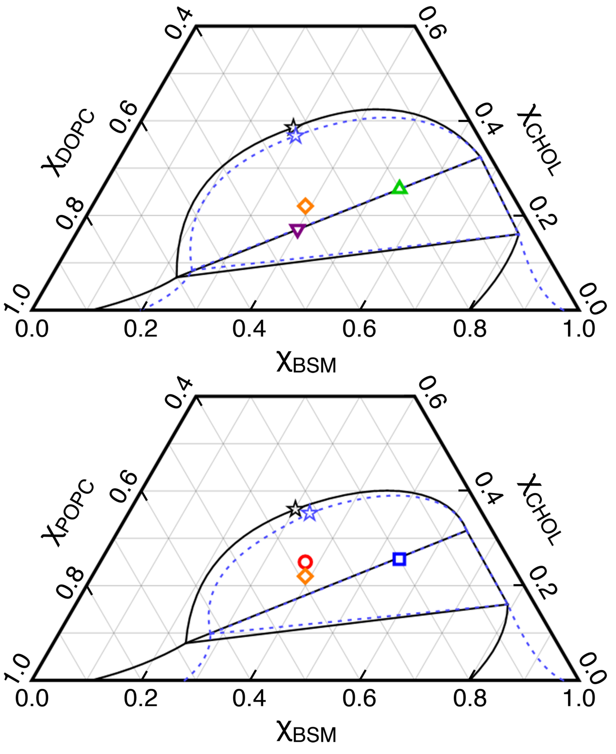

Figure 2.6 Phase diagrams for bSM/DOPC/Chol and bSM/POPC/Chol determined by combination of FRET and DSC. Phase diagrams for bSM/DOPC/Chol (*top*) and bSM/POPC/Chol (*bottom*) at 15°C (solid) and 25°C (dotted). Phase boundaries and critical points for the Ld+Lo coexistence region were determined by taking slices (Figs. 2.2 and 2.4) though the high-resolution FRET surface data (Figs. 2.1 and 2.3), as discussed in the text. Phase boundaries for Ld+Lβ coexistence were determined from the DSC phase diagrams (Fig. 2.5). Points indicate compositions examined with SANS (Figs. 2.7-2.8), including: dPSM/DOPC/Chol = 0.54/0.20/0.26 (upward-pointing triangle), dPSM/DOPC/Chol = 0.40/0.43/0.17 (downward-pointing triangle), dPSM/DOPC/Chol= 0.39/0.39/0.22 (diamond), bSM/dPOPC/Chol = 0.54/0.20/0.26 (square), bSM/dPOPC/Chol = 0.375/0.375/0.25 (circle), and PSM/POPC/Chol= 0.39/0.39/0.22 (diamond).

2.4.4 SANS

SANS measurements of ULVs were performed at several compositions in SM/DOPC/Chol and SM/POPC/Chol, under conditions designed to detect the formation of Ld+Lo domains. Figure C.1 shows a schematic diagram of the experiment. Briefly, SANS arises from three additive components [47]: (1) a mean component from scattering length density (SLD) contrast between the average bilayer composition and the solvent; (2) a radial component from SLD variation in the direction normal to the bilayer plane (we note that the radial SLD profile of a lipid bilayer can be approximated by two slabs corresponding to the headgroup and acyl chain regions); and (3) a lateral component from in-plane SLD variation. The total scattered intensity due to each component is proportional to the square of the corresponding SLD contrast. SLD of the solvent and acyl chains can be controlled experimentally, by adjusting the ratio of D_2O/H_2O in the aqueous medium, and the ratio of deuterated/protiated chains in the bilayer. We selectively deuterated only one component, either the high-Tm or low-Tm lipid. We matched the average SLD of the solvent and acyl chain region, such that random mixing of lipids within the plane of the bilayer resulted in a nearly contrast-free system with minimal scattering (additional details are found in Appendix C.1 and Table C.1). Upon domain formation, the lateral segregation of high- and low-Tm species generated in-plane contrast, resulting in increased scattering. Contrast matching conditions were verified experimentally, as described in Appendix C.2 and shown in Fig. C.2. Sample compositions, SLD values, and contrast match conditions for data in Figs. 2.7 and 2.8 are listed in Tables C.2 and C.3, respectively.

2.4.4.1 PSM/DOPC/Chol and bSM/POPC/Chol

Figure 2.7 shows a comparison of SANS scattering curves for two compositions in PSM-d31 (dPSM)/DOPC/Chol, and two compositions in bSM/POPC-d31 (dPOPC)/Chol, at 25°C. The DOPC-containing compositions dPSM/DOPC/Chol = 0.40/0.43/0.17 (Fig. 2.7, downward-pointing triangles) and 0.54/0.20/0.26 (Fig. 2.7, upward-pointing triangles) were chosen to lie on an Ld+Lo tieline determined with FRET, and are marked with the same symbols on the phase diagram in Fig. 2.6. As expected, enhanced scattering at low q indicates lateral segregation of dPSM and DOPC, consistent with observations of phase separation at these compositions in FRET experiments. The total scattered intensity $Q=\int Iq^2 dq$ (Appendix C.3) is larger for the composition dPSM/DOPC/Chol = 0.40/0.43/0.17 (Fig. 2.7, downward-pointing triangles) than 0.54/0.20/0.26 (Fig. 2.7, upward-pointing triangles), which is likely due to differences in domain area fraction for these samples. The in-plane contribution to Q scales with the product of the domain area fraction α and surround area fraction $(\alpha-1)$ [47], and therefore exhibits a maximum when phase fractions are equal. Using the proposed tieline endpoints and applying the Lever Rule, the expected domain area fractions for the compositions dPSM/DOPC/Chol = 0.54/0.20/0.26 and 0.40/0.43/0.17 are ~ 0.19 Ld phase and ~0.45 Lo phase, respectively. Area fractions were calculated using area per lipid values of 60 $Å^2$ for Ld phase (estimated from MD simulations found in [48]) and 45 $Å^2$ for Lo phase (estimated from the value for pure stearoyl-SM (SSM) found in [49]).

Two compositions in bSM/dPOPC/Chol were chosen for SANS experiments, based on FRET results indicating Ld+Lo coexistence at 25°C. The composition bSM/dPOPC/Chol = 0.54/0.20/0.26 (Fig. 2.7, squares) directly corresponds to one of the DOPC-containing samples (Fig. 2.7, upward-pointing triangles). The composition bSM/dPOPC/Chol =0.375/0.375/0.25 (Fig. 2.7, circles) was chosen to facilitate a comparison with the literature (see Discussion). Both compositions are marked on the phase diagram in Fig. 2.6. In stark contrast to the DOPC-containing compositions, essentially no scattering is observed for these compositions at 25°C (expanded in Fig.

2.7 inset). The spatial detection limit of domain detection for SANS depends on several factors, including the volume fractions of the coexisting phases and the contrast between domain and surround, which is in turn affected by partitioning of the deuterated lipid. Previous studies have detected in-plane scattering from domains with radii as small as ~ 7 nm [10,50]. We therefore conclude that domain radii at both compositions for bSM/dPOPC/Chol cannot be larger than ~ 7 nm. This negative SANS result is consistent with our FRET results indicating liquid domains on the 2−6 nm size scale.

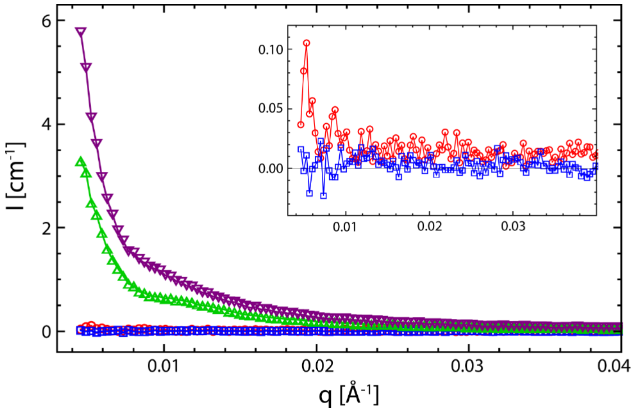

Figure 2.7 SANS reveals membrane domains at 25°C for two compositions in SM/DOPC/Chol, but not in SM/POPC/Chol. Scattering curves for dPSM/DOPC/Chol = 0.54/0.20/0.26 (upward-pointing triangles) and dPSM/DOPC/Chol =0.40/0.43/0.17 (downward-pointing triangles), bSM/dPOPC/Chol = 0.54/0.20/0.26 (squares), and bSM/dPOPC/Chol = 0.375/0.375/0.25 (circles). Excess scattering from domains larger than ~ 7 nm radius (the SANS resolution limit) is seen for the DOPC-containing but not the POPC-containing compositions (expanded in inset). Compositions are shown on the phase diagrams in Fig. 2.6. Experimental contrast series are shown in Fig. C.2. Sample compositions, scattering length densities, and contrast match conditions are listed in Table C.2.

2.4.4.2 PSM/POPC/Chol

Brain SM contains a mixture of chain lengths, and exhibits a broad melting transition (Figs. B.1-B.2). We prepared additional SANS samples in SM/POPC/Chol using chemically pure PSM. For these samples, we had the choice of using either deuterated POPC or deuterated PSM to provide the lateral contrast. In the former case, dPOPC will partition into the POPC-rich Ld phase, while in the latter case, dPSM will partition into the SM-rich Lo phase. We prepared both types of sample at the composition PSM/POPC/Chol = 0.39/0.39/0.22, and for comparison, dPSM/DOPC/Chol at the same composition.

Figure 2.8 shows total scattered intensity as a function of temperature from 15 to 55°C, for dPSM/POPC/Chol (Fig. 2.8, squares), PSM/dPOPC/Chol (Fig. 2.8, circles), and dPSM/DOPC/Chol (Fig. 2.8, triangles). Sample details appear in Table C.3, and corresponding scattering curves are shown in Fig. C.3. Enhanced scattering from all three samples indicates coexisting domains between 15 and 35°C. Residual scattering at 35 and 45°C is more significant for DOPC- than POPC-containing samples, indicative of incomplete miscibility in the DOPC mixture at high temperature (also seen in the FRET data). Together, the FRET and SANS data suggest a miscibility transition between 35 and 45°C for SM/POPC/Chol, and between 45°C and 55°C for SM/DOPC/Chol. Switching the deuterated species in the mixture PSM/POPC/Chol from PSM (Fig. 2.8, squares) to POPC (Fig. 2.8, circles) results in a significant increase in scattering, consistent with the phase diagram, which indicates stronger partitioning of POPC into Ld phase, compared to the partitioning of PSM into Lo phase. For this reason, dPOPC should provide better contrast than dPSM for detecting domains in SM/POPC/Chol mixtures.

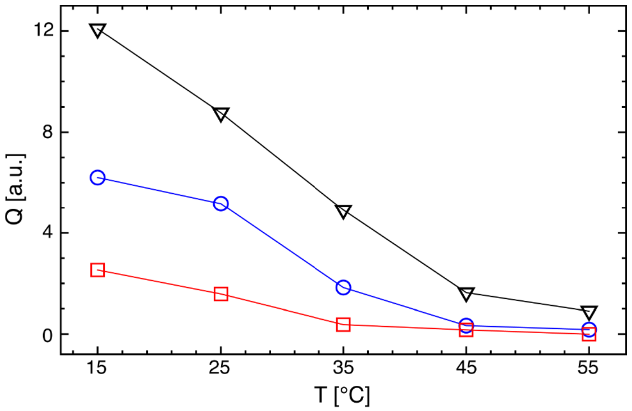

Figure 2.8 SANS reveals phase separation in PSM/POPC/Chol. The total scattered intensity Q vs. temperature for dPSM/POPC/Chol (squares), PSM/dPOPC/Chol (circles), and dPSM/DOPC/Chol (triangles). All compositions have mole fractions 0.39/0.39/0.22. Enhanced scattering in all three samples indicates coexisting domains between 15 and 35°C. Little change in Q from 45-55°C indicates a miscibility transition between 35-45°C for both POPC-containing samples. Residual scattering at 35 and 45°C is more significant for DOPC- than POPC-containing samples. Both results are consistent with FRET. Switching from dPSM (squares) to dPOPC (circles) results in a significant increase in scattering, indicating that POPC partitions more strongly into Ld phase than PSM partitions into Lo phase. dPOPC should provide good contrast for detecting domains if they exist in bSM- or PSM-containing systems. Compositions are shown on the phase diagrams in Fig. 2.6 (diamonds). Scattering curves appear in Fig. C.3. Sample compositions, scattering length densities, and contrast match conditions are listed in Table C.3.

2.5 DISCUSSION

The outer leaflet of the mammalian plasma membrane contains a substantial fraction of SM. Therefore, knowledge of the phase behavior of SM-containing model membranes is of great interest. Accurate phase diagrams provide information about the composition of coexisting phases that is crucial for the design and interpretation of systematic studies of raft phenomena. There are now many published reports of complete or partial phase diagrams for ternary mixtures containing synthetic or natural SM, cholesterol, and a low-Tm lipid (either DOPC or POPC). A comparison of these studies reveals significant differences in the location of phase boundaries, especially for the region of coexisting liquid phases.

The identity of the low-Tm lipid has a profound impact on the size of liquid domains, and we have found that parallel studies on DOPC- and POPC-containing mixtures are especially useful for interpreting composition-dependent trends [8]. In this study, we used FRET and DSC to establish some phase boundaries in bSM/DOPC/Chol and bSM/POPC/Chol at 15 and 25°C. In the following discussion we compare these results to published phase diagrams for SM/DOPC/Chol and SM/POPC/Chol, and address potential sources of discrepancies in phase boundary locations. After accounting for different spatial sensitivities of the various techniques used to establish phase coexistence, broad composition-dependent trends in domain size are revealed, which may have important implications for biological membranes.

2.5.1 Binary Phase Behavior: Comparison of bSM/DOPC and bSM/POPC

The binary phase diagrams determined with DSC (Fig. 2.5) proved useful in constructing the ternary phase diagrams for bSM/DOPC/Chol and bSM/POPC/Chol, by providing constraints on the Ld+Lβ phase boundaries. Binary phase diagrams have previously been determined for PSM/DOPC using DSC and fluorescence properties of *trans*-parinaric acid (tPA) (Nyholm 2011). DSC studies have been conducted on bSM/POPC [16] and bSM/POPC/Chol [51]. The mixture egg SM (eSM)/POPC has been examined with DSC and small- and wide-angle X-ray diffraction [52], and mixtures of PSM/POPC have been studied by fluorescence anisotropy [14,19] and NMR [53]. These studies are in good overall agreement regarding the Ld+Lβ phase boundaries of SM/DOPC and SM/POPC mixtures.

2.5.2 Ternary Phase Behavior of bSM/DOPC/Chol

2.5.2.1 Ld+Lo Region

Ld+Lo phase boundaries are shown in Fig. 2.6. FRET between probes that partition strongly into the Ld phase is particularly useful for determining its onset (*i.e.*, the right-hand boundary). This is clearly the case for BoDIPY-PC and LR-DOPE (Fig. 2.1, upper panel), which show a sharp increase in FRET near the bSM/Chol binary axis, implying that only a small amount of DOPC (< 5 mol%) is required to induce formation of the Ld phase from SM/Chol mixtures. This finding agrees well with phase boundaries determined using fluorescence microscopy of GUVs [29–31]. Using fluorescence lifetime of tPA, Nyholm and coworkers found markedly different phase boundaries for PSM/DOPC/Chol at 23°C, reporting the formation of Ld phase at 15-19 mol% DOPC [54]. However, as pointed out by the authors, the strong partitioning of tPA into ordered phases renders this probe less useful for determining the formation of small amounts of Ld phase.

The upper boundary of the Ld+Lo region at ~ 40 mol% Chol is marked by abrupt changes in FRET for both probe pairs (Fig. 2.1). This result is consistent with fluorescence microscopy results in SSM/DOPC/Chol [31], bSM/DOPC/Chol [30], and PSM/DOPC/Chol [29], as well as tPA lifetime in PSM/DOPC/Chol [54]. The phase boundary extends to above 40 mol% Chol in the three latter studies, which may indicate that these compositions are prone to light-induced phase separation [32].

As observed by others [29,31], we find that the Ld+Lo coexistence region for

SM/DOPC/Chol extends over a broad region of composition space at lower temperature, and narrows at higher temperatures. At the highest temperatures, Ld+Lo phase coexistence persists only at compositions near the REE peak (Fig 2.1.), consistent with the observations by Veatch and Keller [29].

2.5.2.2 Critical Point

We find a ridge of enhanced FRET in single-phase compositions just above the Ld+Lo boundary (Fig. 2.1, upper panel) that persists even to 45°C (Fig. A.1), suggesting a critical point for bSM/DOPC/Chol at ~ 0.30/0.33/0.37. Other studies have found similar critical compositions in SM-containing ternary mixtures. Farkas and Webb used fluorescence microscopy of GUVs and found a critical point at 0.30/0.30/40 in SSM/DOPC/Chol [31]. Tian et al. used micropipette aspiration of GUVs to measure composition-dependent trends in line tension within the Ld+Lo region of eSM/DOPC/Chol that suggested a critical point near 0.26/0.34/0.40 [55]. Using 9.5 GHz ESR, Smith and Freed reported a critical point for bSM/DOPC/Chol at 0.20/0.50/0.30, a substantially higher DOPC content than found in the present study [30]. This is perhaps due to the difficulties inherent in analyzing ESR spectra that are a superposition of Ld and Lo phase components near a critical point, where the coexisting phases have nearly identical physical properties. Moreover, ESR determinations of the critical point location in PSM/POPC/Chol are also shifted to higher fractions of low-Tm lipid [21,23].

2.5.2.3 Tielines

The bSM/DOPC/Chol tieline reported here (33° slope) agrees well with SSM/DOPC/Chol measurements by Farkas and Webb, who used both polarization imaging of GUVs and mass spectrometry on phase patches excised from GUVs [31]. They report a tieline in the Ld+Lo coexistence region with a 37° slope, and suggested that tielines become less steep upon approaching the three-phase triangle where our bSM/DOPC/Chol tieline is approximated. Our bSM/DOPC/Chol tieline is not as steep as the analogous tieline with slope 40° found by Smith and Freed, who used a novel tieline field method to fit fluorescence microscopy and ESR results for bSM/DOPC/Chol [30]. This discrepancy may be due to the methodology used, which relies heavily on the location of the critical point and Ld+Lo boundary for determining tieline slopes: as mentioned previously, the critical point determined by ESR occurs at lower SM and Chol fractions, requiring tielines with greater slopes.

Our bSM/DOPC/Chol tieline is steeper than the corresponding DSPC/DOPC/Chol tieline, which has a 22° slope (Frederick A. Heberle et al. 2010). The difference indicates stronger partitioning of cholesterol into the Lo phase in SM-containing mixtures, in agreement with studies that find a more favorable interaction between Chol and SM, compared to DPPC or DSPC [56,57]. For SM and PC mixtures, the tieline Lo composition is similar, indicating that cholesterol solubility in the gel phase does not depend on the type of high-Tm lipid present. Other studies have found that the disappearance of gel phase at the upper corner of the three-phase triangle occurs at ~ 25-27 mol% Chol for several high-Tm lipids [58,59].

2.5.3 Ternary Phase Behavior of bSM/POPC/Chol

2.5.3.1 Ld+Lo Region and Tielines

FRET experiments for bSM/POPC/Chol were performed under identical conditions to those for bSM/DOPC/Chol. The large FRET peak seen in the interior of the DOPC surface marking the Ld+Lo region (Fig. 2.1, upper panel) is dramatically attenuated in bSM/POPC/Chol (Fig. 2.3, upper panel), an observation consistent with a reduction in domain size upon substituting POPC for DOPC. Qualitatively, the size of domains must be close to the spatial detection limit for FRET, which is approximately the Förster distance for this probe pair (*i.e.*, $R_0 \sim 6$ nm). Weaker partitioning of Ld-preferring probes in POPC mixtures is an alternative explanation for the reduced magnitude of FRET efficiency.

We report a single tieline for bSM/POPC/Chol. As for bSM/DOPC/Chol, this tieline was chosen along the trajectory through the FRET surface features of greatest magnitude (Figs. 2.3, A.3). The tieline endpoints reveal stronger partitioning between Ld and Lo domains for POPC (partition coefficient into Ld phase, Kp ~ 13) than for bSM (Kp ~ 1/3), consistent with our SANS result that a PSM/dPOPC/Chol sample exhibits increased scattering compared to a dPSM/POPC/Chol sample of otherwise identical composition (Fig. 2.8). Although the bSM/POPC/Chol tieline is slightly shorter than the bSM/DOPC/Chol tieline, it lies along the same compositional trajectory, consistent with the analogous tieline in DSPC/DOPC/Chol (Frederick A. Heberle et al. 2010). In that study, we observed that while the length of the tieline followed the trend DOPC > POPC > SOPC, the tieline slope remained constant [8]. Interestingly, the bSM/DOPC/Chol and bSM/POPC/Chol phase diagrams are similar, indicating that changing the low-Tm lipid from DOPC to POPC does not significantly alter the phase diagram. This result is consistent with recent work using a novel FRET technique, which reported similar phase diagrams for DSPC/DOPC/Chol and DSPC/POPC/Chol [60], despite domains being macroscopic in DSPC/DOPC/Chol and nanoscopic in DSPC/POPC/Chol [8,10,11].

2.5.3.2 SANS Detects Liquid Domains in PSM/POPC/Chol, but not bSM/POPC/Chol

Like FRET, SANS relies on the segregation of a "probe" molecule between phase domains. However for SANS, unlike for FRET, the probe is a chain-perdeuterated variant of one of the lipid species. The scattering signal that arises from a non-random lateral distribution of the probe is therefore directly attributable to spatial segregation of the lipids themselves, rather than the inherently indirect observations of lateral heterogeneity made with fluorescence probes. We observed an increase in scattering attributable to Ld+Lo domain formation in PSM/POPC/Chol (Fig. 2.8), but not bSM/POPC/Chol (Fig. 2.7). Monte Carlo simulations indicate that the minimum domain radius detectable by SANS is ~ 7 nm [10,50], which allows us to place an upper limit on domain size in bSM/POPC/Chol of ~ 7 nm radius. Combining our FRET and SANS results, we are able to place a range of 2–6 nm radius on Ld+Lo domains in bSM/POPC/Chol.

2.5.4 Comparison of Published SM/POPC/Chol Phase Diagrams

SM/POPC/Chol is generally recognized as one of the best three-component lipid mixtures for modeling the mammalian outer leaflet [24] and consequently it is among the most studied: at least five published phase diagrams exist for bSM/POPC/Chol [16] and PSM/POPC/Chol [14,19,23,29]. All of these reports find Ld+Lo phase coexistence in the central region of the phase diagram, and most agree on tieline slope just above the three phase region, including the present study and others [19,23,29]. Despite this general similarity, the precise locations of phase boundaries vary considerably, particularly with respect to the region of Ld+Lo coexistence, as demonstrated in Fig. 2.*9B*. Some discrepancies, such as the location of the upper boundary of the three-phase region, are likely due to subjectivity in distinguishing a minor component of a composite signal (*i.e.*, a signal arising from the presence of probe in multiple environments). Aside from such differences, the main distinction between the phase diagrams occurs at low SM fractions, where some diagrams report Ld+Lo phase coexistence extending to the POPC/Chol binary axis [14,19] or very near the binary axis [16], while others (including the present study) do not detect Ld+Lo phase coexistence below 20 mol% SM [23,29]. These discrepancies are significant and merit further consideration.

2.5.4.1 Spatial Sensitivity of Techniques

In studies of lipid phase behavior, an important distinction is often made between ESR and single-probe fluorescence spectroscopies (*i.e.*, fluorescence lifetime, quenching, and quantum yield), which have "nearest neighbor" sensitivity to the immediate environment of the probe, and techniques that require larger-scale clustering of lipids for detection. While the boundaries are somewhat imprecise, the latter category can be subdivided into "nanoscale" (FRET, SANS, delta-lysin induced dye efflux), "mesocale" (NMR), and "macroscale" (fluorescence microscopy) sensitivity (Fig. 2.9*A*). Nearest-neighbor techniques are in principle capable of detecting lipid clustering at all size scales, ranging from compositional fluctuations inherent in any complex mixture, to first-order phase separation with "infinite" sized domains; however, it is not clear that these extremes can be distinguished from *each other*. This is a significant caveat, since domains smaller than a few nanometers consist of only a few shells of lipid, and are unlikely to be subject to the constraints of first-order phase separation implied by phase boundaries and tielines. Furthermore, the size and lifetime of these clusters may be too small and short-lived to achieve the functions ascribed to lipid rafts in cells. For example, a single alpha-helical portion of a transmembrane peptide alone has twelve nearest-neighbor lipids [61–63] and would therefore require a raft comprising at least this many lipids to be considered as part of the phase comprising that lipid.

An additional issue with fluorescence-based techniques is that it is often challenging to distinguish between continuous variation in the fluorescence signal due to gradual changes in interfacial polarity and chain order that accompany changes in mixture composition, versus abrupt changes due to a first-order phase transition and the onset of a new chemical environment. This is particularly true if probe partitioning between the two environments is nearly uniform. For this reason, data at high compositional resolution (such as our FRET surfaces) can be of great benefit. Furthermore, our temperature-dependent results for bSM/DOPC/Chol and bSM/POPC/Chol permit comparison of bSM/POPC/Chol FRET surfaces in question with FRET surfaces exhibiting well-established first order phase transitions (bSM/DOPC/Chol at 15 and 25°C, Fig. 2.1) and known small-scale heterogeneity (bSM/DOPC/Chol at 45°C, Fig. A.1). Indeed, it is often more robust to interpret *variation* in a FRET signal, as we have done here, rather than absolute magnitude. We find that FRET detects heterogeneity in bSM/POPC/Chol at 15 and 25°C that disappears at 35°C. Comparing the FRET results for bSM/DOPC/Chol and bSM/POPC/Chol (Figs. 2.1-2.4, A.1-A.3), it is clear that no large-scale separation of phase domains is present for bSM/POPC/Chol. Instead, domains at the lower temperatures are evidently on the size scale of R_0 for these probe pairs, or ~ 2–6 nm.

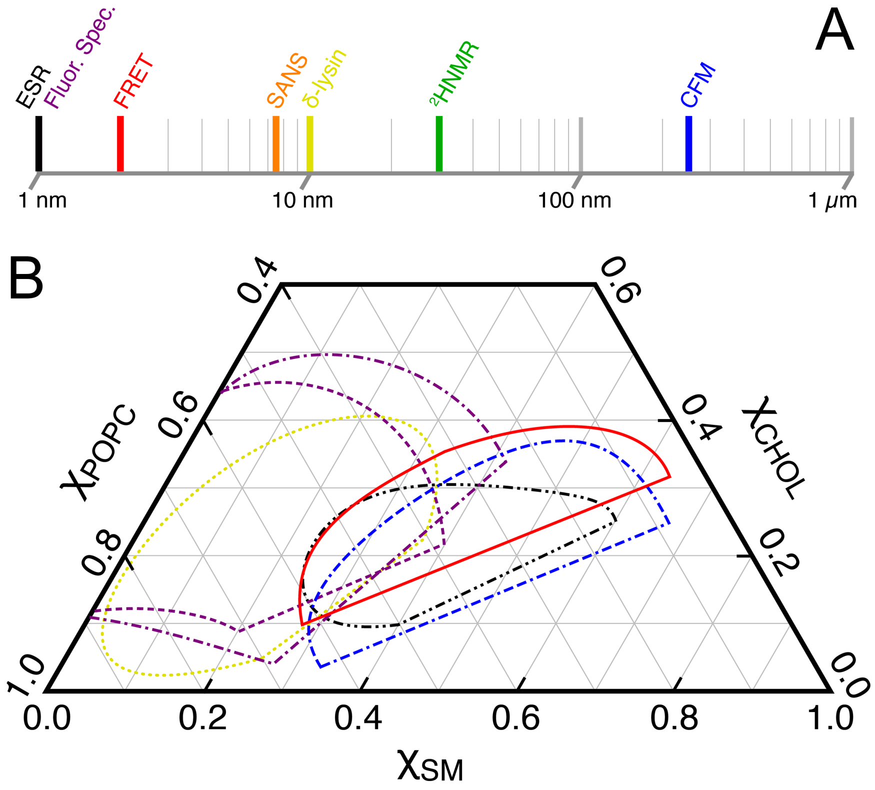

Figure 2.9 Spatial sensitivities of techniques used to determine Ld+Lo phase coexistence regions for SM/POPC/Chol at 23°C. *A* Techniques used to investigate Ld+Lo phase coexistence are sensitive to heterogeneity on different size scales. *B* Phase diagrams for SM/POPC/Chol at 23°C determined with techniques including FRET (bSM, solid, this publication), delta-lysin release kinetics (bSM, dotted) [16], electron spin resonance (PSM, dot dot dash) [23], confocal fluorescence microscopy (PSM, dash dash dot) [29], fluorescence anisotropy (PSM, dashed) [19], and fluorescence anisotropy and quenching (PSM, dot-dashed) [14].

2.5.4.2 Effect of Probes

Extrinsic probes may perturb the native phase behavior of a lipid mixture, to an extent that depends not only on the identity and concentration of the probe, but also on the properties of the mixture itself. For example, ternary mixtures containing POPC, Chol, and a variety of SM species have a strong tendency to form large domains in the presence of intensely illuminated fluorescent probes [32]. Veatch and coworkers reported that impurities can stabilize Ld+Lo phase coexistence at higher temperatures [34]. Hammond et al. found that cross-linking the minor impurity ganglioside GM1 (< 2 mol%) with cholera toxin B subunit increased domain size in bSM/DOPC/dioleoylphosphatidylglycerol (DOPG)/Chol and expanded the Ld+Lo phase coexistence region [64]. In light of these findings, it is reasonable to believe that with 4 mol% quencher, domains smaller than the detection limit in the native lipid system (*i.e.*, without quencher) could be sufficiently perturbed to form detectable domains in the presence of a quencher [14]. Similarly, a 0.25 mol% concentration of delta-lysin, while perhaps minimally perturbing in a randomly mixed bilayer, might become extremely perturbative upon partitioning, as described, 1000-fold into Ld phase [16].

The question remains as to whether the native SM/POPC/Chol system exhibits true first-order phase separation. The studies with the smallest concentrations of extrinsic probes (*i.e.*, our bSM/POPC/Chol study with Chol-analogue DHE and 0.05 mol% Ld-preferring fluorescent probes, and Ionova et al. PSM/POPC/Chol with 0.5 mol% spin label) are consistent with first-order phase separation [23]. Theoretical models and some methods for measuring domain size require or benefit from conducting analysis on a thermodynamic tieline, along which the compositions of the coexisting phases remain constant. However, it is important to note that these constraints do not strictly hold in quasi-ternary systems where the SM species is a natural mixture, or the probe and peptide concentrations are present in significant amounts. In these systems, there may be a gradual change from small-scale heterogeneity or domains on the POPC/Chol binary axis, to larger domains in the Ld+Lo region of the ternary SM/POPC/Chol system. The boundaries detected by various methods reflect the compositions at which domains become large enough to be detected *via* the method employed. The variability in reported phase diagrams highlights not only differences in technique sensitivity, but also the natural tendency for SM/POPC/Chol mixtures to separate into larger domains upon perturbation.

2.5.5 Nanodomain Size in SM/POPC/Chol

In addition to the thermodynamic information contained in the phase diagram, the size, morphology, and dynamics of membrane domains likely play a crucial role in the biological functions of rafts. An abundance of evidence points toward coexisting fluid domains in SM/POPC/Chol, with sizes much smaller than the wavelength of visible light. In particular, the absence of visible phase separation with light microscopy implies domains smaller than the optical resolution limit of ~ 200 nm. The physico-chemical properties of rafts, including their intrinsic stability, strongly depend on where their size falls within the “nanodomain regime” of ~2-200 nm: Are they small clusters of tens of lipids, with poorly-defined boundaries and only minor differences in properties compared to the surrounding sea? Or are they large aggregates of tens of thousands of lipids, with a well-defined interior environment that differs significantly from the surrounding bilayer?

Several domain size measurements have been made at or near the “canonical” raft composition 1:1 SM:POPC with 20-35 mol% Chol. An early report of micron-sized domains [29] was subsequently revealed to be an artifact of photo-induced lipid breakdown [32]. Using a FRET-based model, de Almeida et al. reported 75-100 nm domains (or ~10,000 lipids per leaflet) for compositions near the equimolar mixture

PSM/POPC/Chol= 0.33/0.33/0.33 at 23°C [15]. This result was supported by an ^{2}H-NMR study, which reported a minimum domain size of 45-70 nm for a similar composition at 37°C [20]. A solid state NMR study found no domains at this composition for bSM/POPC/Chol [65], and others have interpreted these results to suggest domains on the order of < 10 nm [16]. Bartels et al. detected domains in PSM/POPC/Chol = 0.40/0.40/0.20 with ^{2}H-NMR, but did not detect domains at higher cholesterol concentrations, or at temperatures above 25°C [66]. A study employing delta-lysin release kinetics suggested domain sizes on the order of the peptide length of ~ 4 nm at several compositions, including bSM/POPC/Chol=0.40/0.30/0.30 [16]. More recently, Pathak and London recognized that the loss of a FRET signal as a function of increasing R_0 could be used to infer domain size, using a limit-of-detection argument. They reported a decrease of domain size from 8–10 to < 4 nm between 25 and 37°C in bSM/POPC/Chol=0.33/0.33/0.33 [22]. To summarize these studies, a range of domain sizes spanning two orders of magnitude has been reported for similar raft compositions at similar temperatures.

By combining data from FRET and SANS, two fundamentally different techniques with different minimum spatial sensitivities, we were able to constrain domain sizes in bSM/POPC/Chol to between 2 and 7 nm radius. Our FRET results alone do not strictly rule out larger phase domains. If probes do not partition strongly between phase domains, or if domains are smaller than the Förster distance in at least one spatial dimension, FRET efficiency will not vary significantly in a phase coexistence region. Compositional variation in FRET for bSM/POPC/Chol is much less than for bSM/DOPC/Chol, but it is decidedly present. Given the Förster distances of our FRET pairs, domains cannot be much smaller than 2 nm and still be detectable by FRET, while domains larger than 7 nm would be detected with SANS. Our combined results therefore limit the size scale of membrane domains in bSM/POPC/Chol to a range of 2–7 nm, or ~ 25-300 lipids per leaflet. This is similar to the result from Pathak and London of 8–10 nm at 25°C, and markedly different from other estimates mentioned previously.

An important finding is that SANS detected nanodomains in PSM/POPC/Chol, but not in bSM/POPC/Chol. This result is consistent with a number of studies, concluding that the structural details of SM may play an important role in membrane spatial organization. An NMR study of ternary mixtures consisting of a natural SM with DOPC and Chol found a broader compositional range of liquid phase coexistence for eSM than for bSM, and no liquid coexistence for milk-SM [67]. Farkas has reported significantly higher chain order in GUVs comprising SSM mixtures, compared to bSM mixtures [68]. Higher chain order could indicate that pure SM species (including PSM and SSM) mix more poorly with low-Tm lipids, giving rise to larger domains. While the origin of specific SM/Chol interactions is not yet known, hydrogen bonding, lipid packing, and hydrophobic mismatch are likely to play a role [25,69]. Understanding the significance of each factor will aid in interpreting studies that report compositional heterogeneity in ternary SM/POPC/Chol mixtures with some SM species, but not others.

Comparisons between bSM- and DSPC-containing ternary systems indicate other significant differences that depend on the nature of the high-Tm lipid. For example, lipid analogs with long saturated chains and headgroup labels such as 1,1-dieicosanyl-3,3,3,3-tetramethylindocarbocyanine perchlorate (DiI-C20:0), prefer ordered phases in DSPC/DOPC/Chol but not in bSM/DOPC/Chol [70]. Though both systems exhibit macroscopic phase separation, their ordered phases may differ in other respects: while SM and DSPC share the same choline headgroup, it seems that the SM headgroup region is more ordered and unable to accommodate bulky probes in Lo phases with bSM, compared to DSPC [71]. Indeed, MD simulations indicate greater

Lo phase order in the interfacial region for SM than saturated PC species [72], though the origins of Chol preference for SM over saturated PC species remains ambiguous [69,73]. SM and PC species have the same headgroup, but they have different backbones linking the headgroup with the acyl chains. In particular, the SM link is capable of forming hydrogen bonds with Chol. When this link is replaced by the PC link, the interaction between SM and Chol decreases significantly, as detected by fluorescence spectroscopy [74].

2.5.6 Biological Relevance

Our studies conclusively demonstrate that Ld+Lo phase coexistence in bSM/POPC/Chol results in domains between 2–7 nm in radius. These domains contain fewer than 300 lipids per leaflet, a finding that could have important consequences for the ability of membrane-associated proteins to find their substrates: even if both molecules partition into the same phase, the phase domain may not be large enough for binding partners to interact with each other. If, however, phase domains grow larger upon an external stimulus, the molecules can then find each other. This is a very different picture than previous domain size measurements, which reported domains with ~10,000 lipids per leaflet [15]. As mentioned, SM/POPC/Chol mixtures are uncommonly prone to artifactual phase separation. We are not the first to speculate that the lipid composition of plasma membranes may be tuned to the brink of a transition, poised to separate into larger structures upon slight perturbation (here we refer to size transitions, not phase transitions). In this study, we provide evidence for the existence of such small domains in probe-free model membranes. Future combined FRET and SANS studies should prove useful for examining changes in domain size, such as those induced by lipid composition or external crosslinking.

2.6 CONCLUSIONS

1. FRET establishes the presence of Ld+Lo and Lo+Lβ coexistence regions in bSM/DOPC/Chol bilayers at 35°C and lower. At 45°C, FRET reports miscibility over the entire composition space.

2. For both donor/acceptor pairs used in this study, FRET does not detect Ld+Lβ phase coexistence at low Chol concentration. However, DSC confirms the existence of phase separation in this region.

3. Our FRET results are consistent with Ld+Lo coexistence in bSM/POPC/Chol. Compositional trends in FRET data indicate domain formation on the order of the Förster distance R_0 ~ 2–6 nm for these probe pairs, while SANS is consistent with complete lipid miscibility. Taking into account the different spatial sensitivities of these techniques, the data are consistent with the presence of domains no larger than ~ 7 nm in radius.

4. Upon replacing the natural bSM mixture with synthetic PSM, SANS reports domain formation for the composition PSM/POPC/Chol = 0.39/0.39/0.22. We conclude that size of Ld+Lo nanodomains is exquisitely sensitive to details of the structure of the high melting temperature lipid. Researchers should be aware that the choice of SM—natural versus chemically pure—can have profound consequences for the detailed nature of any coexisting phase domains.

2.7 REFERENCES

[1] K. Simons, E. Ikonen, Functional rafts in cell membranes, Nature, 387 (1997) 569–572.

[2] D.A. Brown, E. London, Structure and function of sphingolipid- and cholesterol-rich membrane rafts, The Journal of Biological Chemistry, 275 (2000) 17221–4.

[3] C. Eggeling, C. Ringemann, R. Medda, G. Schwarzmann, K. Sandhoff, S. Polyakova, V.N. Belov, B. Hein, C. von Middendorff, A. Schönle, S.W. Hell, Direct observation of the nanoscale dynamics of membrane lipids in a living cell, Nature, 457 (2009) 1159–62.

[4] E.L. Elson, E. Fried, J.E. Dolbow, G.M. Genin, Phase separation in biological membranes: integration of theory and experiment, Annual Review of Biophysics, 39 (2010) 207.

[5] H.-J. Kaiser, D. Lingwood, I. Levental, J.L. Sampaio, L. Kalvodova, L. Rajendran, K. Simons, Order of lipid phases in model and plasma membranes, Proceedings of the National Academy of Sciences, 106 (2009) 16645–50.

[6] D. Lingwood, K. Simons, Lipid rafts as a membrane-organizing principle, Science, 327 (2010) 46–50.

[7] F.A. Heberle, G.W. Feigenson, Phase separation in lipid membranes, in: K. Simons (Ed.), Cold Spring Harbor Perspectives: The Biology of Lipids, 2011.

[8] F.A. Heberle, J. Wu, S.L. Goh, R.S. Petruzielo, G.W. Feigenson, Comparison of three ternary lipid bilayer mixtures: FRET and ESR reveal nanodomains, Biophysical Journal, 99 (2010) 3309–3318.

[9] T.M. Konyakhina, S.L. Goh, J. Amazon, F.A. Heberle, J. Wu, G.W. Feigenson, Control of a Nanoscopic-to-Macroscopic Transition: Modulated Phases in Four-Component DSPC/DOPC/POPC/Chol Giant Unilamellar Vesicles, Biophysical Journal, 101 (2011) L8–L10.

[10] F.A. Heberle, R.S. Petruzielo, J. Pan, P. Drazba, N. Kucerka, R.F. Standaert, G.W. Feigenson, J. Katsaras, Bilayer thickness mismatch controls raft size in model membranes, Submitted, (2012).

[11] J. Zhao, J. Wu, F.A. Heberle, T.T. Mills, P. Klawitter, G. Huang, G. Costanza, G.W. Feigenson, Phase studies of model biomembranes: complex behavior of DSPC/DOPC/cholesterol, Biochimica Et Biophysica Acta, 1768 (2007) 2764–76.

[12] R.B. Gennis, Biomembranes: Molecular Structure and Function, Springer-Verlag, New York, 1989.

[13] J.R. Silvius, Fluorescence Energy Transfer Reveals Microdomain Formation at Physiological Temperatures in Lipid Mixtures Modeling the Outer Leaflet of the Plasma Membrane, Biophysical Journal, 85 (2003) 1034–1045.

[14] R.F.M. de Almeida, A. Fedorov, M. Prieto, Sphingomyelin/ phosphatidylcholine/ cholesterol phase diagram: boundaries and composition of lipid rafts, Biophysical Journal, 85 (2003) 2406–16.

[15] R.F.M. de Almeida, L.M.S. Loura, A. Fedorov, M. Prieto, Lipid rafts have different sizes depending on membrane composition: a time-resolved fluorescence resonance energy transfer study, Journal of Molecular Biology, 346 (2005) 1109–20.

[16] A. Pokorny, L.E. Yandek, A.I. Elegbede, A. Hinderliter, P.F.F. Almeida, Temperature and composition dependence of the interaction of delta-lysin with ternary mixtures of sphingomyelin/cholesterol/POPC, Biophysical Journal, 91 (2006) 2184–97.

[17] M.L. Frazier, J.R. Wright, A. Pokorny, P.F.F. Almeida, Investigation of domain formation in sphingomyelin/cholesterol/POPC mixtures by fluorescence resonance energy transfer and Monte Carlo simulations, Biophysical Journal, 92 (2007) 2422–33.

[18] A.C. Brown, K.B. Towles, S.P. Wrenn, Measuring Raft Size as a Function of Membrane Composition in PC-Based Systems: Part II - Ternary Systems, Langmuir, 23 (2007) 11188.

[19] K.K. Halling, B. Ramstedt, J.H. Nyström, J.P. Slotte, T.K.M. Nyholm, Cholesterol interactions with fluid-phase phospholipids: effect on the lateral organization of the bilayer, Biophysical Journal, 95 (2008) 3861–71.

[20] A. Bunge, P. Müller, M. Stöckl, A. Herrmann, D. Huster, P. Muller, Characterization of the ternary mixture of sphingomyelin, POPC, and cholesterol: support for an inhomogeneous lipid distribution at high temperatures, Biophysical Journal, 94 (2008) 2680–90.

[21] V.A. Livshits, I. V. Demisheva, D. Marsh, Self-organization and phase structure of ternary lipid membranes: A spin label EPR study, Nanotechnologies in Russia, 5 (2010) 601–610.

[22] P. Pathak, E. London, Measurement of Lipid Nanodomain (Raft) Formation and Size in Sphingomyelin/POPC/Cholesterol Vesicles Shows TX-100 and

Transmembrane Helices Increase Domain Size by Coalescing Preexisting Nanodomains But Do Not Induce Domain Formation, Biophysical Journal, 101 (2011) 2417–2425.

[23] I. V. Ionova, V.A. Livshits, D. Marsh, Phase Diagram of Ternary Cholesterol/ Palmitoylsphingomyelin/ Palmitoyloleoyl-Phosphatidylcholine Mixtures: Spin-Label EPR Study of Lipid-Raft Formation, Biophysical Journal, 102 (2012) 1856–1865.

[24] G.W. Feigenson, Phase boundaries and biological membranes, Annual Review of Biophysics and Biomolecular Structure, 36 (2007) 63–77.

[25] P.S. Niemelä, M.T. Hyvönen, I. Vattulainen, Atom-scale molecular interactions in lipid raft mixtures, Biochimica Et Biophysica Acta, 1788 (2009) 122–35.

[26] C. Dietrich, L.A. Bagatolli, Z.N. Volovyk, N.L. Thompson, M. Levi, K. Jacobson, E. Gratton, Lipid rafts reconstituted in model membranes, Biophysical Journal, 80 (2001) 1417–28.

[27] T. Baumgart, S.T. Hess, W.W. Webb, Imaging coexisting fluid domains in biomembrane models coupling curvature and line tension, Nature, 425 (2003) 821–4.

[28] N. Kahya, D. Scherfeld, K. Bacia, B. Poolman, P. Schwille, Probing lipid mobility of raft-exhibiting model membranes by fluorescence correlation spectroscopy, The Journal of Biological Chemistry, 278 (2003) 28109–15.

[29] S.L. Veatch, S.L. Keller, Miscibility Phase Diagrams of Giant Vesicles Containing Sphingomyelin, Physical Review Letters, 94 (2005) 148101.

[30] A.K. Smith, J.H. Freed, The Determination of Tie-Line Fields for Coexisting Lipid Phases: an ESR Study, Journal of Physical Chemistry B, 113 (2009) 3957–3971.

[31] E.R. Farkas, W.W. Webb, Precise and millidegree stable temperature control for fluorescence imaging: application to phase transitions in lipid membranes, The Review of Scientific Instruments, 81 (2010) 093704.

[32] J. Zhao, J. Wu, H. Shao, F. Kong, N. Jain, G. Hunt, G.W. Feigenson, Phase studies of model biomembranes: macroscopic coexistence of Lalpha+Lbeta, with light-induced coexistence of Lalpha+Lo Phases, Biochimica Et Biophysica Acta, 1768 (2007) 2777–86.

[33] A.G. Ayuyan, F.S. Cohen, Lipid peroxides promote large rafts: effects of excitation of probes in fluorescence microscopy and electrochemical reactions during vesicle formation, Biophysical Journal, 91 (2006) 2172–83.

[34] S.L. Veatch, S.S.W. Leung, R.E.W. Hancock, J.L. Thewalt, Fluorescent probes alter miscibility phase boundaries in ternary vesicles, Journal of Physical Chemistry B, 111 (2007) 502–4.

[35] N.F. Morales-Penningston, J. Wu, E.R. Farkas, S.L. Goh, T.M. Konyakhina, J.Y. Zheng, W.W. Webb, G.W. Feigenson, GUV Preparation and Imaging: Minimizing Artifacts, Biochimica Et Biophysica Acta, 1798 (2010) 1324–1332.

[36] J.T. Buboltz, G.W. Feigenson, A novel strategy for the preparation of liposomes: rapid solvent exchange, Biochimica Et Biophysica Acta, 1417 (1999) 232–45.

[37] J.T. Buboltz, C. Bwalya, K. Williams, M. Schutzer, High-resolution mapping of phase behavior in a ternary lipid mixture: do lipid-raft phase boundaries depend on the sample preparation procedure?, Langmuir, 23 (2007) 11968–71.

[38] F.A. Heberle, J.T. Buboltz, D. Stringer, G.W. Feigenson, Fluorescence methods to detect phase boundaries in lipid bilayer mixtures, Biochimica Et Biophysica Acta, 1746 (2005) 186–192.

[39] J.T. Buboltz, Steady-state probe-partitioning fluorescence resonance energy transfer: A simple and robust tool for the study of membrane phase behavior, Physical Review E, 76 (2007) 021903.

[40] E.B. Ferreira, M.L. Lima, E.D. Zanotto, DSC Method for Determining the Liquidus Temperature of Glass-Forming Systems, Journal of the American Ceramic Society, 93 (2010) 3757–3763.

[41] D.M. Price, Temperature Calibration of Differential Scanning Calorimeters, Journal of Thermal Analysis, 45 (1995) 1285–1296.

[42] N. Kucerka, J. Pencer, J.N. Sachs, J.F. Nagle, J. Katsaras, Curvature effect on the structure of phospholipid bilayers, Langmuir, 23 (2007) 1292–9.

[43] G.W. Feigenson, J.T. Buboltz, Ternary Phase Diagram of Dipalmitoyl-PC/Dilauroyl-PC/Cholesterol: Nanoscopic Domain Formation Driven by Cholesterol, Biophysical Journal, 80 (2001) 2775–2788.

[44] D. Wüstner, Fluorescent sterols as tools in membrane biophysics and cell biology, Chemistry and Physics of Lipids, 146 (2007) 1–25.

[45] K.P. Shaw, N.J. Brooks, J.A. Clarke, O. Ces, J.M. Seddon, R. V. Law, Pressure–temperature phase behaviour of natural sphingomyelin extracts, Soft Matter, 8 (2012) 1070.

[46] R. Koynova, M. Caffrey, Phases and phase transitions of the phosphatidylcholines, Biochimica Et Biophysica Acta, 1376 (1998) 91–145.

[47] V.N.P. Anghel, N. Kučerka, J. Pencer, J. Katsaras, Scattering from laterally heterogeneous vesicles II The form factor, Journal of Applied Crystallography, 40 (2007) 513–525.

[48] M. Alwarawrah, J. Dai, J. Huang, A molecular view of the cholesterol condensing effect in DOPC lipid bilayers, The Journal of Physical Chemistry B, 114 (2010) 7516–23.

[49] P.R. Maulik, P.K. Sripada, G.G. Shipley, Structure and thermotropic properties of hydrated N-stearoyl sphingomyelin bilayer membranes, Biochimica Et Biophysica Acta, 1062 (1991) 211–9.

[50] J. Pencer, T. Mills, V. Anghel, S. Krueger, R.M. Epand, J. Katsaras, Detection of submicron-sized raft-like domains in membranes by small-angle neutron scattering, The European Physical Journal E, Soft Matter, 18 (2005) 447–58.

[51] P.E. Milhiet, M.-C. Giocondi, C. Le Grimellec, Cholesterol is not crucial for the existence of microdomains in kidney brush-border membrane models, The Journal of Biological Chemistry, 277 (2002) 875–8.

[52] G. Degovics, A. Latal, E. Prenner, M. Kriechbaum, K. Lohner, Structure and Thermotropie Behaviour of Mixed Choline Phospholipid Model Membranes, Journal of Applied Crystallography, 30 (1997) 776–780.

[53] T. Mehnert, K. Jacob, R. Bittman, K. Beyer, Structure and lipid interaction of N-palmitoylsphingomyelin in bilayer membranes as revealed by 2H-NMR spectroscopy, Biophysical Journal, 90 (2006) 939–46.

[54] T.K.M. Nyholm, D. Lindroos, B. Westerlund, J.P. Slotte, Construction of a DOPC/PSM/Cholesterol Phase Diagram Based on the Fluorescence Properties of trans-Parinaric Acid, Langmuir, 27 (2011) 8339–50.

[55] A. Tian, C. Johnson, W. Wang, T. Baumgart, Line Tension at Fluid Membrane Domain Boundaries Measured by Micropipette Aspiration, Physical Review Letters, 98 (2007) 18–21.

[56] B. Ramstedt, J.P. Slotte, Interaction of Cholesterol with Sphingomyelins and Acyl-Chain-Matched Phosphatidylcholines: A Comparative Study of the Effect of the Chain Length, Biophysical Journal, 76 (1999) 908–915.

[57] B.Y. van Duyl, D. Ganchev, V. Chupin, B. de Kruijff, J.A. Killian, Sphingomyelin is much more effective than saturated phosphatidylcholine in excluding unsaturated phosphatidylcholine from domains formed with cholesterol, FEBS Letters, 547 (2003) 101–106.

[58] F. Liu, I.P. Sugar, P.L. Chong, Cholesterol and Ergosterol Superlattices in Three-Component Liquid Crystalline Lipid Bilayers as Revealed by Dehydroergosterol Fluorescence, Biophysical Journal, 72 (1997) 2243–2254.

[59] P.L.-G. Chong, W. Zhu, B. Venegas, On the lateral structure of model membranes containing cholesterol, Biochimica Et Biophysica Acta, 1788 (2009) 2–11.

[60] T.M. Konyakhina, J. Wu, J.D. Mastroianni, F.A. Heberle, G.W. Feigenson, Phase Diagram of a Four-Component Lipid Mixture: DSPC/DOPC/POPC/Chol, Submitted, (2012).

[61] T.B. Woolf, Molecular dynamics of individual alpha-helices of bacteriorhodopsin in dimyristol phosphatidylocholine I Structure and dynamics, Biophysical Journal, 73 (1997) 2376–2392.

[62] K. Hristova, W.C. Wimley, V.K. Mishra, G.M. Anantharamiah, J.P. Segrest, S.H. White, An amphipathic alpha-helix at a membrane interface: a structural study using a novel X-ray diffraction method, Journal of Molecular Biology, 290 (1999) 99–117.

[63] W.K. Subczynski, M. Pasenkiewicz-Gierula, R.N. McElhaney, J.S. Hyde, A. Kusumi, Molecular dynamics of 1-palmitoyl-2-oleoylphosphatidylcholine membranes containing transmembrane alpha-helical peptides with alternating leucine and alanine residues, Biochemistry, 42 (2003) 3939–48.

[64] A.T. Hammond, F.A. Heberle, T. Baumgart, D. Holowka, B. Baird, G.W. Feigenson, Crosslinking a lipid raft component triggers liquid ordered-liquid disordered phase separation in model plasma membranes, Proceedings of the National Academy of Sciences, 102 (2005) 6320–5.

[65] F. Aussenac, M. Tavares, E.J. Dufourc, Cholesterol dynamics in membranes of raft composition: a molecular point of view from 2H and 31P solid-state NMR, Biochemistry, 42 (2003) 1383–90.

[66] T. Bartels, R.S. Lankalapalli, R. Bittman, K. Beyer, M.F. Brown, Raftlike mixtures of sphingomyelin and cholesterol investigated by solid-state 2H NMR spectroscopy, Journal of the American Chemical Society, 130 (2008) 14521–14532.

[67] G. Lindblom, G. Orädd, A. Filippov, Lipid lateral diffusion in bilayers with phosphatidylcholine, sphingomyelin and cholesterol An NMR study of dynamics and lateral phase separation, Chemistry and Physics of Lipids, 141 (2006) 179–84.

[68] E.R. Farkas, Optical Techniques Illuminate Phase Behavior in Model Membranes, Cornell University, 2010.

[69] J. Aittoniemi, P.S. Niemelä, M.T. Hyvönen, M. Karttunen, I. Vattulainen, Insight into the putative specific interactions between cholesterol, sphingomyelin, and palmitoyl-oleoyl phosphatidylcholine, Biophysical Journal, 92 (2007) 1125–37.

[70] T. Baumgart, G. Hunt, E.R. Farkas, W.W. Webb, G.W. Feigenson, Fluorescence probe partitioning between Lo/Ld phases in lipid membranes, Biochimica Et Biophysica Acta, 1768 (2007) 2182–2194.

[71] K. Simons, W.L.C. Vaz, Model systems, lipid rafts, and cell membranes, Annual Review of Biophysics and Biomolecular Structure, 33 (2004) 269–95.

[72] P. Niemelä, M.M.T. Hyvönen, I. Vattulainen, Structure and dynamics of sphingomyelin bilayer: insight gained through systematic comparison to phosphatidylcholine, Biophysical Journal, 87 (2004) 2976–2989.

[73] S. Bhattacharya, S. Haldar, Interactions between cholesterol and lipids in bilayer membranes Role of lipid headgroup and hydrocarbon chain-backbone linkage, Biochimica Et Biophysica Acta, 1467 (2000) 39–53.

[74] G. M'Baye, Y. Mély, G. Duportail, A.S. Klymchenko, Liquid ordered and gel phases of lipid bilayers: fluorescent probes reveal close fluidity but different hydration, Biophysical Journal, 95 (2008) 1217–25.

Chapter 3
Electron Spin Resonance Results are Consistent with Ld+Lo Compositional Heterogeneity in bSM/POPC/Chol

3.1 ABSTRACT

We employed electron spin resonance (ESR) spectroscopy, a technique sensitive to local environment, to investigate heterogeneity in the liquid-disordered (Ld) + liquid-ordered (Lo) coexistence region of porcine brain sphingomyelin (bSM)/dioleoyl-*sn*-glycero-3-phosphocholine (DOPC)/cholesterol (Chol) and bSM/1-palmitoyl-2-oleoyl-*sn*-glycero-3-phosphocholine (POPC)/Chol at room temperature. Compositional trends in order parameter (S_0) and rotational diffusion parameter ($R\perp$) extracted from simulations of ESR spectra measured at 9.5 GHz were compared for three ternary systems including bSM/DOPC/Chol, bSM/POPC/Chol, and 1,2-distearoyl-*sn*-glycero-3-phosphocholine (DSPC)/DOPC/Chol. Previous studies have established Ld+Lo phase coexistence in DSPC/DOPC/Chol [1,2] and bSM/DOPC/Chol [3–5]. A comparison of S_0 and $R\perp$ trends between DSPC/DOPC/Chol, bSM/DOPC/Chol, and bSM/POPC/Chol provides support for Ld+Lo coexistence in bSM/POPC/Chol, in agreement with Förster resonance energy transfer (FRET) results (Chapter 2) and published studies [6]. Still, some mysteries remain in the interpretation of these ESR data.

3.2 INTRODUCTION

ESR has long been used to investigate motion and order of hydrocarbon chains in the bilayer [7] and to study lateral phase separation in model membranes [8]. ESR has also provided insight into the dynamic structure of Ld, Lo, and gel (Lβ) phases

[9]. Several studies have investigated coexisting phases in detergent resistant membranes isolated from cells [10], plasma membrane vesicles prepared from cells [11], and live cells [12]. High frequency continuous wave (CW)-ESR (eg. 94 and 250 GHz) provides sensitivity to faster membrane dynamics, including internal acyl chain motions [13,14]. Multifrequency ESR exploits the sensitivities of multiple microwave frequencies to different lipid motions [15]. ESR at 9.5 GHz is sensitive to slow modes including overall lipid motion.

We focus here on using ESR at 9.5 GHz to investigate three-component model membranes. Composition-dependent ESR studies have been conducted for many years [16]. More recently, ESR has been used to verify phase coexistence regions and phase boundaries across composition space [17] and determine tielines [18] for the ternary lipid mixture 1,2-dipalmitoyl-*sn*-glycero-3-phosphocholine (DPPC) /1,2-dilauroyl-*sn*-glycero-3-phosphocholine (DPLC)/Chol. In studies of ternary systems comprising lipids of increasing biological relevance, Heberle et al. employed ESR to verify Ld+Lo phase boundaries in three DSPC-containing model systems, including DSPC/DOPC/Chol [2]. ESR has been used to investigate sphingomyelin (SM)-containing ternary systems including bSM/DOPC/Chol [5,19] and palmitoyl SM (PSM)/POPC/Chol [20,21]. These studies determined tielines in bSM/DOPC/Chol [5] and proposed phase diagrams for PSM/POPC/Chol [20,21].

ESR permits detection of heterogeneity through measurements of local order and dynamics. In these studies, we compared compositional trends in spectral parameters S_0 and $R\perp$ obtained from simulations of ESR spectra collected at 9.5 GHz. Trends are consistent both between the three ternary systems we examined, and with other studies examining these mixtures [2,19,21]. At 9.5 GHz ESR frequency, slow motions including bilayer undulations complicate a rigorous quantitative interpretation, especially for rotational diffusion. However, composition-dependent trends in the recovered parameters offer insight into lipid mixing, particularly when compared to trends in a system with well-established phase behavior such as DSPC/DOPC/Chol. We did not assign physical interpretation to actual S_0 values or relative $R\perp$ values. Instead, we found similar trends in the three lipid systems studied, consistent with Ld+Lo phase coexistence in bSM/POPC/Chol.

3.3 MATERIALS AND METHODS

3.3.1 ESR Background

In ESR, a collision-protected unpaired electron serves as the probe that is manipulated in a magnetic field. The electron response to excitation is recorded, providing information about its local environment. Although many sophisticated ESR measurements are possible, we focused here on CW-ESR at 9.5 GHz as a high-throughput method for investigating the spin probe local environment as a function of composition. The experimental methods described below were designed to utilize ESR for investigating Ld+Lo phase coexistence in bSM/POPC/Chol.

We used a spin probe called 16-doxyl-stearic acid (16-DSA) that comprises a nitroxide free radical attached to the 16-carbon position of an 18-carbon fatty acid chain (Fig 3.1). Perpendicular to the bilayer normal, the nitroxide ring includes an unpaired electron in the nitrogen *p*-orbital parallel to the bilayer normal. Being near the end of the hydrocarbon chain, this spin probe reports chain order and dynamics rather than order in the headgroup region. This probe partitions roughly equally into

Lo and Ld phases. While strong partitioning is preferred for fluorescent probes used in FRET studies, equal partitioning is preferred here because it allows us to detect appreciable ESR signals for the probe in both liquid environments.

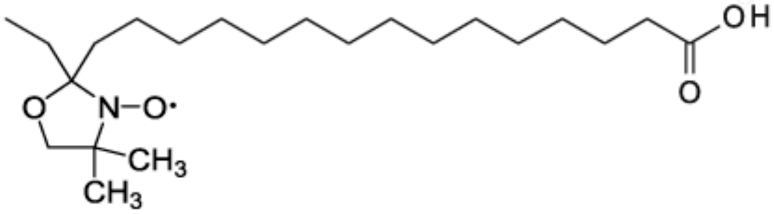

Figure 3.1 Structure of spin probe 16-DSA. The nitroxide spin label (left end) is located at the 16-carbon position of the 18-carbon fatty acid chain.

3.3.2 Materials

All sphingolipids and glycerophospholipids were purchased from Avanti Polar Lipids (Alabaster, AL) as stock solutions in chloroform (bSM, DSPC, DOPC, POPC). Lipid stock solutions were prepared in HPLC grade chloroform with concentration determined to < 1% by inorganic phosphate assay. SM stocks included 0.5% methanol by volume to prevent precipitation during humid weather. Chol was obtained from Nu Chek Prep (Elysian, MN) and prepared in chloroform with standard gravimetric methods to 0.2%. Ultrapure H2O from purification systems (EMD Millipore, Billerica, MA) was used for all aqueous sample preparations.

Purity to > 99% was confirmed using thin-layer chromatography (TLC) on washed, activated Adsorbosil TLC plates (Alltech, Deerfield, IL) developed with: chloroform/methanol/water (65/24/4) for all sphingolipids and phospholipids; hexane/ethyl ether/acetic acid (80/20/1) for 16-DSA; and petroleum ether/diethyl ether/chloroform (7/3/3) for Chol.

3.3.3 Sample Preparation

Chloroform mixtures of lipids and probes were prepared in glass culture tubes using a glass syringe (Hamilton USA, Reno, NC). Samples contained 1500 nmol lipid with 0.2 mol% 16-DSA spin probe. Rotary evaporation at 50°C was used to dry the chloroform mixture into a thin film. The sample tube was plunged into dry ice to freeze any condensed water and then placed under vacuum at room temperature for 24 hours to remove residual solvent. The dry film was hydrated with 400 uL of buffer pre-warmed to 45°C, and immediately vortexed to disperse the lipid into paucilamellar vesicles (PLVs). The buffer contained 10 mM KCl, 5 mM PIPES, and 1 mM EDTA at pH 7.0. The PLV suspension was subjected to five freeze/thaw cycles between liquid nitrogen and a 45°C water bath, sealed under argon, and placed in a water bath at 45°C. Samples were cooled to room temperature at 2°C per hour and incubated for > 24 h. Samples were pelleted and transferred to 1.5-1.8x100 mm glass capillaries for measurement. Each capillary was flame-sealed at one end and centrifuged to remove excess buffer that would otherwise reduce ESR signal.

3.3.4 Measurements

Samples were measured within three days of preparation, using a Bruker Instruments EMX spectrometer in CW mode at 9.5 GHz and ambient temperature.

Instrument settings were: 3320 G center field, 100 G sweep width, 2 mW microwave power, 1 G modulation frequency, and 1024 points resolution. For each sample, twenty scans were averaged in order to reduce noise and better resolve spectral features.

3.3.5 Data Analysis

We modeled the experimental ESR spectra to recover dynamic parameters including the order parameter S_0 and rotational diffusion coefficient $R\perp$ for the spin probe 16-DSA. We used the NLSL program, which implements the MOMD (Microscopic Order with Macroscopic Disorder) model to simulate measured spectra [22], and then uses nonlinear least-squares fitting [23] of the experimentally determined spectra to determine values for the dynamic parameters. The vesicle suspension comprises an isotropic distribution of locally ordered liquid environments for the nitroxide spin label, and is therefore well described by the MOMD model. This model assumes spectra arise from Brownian diffusion of the nitroxide spin probe in an ordered liquid. Spectra simulated using the stochastic Liouville equation were fit to our experimental spectra. These fits enabled determination of S_0 and $R\perp$ for our 16-DSA probe in the slow-motional regime (9.5 GHz).

Diffusion rates $R\perp$ and $R||$ describe nitroxide spin probe diffusion parallel and perpendicular to the bilayer normal. In the anisotropic membrane environment, probe motion is also affected by nitroxide orientation relative to the bilayer normal. The restoring potential describes the tendency for the nitroxide to orient in the bilayer. In particular, the lowest order term of the restoring potential expressed by S_0 describes preferential alignment of the nitroxide z-axis. S_0 is therefore a chain order assessed by the strength of the restoring force aligning the spin label in the magnetic field.

To fit our experimental ESR spectra, we followed Chiang et al. to obtain model parameters [17]. We chose starting parameters for samples on our high-melting lipid (high-Tm)/Chol binary identical to those used for the DSPC/Chol binary with the related spin probe 1-palmitoyl-2-(16-doxyl stearoyl) phosphatidylcholine (16-PC). We carried out the fitting procedure as described in Chiang et al. by varying six model parameters [17]. These include three pairs of closely related parameters including the first two coefficients of the restoring potential, the diffusion rates as described by the average rotational rate constant and rotational anisotropy, and two parameters describing Gaussian inhomogeneous spectral broadening. Strong correlations between these pairs suggested that fewer adjustable parameters should be used. A fixed rotational anisotropy of ten describing a ten-fold difference between $R\perp$ and $R||$ was chosen to be physically reasonable. The lower order terms for restoring potential and spectral broadening were set to zero. As a result, only three parameters were varied to obtain the best-fit simulated spectra.

3.4 RESULTS

We used ESR to further characterize heterogeneity in the Ld+Lo coexistence of bSM/DOPC/Chol and bSM/POPC/Chol at room temperature. To aid in the interpretation of observed trends, parallel samples were prepared using the mixture DSPC/DOPC/Chol, which has a well-characterized Ld+Lo region [1,2]. We prepared two compositional trajectories, shown in Fig. 3.2. Trajectory T2 crosses through the Ld+Lo region in all three systems, in the approximate direction of tielines just above the three-phase triangle of DSPC/DOPC/Chol. Based on the published phase diagram for this mixture [2], this is the longest Ld+Lo tieline. The compositions of coexisting phases along this tieline are expected to be maximally dissimilar, thereby clarifying analysis. The trajectory T1 crosses the ternary composition space above the Ld+Lo region, providing a control trajectory for which all changes in physical properties can be attributed to a gradual, continuous transition between Ld and Lo phases.

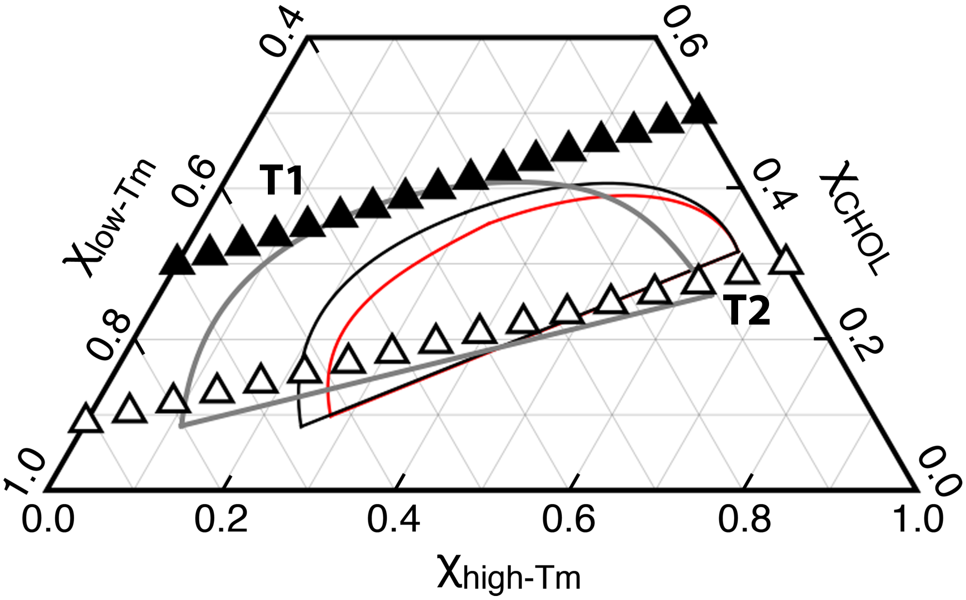

Figure 3.2 Compositional trajectories for ESR experiments. The one-phase control trajectory (T1, filled symbols) extends smoothly from Lo phase at 50% Chol on the high-Tm/Chol binary to Ld phase at 30% Chol on the low-Tm/Chol binary. The Ld+Lo trajectory (T2, open symbols) extends from 30% Chol on the high-Tm/Chol binary to 9% Chol on the low-Tm/Chol binary. Trajectory T2 crosses through the Ld+Lo coexistence region shown for DSPC/DOPC/Chol (gray), bSM/DOPC/Chol (black), and bSM/POPC/Chol (red). Trajectory T2 follows the tieline at the base of the Ld+Lo coexistence region for DSPC/DOPC/Chol.

3.4.1 Order Parameter Results

3.4.1.1 Order Parameter Trends

Figure 3.3 plots the order parameter S_0 reported by the spin probe 16-DSA *versus* composition. For each of the three mixtures, chain order increases with increasing amounts of high-Tm lipid (left-to-right on the plot), and with increasing cholesterol (T1 data, as compared to T2). Along T1 and T2, order is quantitatively similar for bSM/DOPC/Chol and DSPC/DOPC/Chol, but greater for bSM/POPC/Chol. This result is consistent with increased bilayer fluidity and decreased order in DOPC-containing mixtures, as expected due to the unsaturation in each DOPC hydrocarbon chain.

Apart from these broad trends, two distinct categories of behavior are observed. For the T2 trajectory, a sharp decrease in S_0 at high fractions of high-Tm lipid marks the formation of Ld phase and concomitant redistribution of 16-DSA between high- and low-order environments in the Ld+Lo coexistence region. The decrease coincides with the FRET peak reported by the BoDIPY/LR-DOPE probe pair in the region of enhanced efficiency for bSM/DOPC/Chol (Fig. 2.1). Since the spin probe partitions roughly equally between Ld and Lo phases, it experiences both low- and high-order environments. Consequently, the observed S_0 value is an average of S_0 values in the two phases. A decrease in S_0 is also apparent in the T2 trajectory of bSM/POPC/Chol, though the change is not as sharp as for bSM/DOPC/Chol and DSPC/DOPC/Chol. However, while the T2 trend for bSM/POPC/Chol is more consistent with the other T2 trajectories than with T1 trajectories, S_0 values are consistently intermediate between those for the DOPC-containing T2 trajectories and all T1 trajectories. Therefore, S_0 results provide at best ambiguous support for Ld+Lo coexistence in bSM/POPC/Chol.

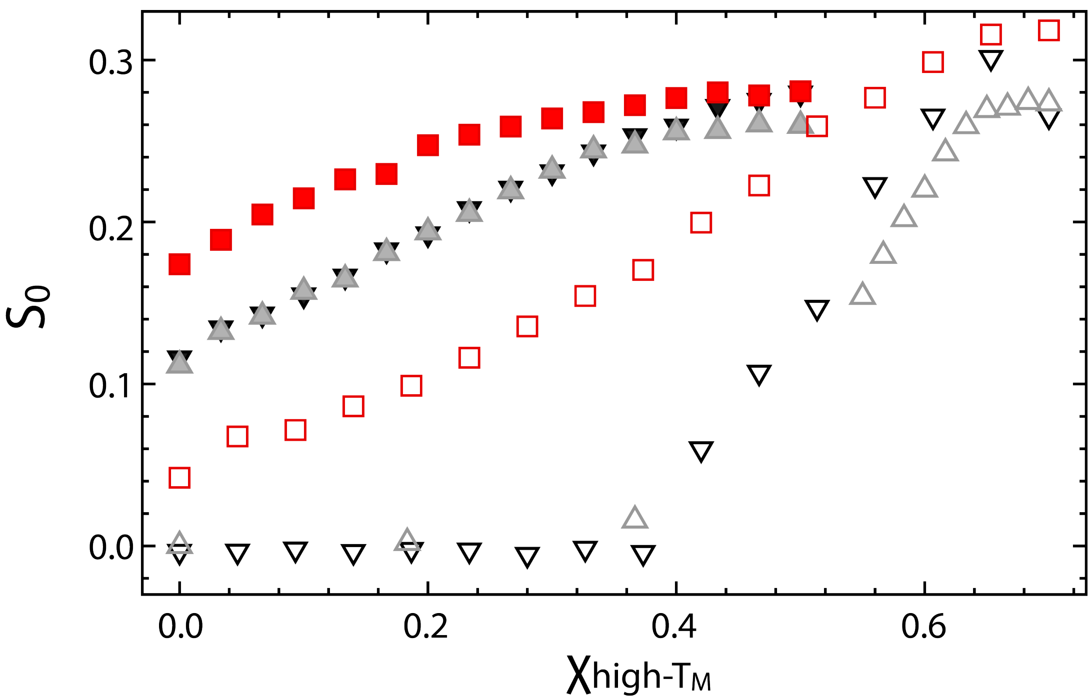

Figure 3.3 ESR order parameter ambiguously supports Ld+Lo coexistence for bSM/POPC/Chol. ESR order parameter trends vs. composition along the one-phase control trajectory (T1, filled symbols) and Ld+Lo trajectory (T2, open symbols) for DSPC/DOPC/Chol (gray up triangles), bSM/DOPC/Chol (black down triangles), and bSM/POPC/Chol (red squares). Similar order parameter (S_0) trends for DSPC/DOPC/Chol and bSM/DOPC/Chol confirm Ld+Lo coexistence in these systems. Trends in bSM/POPC/Chol through the expected Ld+Lo coexistence region (open red squares) are intermediate between known phase coexistence (open symbols) and one-phase compositions (filled symbols).

3.4.1.2 Endpoint Order Parameter Values

Considering S_0 values at the trajectory endpoints, order depends more on composition in Ld than Lo phase. We report similar S_0 values in all three ternary systems for both T1 and T2 trajectory compositions near the high-Tm/Chol binary where little low-Tm lipid is present. We conclude that near the bilayer center, bSM and DSPC exhibit similarly ordered Lo phases at a given high-Tm/Chol ratio. Because the spin probe 16-DSA resides near the bilayer center, it only reports chain order in the hydrocarbon region.

Order changes little within Lo phase between 30% and 50% Chol near the high-Tm/Chol binary. Although the T1 trajectories for bSM/DOPC/Chol and DSPC/DOPC/Chol nearly coincide, they differ near the high-Tm/Chol binary where order is greater for bSM/DOPC/Chol. This indicates that bSM/DOPC/Chol Lo phase accommodates more Chol, consistent with steeper tielines in the Ld+Lo coexistence region.

Near the low-Tm /Chol binary, low-Tm lipid properties dominate since little high-Tm lipid is present at these compositions. For T1 and T2 compositions near this binary, Ld phase is similarly ordered for both bSM/DOPC/Chol and DSPC/DOPC/Chol but more ordered for bSM/POPC/Chol. T1 exhibits greater order for all systems near the low-Tm/Chol binary. This indicates that Ld phase on the low-Tm/Chol binary becomes significantly more ordered as Chol is added. Indeed, adding Chol to Ld phase increases chain order by forcing unsaturated lipid chains into smaller cross-sectional area, effectively using the lipid headgroup to shield the large hydrophobic cross-section of Chol from water [24].

3.4.2 Rotational Diffusion

Spin probe rotational diffusion perpendicular to the acyl chains ($R\perp$) is shown in Fig. 3.4. As for S_0, $R\perp$ decreases sharply from its Lo value on the high-Tm/Chol binary upon formation of Ld phase (along the T2 trajectory). However, $R\perp$ eventually increases and reaches a similar or slightly larger final value in pure Ld phase along the low-Tm/Chol binary. The initial decrease in $R\perp$ does not correspond to simple physical behavior: since diffusion is faster in Ld phase, we expect that crossing from Lo into the Ld+Lo coexistence region should result in an increase in $R\perp$. This issue highlights the limitations of the MOMD model for analyzing ESR spectra at 9.5 GHz, as discussed further in Section 3.5.

Nevertheless, the trends in $R\perp$ for the two compositional trajectories in the three ternary systems may be compared. In particular, the trends in $R\perp$ for DSPC/DOPC/Chol show distinct regimes corresponding to phase-coexistence regions, and we therefore proceed in our comparison of these trends for the other mixtures. In particular, $R\perp$ for the T2 trajectory of bSM/POPC/Chol is strikingly similar to that of the other T2 trajectories. Since the T2 trajectories of bSM/DOPC/Chol and DSPC/DOPC/Chol cross a well-established Ld+Lo phase coexistence region, this result suggests heterogeneity in bSM/POPC/Chol.

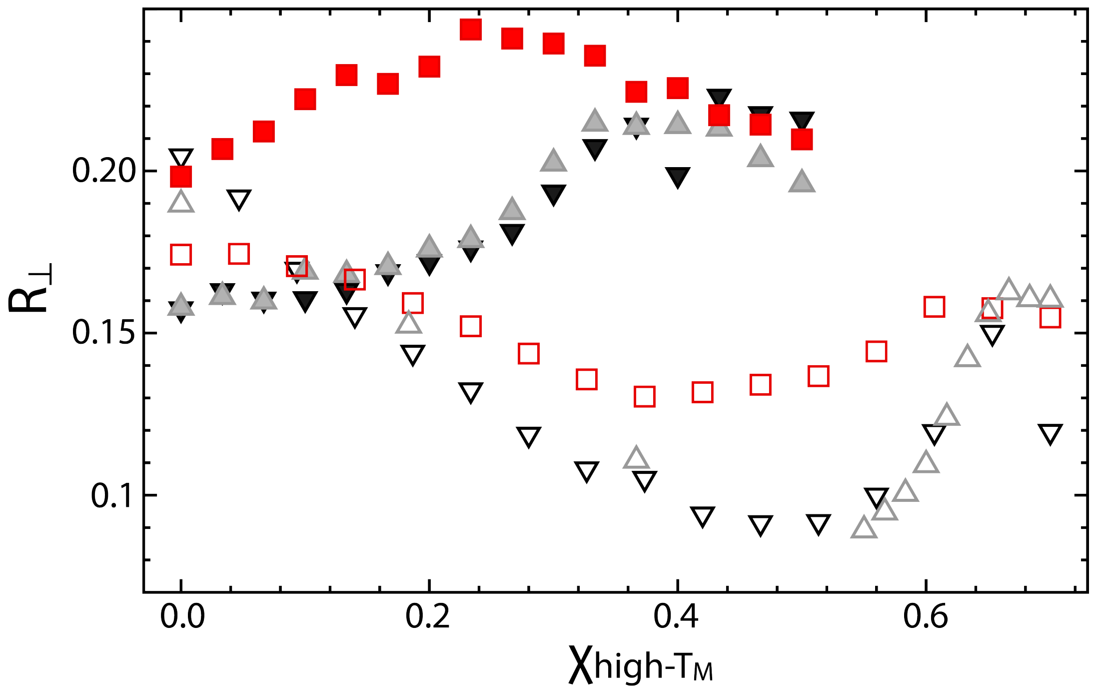

Figure 3.4 ESR rotational diffusion parameter is consistent with Ld+Lo coexistence for bSM/POPC/Chol. ESR rotational diffusion rate trends vs. composition along the one-phase control trajectory (T1, filled symbols) and Ld+Lo trajectory (T2, open symbols) for DSPC/DOPC/Chol (gray up triangles), bSM/DOPC/Chol (black down triangles), and bSM/POPC/Chol (red squares). Similar rotational diffusion rate *R⊥* (10^9 s^{-1}) trends for all three systems are consistent with Ld+Lo heterogeneity in bSM/POPC/Chol (red open squares).

3.4.3 Phase Diagram Features

It is possible to distinguish abrupt changes in the compositional trends of S_0 and $R\perp$ that are consistent with features on the DSPC/DOPC/Chol, bSM/DOPC/Chol, bSM/POPC/Chol phase diagrams (Fig. 3.2). Along the T2 trajectory, both S_0 and $R\perp$ exhibit a distinct break point at high fractions of the high-Tm lipid, consistent with the boundary between the Ld+Lo and Lo regions. For DSPC/DOPC/Chol and bSM/DOPC/Chol, this break occurs at $\chi_{\text{high-Tm}}$~0.65. For bSM/POPC/Chol the break is less distinct in S_0 but occurs at χ_{bSM}~0.60 for $R\perp$. Along the T1 trajectory, $R\perp$ drops near the critical point at χ_{bSM}~0.38 for all three mixtures.

3.5 DISCUSSION

This section compares the results presented above to published studies, discusses limitations of these ESR studies, and proposes future experiments.

3.5.1 Comparison with Published Studies

We compare our 16-DSA results for each of the ternary mixtures with previous studies conducted in these mixtures with 9.5 GHz ESR. Heberle et al. employed the spin probe 16-PC and used the MOMD model to perform one-component fits on spectra for DSPC/DOPC/Chol compositions exhibiting Ld+Lo phase coexistence [2]. Smith et al. use 16-PC and the MOMD model to perform one-component fits on spectra for bSM/DOPC/Chol compositions along the Ld+Lo phase boundary [19]. Livshits et al. and Ionova et al. interpreted compositional trends in features of measured absorption spectra to construct ternary phase diagrams for PSM/POPC/Chol [20,21].

3.5.1.1 DSPC/DOPC/Chol

We compare our 16-DSA results for DSPC/DOPC/Chol with those Heberle et al. obtained for 16-PC ([2], Fig. 4A). Here, the same compositional trajectory through the Ld+Lo region was examined, and spectra for samples exhibiting Ld+Lo coexisting phases were fit with one component to determine the average S_0 value. In both cases, a sharp drop in S_0 accompanies Ld phase formation and marks the phase boundary between the Ld+Lo coexistence region and the one-phase Lo region. Our results for DSPC/DOPC/Chol along the tieline trajectory T2 are in agreement with those obtained by Heberle et al., confirming that compositional trends of both S_0 and $R\perp$ for 16-DSA and 16-PC may be compared.

3.5.1.2 bSM/DOPC/Chol

We compare our bSM/DOPC/Chol results for trajectory T1 to those Smith et al. obtained for spectra along the upper boundary of the Ld+Lo region, from Lo phase at bSM/DOPC/Chol = 0.44/0.46/0.10 to Ld phase at 0.15/0.63/0.22 along a roughly linear compositional trajectory ([19], Samples 1-9, Figs. 3 and 5). Our T2 trajectory results are compared to spectra obtained on the lower portion of the Ld+Lo region from Lo phase at 0.62/0.04/0.32 to Ld phase at 0.15/0.63/0.22 ([19], Samples 19-10, Figs. 3 and 5). Compositional trends for both S_0 and R⊥ are consistent between these two studies.

Smith et al. observed nearly constant values of S_0 reported by 16-PC for compositions with high bSM and Chol concentrations [19]. They also observed nearly constant S_0 values within the Ld phase, independent of composition. These results are qualitatively consistent with our findings for bSM/DOPC/Chol, that S_0 varies little for compositions in the Lo phase as well as the Ld phase with decreasing order from high Lo phase fraction to high Ld phase fraction (Fig. 3.3).

Further comparison is made between comparable trajectories in the two studies. Along the T1 trajectory (Fig. 3.3) and Smith et al. Samples 1-9 ([19], Fig. 5), S_0 decreases gradually and continuously from Lo to Ld phase. Along the T2 trajectory and Smith et al. Samples 19-10 ([19], Fig. 5), S_0 decreases dramatically from an initially high value in Lo phase upon Ld phase formation.

Finally, Smith et al. found similar compositional trends both S_0 and $R\perp$ for 16-PC and the spin probe 1-palmitoyl-2-(14-doxyl stearoyl) phosphatidylcholine (14-PC), permitting comparison between our bSM/POPC/Chol results and those obtained by Livshits et al. Ionova et al. for spin probe 14-PC [19–21].

3.5.1.3 SM/POPC/Chol

Livshits et al. and Ionova et al. calculated spectral features directly from the first-derivative of measured absorption spectra and interpreted compositional trends in these values to construct a ternary phase diagram for PSM/POPC/Chol [20,21]. Further, Ionova et al. found results for outer hyperfine splitting to be in qualitative agreement with trends in S_0 determined by using the MOMD model to perform one-component fits on spectra for PSM/POPC/Chol containing spin probe 14-PC [21]. This permits comparison between our results obtained for S_0 in bSM/POPC/Chol and their results in PSM/POPC/Chol. As discussed in Chapter 2, differences between PSM and bSM domain sizes have been detected via small-angle neutron scattering (SANS), yet the ternary phase diagrams for both SM species with POPC and cholesterol are similar. We therefore make qualitative comparisons between compositional trends in

S_0 with these studies. Ionova et al. found an increase in S_0 ([21], Fig. S4) accompanied by small increases in rotational diffusion rate with increasing cholesterol content. This trend is consistent with our results for bSM/POPC/Chol, comparing trajectory T2 at low cholesterol and trajectory T1 at higher cholesterol fractions (Fig. 3.3).

3.5.2 ESR Limitations at 9.5 GHz

Quantitative physical interpretation of S_0 and $R\perp$ values obtained from MOMD simulations is not possible with our ESR results at 9.5 GHz [15]. We discuss three reasons. First, correlations between simulation parameters are not fully removed by reducing the number of independent parameters, despite attempts discussed in Section 3.3. Second, this model does not fully capture nitroxide probe dynamics, as indicated by systematic deviations between our experimental and simulated spectra (not shown). This discrepancy has arisen for both 16-DSA and the more commonly used 14-PC and 16-PC [2,19]. Third, we could fit spectra in the phase coexistence regime to a superposition of ordered and disordered parameters since the spin probe exists in both Lo and Ld environments.

It has been shown that the 9.5 GHz measurement frequency used here does not provide the necessary dynamic conditions for accurate physical interpretation of fitting parameters including S_0 and $R\perp$ in terms of local acyl chain motions relative to the overall bilayer [15]. Indeed, the fast local (internal) motions of the nitroxide on the acyl chain we seek to isolate and measure independently are instead averaged with slower overall bilayer motions such as undulation and tumbling. Even though the overall bilayer motions are slower, they affect the spectra because they are not slow enough to be frozen into the rigid limit at this measurement frequency. In short, spectra measured at this frequency are affected by both fast internal dynamics and slower overall bilayer motions [17].

In addition, S_0 reflects a composite of fast methylene bond rotations and slow rotation of the entire acyl chain. Further, the two components of rotational diffusion, $R\perp$ and $R||$, are coupled. Typically, $R||$ is typically fast for these acyl chains, so the fitting is insensitive to $R||$. In these simulations, we used a fixed rotational anisotropy of ten to describe a ten-fold difference between $R\perp$ and $R||$ (Section 3.3), which may not be reasonable across the compositions examined. Others have chosen to interpret results simulated with separately varied $R\perp$ and $R||$ parameters [17,19] but point out the physical limitations. Full physical interpretation of the spectra involves separate knowledge $R\perp$ and $R||$.

Smith et al. used 9.5 GHz ESR to examine order and dynamics for bSM/DOPC/Chol by comparing spectra measured with the spin probe in various positions along the acyl chain, from 5-PC to 16-PC and various other spin labels [19]. The results they obtained for $R_\perp$ with spin labels located further up the acyl chain exhibit more physically realistic trends. This is consistent with slower $R\perp$ values further up the acyl chain. The $R\perp$ values at the 16-carbon position may simply be too fast to be accessible at 9.5 GHz.

Since the T2 trajectories pass through the known Ld+Lo phase coexistence regime, spectra could be fit to two S_0 values for the Lo and Ld spectral components in this region. For a tieline trajectory, it is possible to quantify the distribution of spin probe between the two phases by modeling each spectrum as a weighted superposition of Lo and Ld spectra. We have performed these two-component fits (results not shown), but point out that the T2 compositional trajectory is a tieline for DSPC/DOPC/Chol but not bSM/DOPC/Chol or bSM/POPC/Chol. One-component fits provide reasonable results and have been employed in other studies that examine ESR spectra for compositions that do not lie along a tieline [19,21].

3.5.3 Future Directions

We propose multifrequency ESR studies, augmenting our results with studies at higher frequencies (95, 170, or 240 GHz) to separate local from overall motions [15]. At higher frequency, slow bilayer undulations are frozen out, so quantitative interpretation of S_0 and dynamic parameters is possible. These S_0 values can be compared to those measured by other methods, including time-resolved fluorescence anisotropy described below. In addition, more physically meaningful interpretations of the compositional trends in order and dynamics can be made because $R\perp$ and $R||$ can be separated.

3.6 CONCLUSIONS

ESR permits detection of heterogeneity through measurements of local order and dynamics. In these studies, we have compared compositional trends in spectral parameters S_0 and $R\perp$ obtained from MOMD simulations of ESR spectra collected at 9.5 GHz. Results are consistent along each trajectory for the three ternary systems examined, and trends are consistent with those found in other studies examining these mixtures. At 9.5 GHz ESR frequency, slow motions including bilayer undulations complicate rigorous quantitative interpretation, especially for rotational diffusion. However, composition-dependent trends in the recovered parameters offer insight into lipid mixing, particularly when compared to trends in a system with well-established phase behavior such as DSPC/DOPC/Chol. We do not assign physical interpretation to actual of S_0 values or relative $R\perp$ values. Instead, we simply note consistent trends in the three lipid systems studied, and more similarity between bSM/POPC/Chol compositional trends along T2 with other mixtures exhibiting Ld+Lo phase coexistence than mixtures exhibiting gradual changes within one phase. These results are consistent with Ld+Lo phase coexistence in bSM/POPC/Chol.

3.7 REFERENCES

[1] J. Zhao, J. Wu, F.A. Heberle, T.T. Mills, P. Klawitter, G. Huang, G. Costanza, G.W. Feigenson, Phase studies of model biomembranes: complex behavior of DSPC/DOPC/cholesterol, Biochimica Et Biophysica Acta, 1768 (2007) 2764–76.

[2] F.A. Heberle, J. Wu, S.L. Goh, R.S. Petruzielo, G.W. Feigenson, Comparison of three ternary lipid bilayer mixtures: FRET and ESR reveal nanodomains, Biophysical Journal, 99 (2010) 3309–3318.

[3] C. Dietrich, L.A. Bagatolli, Z.N. Volovyk, N.L. Thompson, M. Levi, K. Jacobson, E. Gratton, Lipid rafts reconstituted in model membranes, Biophysical Journal, 80 (2001) 1417–28.

[4] C.K. Haluska, A.P. Schröder, P. Didier, D. Heissler, G. Duportail, Y. Mély, C.M. Marques, Combining fluorescence lifetime and polarization microscopy to discriminate phase separated domains in giant unilamellar vesicles, Biophysical Journal, 95 (2008) 5737–47.

[5] A.K. Smith, J.H. Freed, The Determination of Tie-Line Fields for Coexisting Lipid Phases: an ESR Study, Journal of Physical Chemistry B, 113 (2009) 3957–3971.

[6] A. Pokorny, L.E. Yandek, A.I. Elegbede, A. Hinderliter, P.F.F. Almeida, Temperature and composition dependence of the interaction of delta-lysin with ternary mixtures of sphingomyelin/cholesterol/POPC, Biophysical Journal, 91 (2006) 2184–97.

[7] M. Edidin, Rotational and translational diffusion in membranes, Annual Review of Biophysics and Bioengineering, 3 (1974) 179–201.

[8] H.M. McConnell, Molecular motion in biological membranes, in: L.J. Berliner (Ed.), Spin Labeling: Theory and Applications, Academic Press, New York, 1976: pp. 525–561.

[9] P. Borbat, A. Costa-Filho, K. Earle, Electron Spin Resonance in Studies of Membranes and Proteins, Science, 291 (2001) 266–269.

[10] M. Ge, K.A. Field, R. Aneja, D. Holowka, B. Baird, J.H. Freed, Electron spin resonance characterization of liquid ordered phase of detergent-resistant membranes from RBL-2H3 cells, Biophysical Journal, 77 (1999) 925–33.

[11] M. Ge, A. Gidwani, H.A. Brown, D. Holowka, B. Baird, J.H. Freed, Ordered and disordered phases coexist in plasma membrane vesicles of RBL-2H3 mast cells An ESR study, Biophysical Journal, 85 (2003) 1278–88.

[12] M.J. Swamy, L. Ciani, M. Ge, A.K. Smith, D. Holowka, B. Baird, J.H. Freed, Coexisting domains in the plasma membranes of live cells characterized by spin-label ESR spectroscopy, Biophysical Journal, 90 (2006) 4452–65.

[13] J.P. Barnes, J.H. Freed, Dynamics and ordering in mixed model membranes of dimyristoylphosphatidylcholine and dimyristoylphosphatidylserine: a 250-GHz electron spin resonance study using cholestane, Biophysical Journal, 75 (1998) 2532–46.

[14] V.A. Livshits, D. Marsh, Simulation studies of high-field EPR spectra of spin-labeled lipids in membranes, Journal of Magnetic Resonance, 147 (2000) 59–67.

[15] Y. Lou, M. Ge, J.H. Freed, A Multifrequency ESR Study of the Complex Dynamics of Membranes, The Journal of Physical Chemistry B, 105 (2001) 11053–11056.

[16] Y.K. Shin, D.E. Budil, J.H. Freed, Thermodynamics and dynamics of phosphatidylcholine-cholesterol mixed model membranes in the liquid crystalline state: effects of water, Biophysical Journal, 65 (1993) 1283–94.

[17] Y.-W. Chiang, Y. Shimoyama, G.W. Feigenson, J.H. Freed, Dynamic molecular structure of DPPC-DLPC-cholesterol ternary lipid system by spin-label electron spin resonance, Biophysical Journal, 87 (2004) 2483–96.

[18] Y.-W. Chiang, J. Zhao, J. Wu, Y. Shimoyama, J.H. Freed, G.W. Feigenson, New method for determining tie-lines in coexisting membrane phases using spin-label ESR, Biochimica Et Biophysica Acta, 1668 (2005) 99–105.

[19] A.K. Smith, J.H. Freed, Dynamics and ordering of lipid spin-labels along the coexistence curve of two membrane phases: An ESR study, Chemistry and Physics of Lipids, 165 (2012) 348–361.

[20] V.A. Livshits, I. V. Demisheva, D. Marsh, Self-organization and phase structure of ternary lipid membranes: A spin label EPR study, Nanotechnologies in Russia, 5 (2010) 601–610.

[21] I. V. Ionova, V.A. Livshits, D. Marsh, Phase Diagram of Ternary Cholesterol/ Palmitoylsphingomyelin/ Palmitoyloleoyl-Phosphatidylcholine Mixtures: Spin-Label EPR Study of Lipid-Raft Formation, Biophysical Journal, 102 (2012) 1856–1865.

[22] D.J. Schneider, J.H. Freed, Spin Labeling: Theory and Application, in: J. Reuben (Ed.), Plenum, New York, 1989.

[23] D. Budil, S. Lee, S. Saxena, J.H. Freed, Nonlinear-Least-Squares Analysis of Slow-Motion EPR Spectra in One and Two Dimensions Using a Modified Levenberg–Marquardt Algorithm, Journal of Magnetic Resonance, Series A, 120 (1996) 155–189.

[24] J. Huang, G.W. Feigenson, A microscopic interaction model of maximum solubility of cholesterol in lipid bilayers, Biophysical Journal, 76 (1999) 2142–57.

Chapter 4
Measuring Nanodomain Size by use of FRET:
Experimental Methods for Testing the FP-FRET Model

4.1 ABSTRACT

The Finite Phase-separation FRET (FP-FRET) model has recently been developed by Heberle and Feigenson and tested on simulated data [1]. This model describes FRET efficiency (E) between freely-diffusing membrane probes in phase-separated bilayers that exhibit finite-sized phase domains. The model can be used to determine the sizes of coexisting domains with diameters from 2 to ~120 nm, depending on the Förster distance (R_0) of the probe pair employed. We conducted experiments designed to optimize the conditions for acquiring FP-FRET data. The experimental system was the ternary lipid mixture 1,2-distearoyl-*sn*-glycero-3-phosphocholine (DSPC)/1-palmitoyl-2-oleoyl-*sn*-glycero-3-phosphocholine (POPC)/cholesterol (Chol), which exhibits nanoscopic coexisting Ld+Lo phase domains [2,3]. We point out specific requirements and assumptions of the FP-FRET model and discuss methods currently being developed to obtain experimental data suitable for fitting with the model. Ultimately, the FP-FRET model will be used to determine the sizes of coexisting domains in DSPC/POPC/Chol and other systems exhibiting nanoscopic domains.

4.2 INTRODUCTION

Lipid mixtures including high- and low-melting lipids plus Chol exhibit complex phase behavior, including non-random mixing over a wide range of size scales. Evidence supports the presence of lateral heterogeneity (lipid rafts) in the unstimulated plasma membrane [4–6], yet the thermodynamic nature of this lipid organization is not well understood. Further, raft functionality depends on careful control of membrane domain size [7]. The thermodynamic nature of coexisting domains can be investigated by determining the dependence of domain size on both lipid composition and temperature [1]. Nevertheless, measurements of the size- and time-scales on which coexisting domains exist are challenging.

Few experimental techniques are capable of measuring the sizes of small membrane domains. These techniques include FRET [5,8], small-angle neutron scattering (SANS) [3,9,10], atomic force microscopy (AFM) [11], and super-resolution techniques [6,12]. FRET and SANS are advantageous because they can be used to investigate free-standing (*i.e.*, vesicular) bilayers without the strong interactions often induced by rigid bilayer support [13,14]. When measuring the sizes of nanodomains, small perturbations may result in significant artifacts that affect domain size.

Förster resonance energy transfer (FRET) takes place when resonance occurs between electric dipoles in an excited-state donor molecule and a ground-state acceptor molecule, resulting in donor quenching and acceptor excitation without donor photon emission. FRET efficiency (E) depends on the separation distance between donor and acceptor, making the technique useful for investigating phenomena occurring on molecular length scales [15]. Freely diffusing fluorescent lipid analogues can be employed for donor and acceptor; in this case, FRET can be used to probe the mixing behavior of lipids in a bilayer. When fluorescent probes partition between coexisting phase domains, the distribution of donor-acceptor distances changes, causing E to change as well. Quantitative descriptions of FRET for a random, planar array of fluorophores [16–18] have more recently been interpreted in the context of coexisting membrane phases [19,20], and FRET has been used as a molecular ruler for determining the sizes of phase domains [21,22]. FRET is sensitive to domain sizes in the important nanoscale regime of 2 to 20 nm, but an appropriate geometric model must be used to describe the spatial arrangement of donors and acceptors.

Several modifications to the membrane FRET models have been developed to determine sizes of small domains [1,23,24]. Brown and coworkers developed and used a model to estimate domain sizes in the Ld+Lo coexistence region for 1,2-dipalmitoyl-*sn*-glycero-3-phosphocholine (DPPC)/DOPC/Chol and DPPC/POPC/Chol [24,25]. However, this model is extremely limited, being applicable only near the tieline endpoints, and for probes that partition into opposite phases. In contrast, the FP-FRET model is valid for any tieline composition and can be used to perform a global analysis with several probe pairs that partition into the same or opposite phases [1]. Here we focus on designing experiments to conduct the first experimental tests of the FP-FRET model.

4.3 MATERIALS and METHODS

4.3.1 Materials

All glycerophospholipids were purchased from Avanti Polar Lipids (Alabaster, AL) as stock solutions in chloroform. Lipid stock solutions were prepared in HPLC grade chloroform with concentration determined to < 1% by inorganic phosphate assay. Chol was obtained from Nu Chek Prep (Elysian, MN) and prepared in chloroform with standard gravimetric methods to 0.2%. Ultrapure H_2O from purification systems (EMD Millipore, Billerica, MA) was used for all aqueous sample preparations.

The fluorescent Chol analog DHE (Ergosta-5,7,9(11),22-tetraen- 3β-ol; dehydrogerosterol) was obtained from Sigma-Aldrich (St. Louis, MO). The fluorescent lipid analogs Fast-DiO (3,3'-dilinoleyloxacarbocyanine perchlorate; DiO-C18:2) and Fast-DiI (1,1'-dilinoleyl-3,3,3',3'-tetramethylindocarbocyanine perchlorate; DiI-C18:2) were obtained from Invitrogen (Carlsbad, CA). All fluorescent probes were prepared in chloroform. Probe concentrations were determined in methanol by absorption spectroscopy using an HP 8452A spectrophotometer (Hewlett-Packard, Palo Alto, CA). Probe extinction coefficients were obtained from lot certificates of analysis: 12900 $M^{-1}cm^{-1}$ at 324 nm for DHE, 148300 $M^{-1}cm^{-1}$ at 486 nm for Fast-DiO, and 142700 $M^{-1}cm^{-1}$ at 548 nm for Fast-DiI. Purity to > 99% was confirmed using thin-layer chromatography (TLC) on washed, activated Adsorbosil TLC plates (Alltech, Deerfield, IL) developed with: chloroform/methanol/water (65/24/4) for all phospholipids; chloroform/methanol (9/1) for Fast-DiO and Fast-DiI probes; and petroleum ether/diethyl ether/chloroform (7/3/3) for DHE and Chol.

Chloroform mixtures of lipids and probes were prepared in glass culture tubes using a glass syringe (Hamilton USA, Reno, NC). Paucilamellar vesicles (PLVs) were prepared from these mixtures using rapid solvent exchange (RSE) [26]. The aqueous buffer contained 200 mM KCl, 5 mM PIPES, and 1 mM EDTA at pH 7.0. Unilamellar vesicles (ULVs) were prepared by passing the sample 11 times through a single 50 nm diameter pore size filter, using a hand-held mini extruder (Avanti Polar Lipids, Alabaster, AL).

4.3.2 Experimental Methods

We employed the experimental methodology of preparing samples at regular increments along a compositional trajectory, as described previously [27,28]. In these experiments, samples were prepared at 1.2 mol% compositional increments along a tieline. Samples contained two probes comprising a single donor/acceptor FRET pair: DHE/FastDiO or Fast-DiO/Fast-DiI. Probe concentrations (expressed as probe/lipid ratio) were 1/100 for DHE, and 1/1500 or 1/3000 for Fast-DiO and Fast-DiI. In addition to FRET samples containing both dyes, samples containing a single dye were prepared at the same compositional increments with the same dye concentrations. Samples containing only lipid (*i.e.*, no probe) were prepared at representative Ld and Lo phase compositions. Single-dye and lipid-only controls were used to correct raw FRET signals as described previously [27]. When sample replicates were measured, they were independently prepare samples at each composition.

Fluorescence spectroscopy measurements were performed with a Hitachi F-7000 spectrofluorimeter (Hitachi High Technologies America, Schaumburg, IL) equipped with a temperature-controlled cuvette holder (Quantum Northwest, Inc.). Measurements were performed at 23°C. Samples were diluted into buffer gently stirring in the cuvette for a final concentration of 32 μM (total lipid). Intensity measurements were made using 2.5 and 5 nm excitation and emission slits (respectively) and a 2.0 s integration time, at four pairs of excitation and emission wavelengths. One pair (channel) measures sensitized acceptor emission (SAE) FRET signals [29], and a second channel measures donor fluorescence (DHE or Fast-DiO) for calculating energy transfer efficiency (E). The remaining channels are necessary to correct for donor/acceptor bleedthrough and scattering of the excitation light [27]. The six channels (ex/em in nm) include DHE fluorescence (327/393), Fast-DiO SAE (327/503), Fast-DiO fluorescence (489/503), Fast-DiI SAE (489/563), Fast-DiI fluorescence (549/563), and vesicle scattering (370/360). A full measurement for each sample was acquired in ~ 1.5 min.

4.3.3 Modeling FRET

4.3.3.1 Original FRET Model

The Fung and Stryer model [18] provides a starting point for describing FRET in membranes. According to this model, the transfer efficiency E is given by

$$E = 1 - q_r \tag{4.1}$$

The donor quenching due to FRET (q_r) is given by

$$q_r = \int_0^\infty e^{-t/\tau_0} e^{-n_A S(t)} dt \tag{4.2}$$

where n_A is the concentration of energy acceptor in the membrane, a surface density given in number of acceptors per unit area. The energy transfer term $S(t)$ is given by

$$S(t) = \int_{R_e}^\infty 2\pi r \left[1 - e^{-(t/\tau_0)(R_0/r)^6}\right] dr \tag{4.3}$$

These equations reveal that donor quenching depends on the surface density of acceptors n_A, the Förster distance R_0, and the distance of closest approach between a donor and acceptor R_e. R_0 quantifies the spatial extent of the FRET interaction and depends on the particular donor and acceptor pair.

4.3.3.2 Requirements of the FP-FRET Model

To recover the sizes of ~2-20 nm lateral domains from measurements of FRET between freely diffusing membrane probes, a geometric model must be applied. The FP-FRET model has several geometric and thermodynamic requirements [1]. It is worthwhile to point these out here, because they are important to both experiment design and future experiment planning.

1. Domains are due to first-order phase separation, such that the area fraction of domains at a given composition can be determined from the phase diagram (*i.e.*, using a tieline and the lever rule) and molecular areas of the coexisting phases, which are determined from independent experiments. For the experiments described here, molecular areas were estimated from molecular dynamics (MD) simulations [30,31] and X-ray and neutron scattering data [32,33] in similar systems. The area fraction of membrane in the Lo phase (A_{Lo}) can then be calculated from the phase diagrams as [1,23]:

   $$A_{Lo} = \frac{a_{Lo}S_{Lo}}{a_{Lo}S_{Lo} + a_{Ld}(1 - S_{Lo})} \qquad 4.4$$

   where $a_{Lo}$is the molecular area (area per lipid) in the Lo phase, a_{Ld} is the area per lipid in the Ld phase, and S_{Lo} is the mole fraction of Lo phase.

2. The R_0 of the probe pair does not vary with distance between the donor and acceptor. This is an assumption that cannot be checked. However, there may also exist some variation in R_0 with composition. The compositional dependence can be determined by measuring the R_0 values for the probe pairs in the pure phases at the ends of the tieline. This measurement can be

performed several ways. First, separate donor- and acceptor-only samples maybe prepared for measuring the emission spectrum of the donor and excitation spectrum of the acceptor. From these spectra, the spectral overlap of the probe pair can be calculated. Second, an acceptor concentration series can be prepared. Finally, R_0 values may be recovered from fits to the FP-FRET model. The R_0 values for the probes employed here are 2.5 nm for DHE/Fast-DiO and 5.7 nm for Fast-DiO/Fast-DiI [28].

3. The donor and acceptor probes are randomly distributed within phase domains. Therefore, the probes must be non-interacting, and the probe distribution between phases is described by a partition coefficient. For example, the donor partition coefficient K_D depends on the fraction of total donor found in each phase and the mole fractions of those phases [34]. This partition coefficient is then:

$$K_D = \frac{S_{Lo}^{D}/S_{Lo}}{(1 - S_{Lo}^{D})/(1 - S_{Lo})} \tag{4.5}$$

where the fraction of donor in Lo phase is S_{Lo}^{D}, and the mole fraction of Lo phase is S_{Lo}. The donor partition coefficient is defined such that $K_D \in (0, \infty)$ and $K_D > 1$ indicates donor preference for the Lo phase. The acceptor partition coefficient K_A is defined similarly. Ideally, partition coefficients should be determined with independent experiments, such as single-dye fluorescence curves [29], fluorescence lifetime, quenching [34], anisotropy, or quantum yield [35,36]. Partition coefficients may also be recovered in the FP-FRET model. When probe self-quenching occurs, the assumption of non-interacting probes is not met. Self-quenching is a concentration-dependent effect that results in a nonlinear dependence of fluorescence intensity at high probe concentration. A large portion of fluorescence is lost when a small amount of phase appears and the dye preferentially partitions into this phase. Even at dilute probe concentrations, self-quenching cannot be avoided under conditions of strong probe partitioning, because the probe exhibits high concentration in the preferred phase when this phase is the extreme minority phase. The mechanisms for self-quenching vary for different probes and are influenced by the extent of nonrandom mixing of the probe within each phase and photophysical parameters of the probe, in addition to the partition coefficient [27]. Unfortunately, for the probes employed in these studies, the concentrations required to avoid self-quenching are prohibitively low [37].

4. Domains of the non-percolating phase are circular, and they are dispersed in a continuous (percolating) phase. Circular domains provide the simplest assumption for coexisting liquid phases. Near the Ld-end of the tieline, small Lo domains are dispersed in a continuous Ld matrix, while the opposite is true near the Ld end of the tieline. The percolation threshold where the connectivity switches from Lo to Ld phase is assumed to be located halfway along the tieline. Strictly speaking, the percolating phase cannot be assigned a priori for compositions that do not exhibit macroscopic phase separation. However, the percolation threshold was observed to be located at the midpoint of the tielines in related systems [2], and in the absence of other information we use this assumption here. It is important to emphasize that for nanodomains, there is no

direct evidence indicating the domain morphology or percolation threshold. There is evidence of noncircular modulated phase morphology for systems that are compositionally intermediate between those exhibiting nanoscopic and macroscopic domains [38]. In these systems, no percolation threshold was observed because Ld remained the percolating phase all along the tieline [39]. In contrast, a FRET study found Lo nanodomains with continuous Ld phase along most of the tieline in palmitoyl SM (PSM)/POPC/Chol, with a percolation threshold at ~80% Lo phase fraction [22]. It should be possible to investigate the identity of the percolating phase as a function of composition for systems exhibiting coexisting nanodomains using techniques such as AFM, single-particle tracking, or techniques which measure diffusion such as fluorescence recovery after photobleaching (FRAP) [40], fluorescence correlation spectroscopy (FCS), or stimulated emission depletion microscopy (STED) [12].

5. Domains have a constant radius *R* along the tieline. Modifications to the model can accommodate variation in domain sizes, including a distribution of sizes at a particular composition, or systematic variation in domain size along a tieline. De Almeida et al. reported Lo domains growing from < 20 to 75-100 nm with increasing Lo phase fraction along a tieline in PSM/POPC/Chol [22]. Domain size polydispersity is another issue which has been investigated [23]. Theoretical work suggests a narrow size distribution for nanoscale domains [41], and stable, monodisperse arrays of domains have been observed experimentally [42].

6. Domains do not interact, so they are randomly distributed within the percolating phase.
7. Energy transfer occurs only between donors and acceptors in the same bilayer, but not between multilayers. This assumption can be met by selecting probes that reside in the hydrocarbon rather than the interfacial region of the lipid bilayer, choosing probe pairs with relatively small R_0 values, and extruding PLVs to obtain ULVs. The requirement of small R_0 is met by the DHE/Fast-DiO probe pair but not by the Fast-DiO/Fast-DiI probe pair. We proceeded with Fast-DiO/Fast-DiI because employing probe pairs with larger R_0 values both extends the spatial sensitivity of the FP-FRET model and provides better signal-to-noise due more efficient energy transfer.
8. The chromophore for each probe has a stable transverse location in the bilayer for each phase. This condition can be met by selecting probes that exhibit relatively stable transverse locations in the bilayer. MD simulations have found a relatively narrow distribution for the transverse location of 1,1'-dioctadecyl-3,3,3',3'-tetramethylindocarbocyanine (DiI) chromophore in fluid DPPC bilayers [43,44]. This is likely due to the delocalized positive charge in the chromophore, which tends to anchor the chromophore near the polar interface. The DiO chromophore exhibits a similar positive charge, and is therefore likely to behave similarly. Cholesterol exhibits a predictable location in bilayers comprising the saturated and monounsaturated phosphatidylcholine (PC) lipids employed here, with long axis parallel to the bilayer normal [45].

As a structural analog of Chol [46], DHE likely exhibits good transverse stability in the bilayer compositions we examined.

4.3.3.3 Treatment for Large Domains

We first describe FRET for the case of infinite phase separation because it will motivate the need for special consideration of smaller domains. The description in the following two sections follows Heberle and Feigenson [1]. The infinite phase separation condition applies when the domain radius is ~20 times R_0. In this case, the coexisting domains can be treated as though they are completely separate from the surrounding phase, such that donor quenching can be determined separately in each phase. FRET can be calculated separately for the domain phase and the surround phase and then scaled using the relative fraction of donor and acceptor in each phase. The fraction of total donor and acceptor in each phase depends on the probe partition coefficients, which can be measured independently. These fractions do not depend on absolute donor concentration: transfer efficiency is independent of absolute donor concentration when the concentration of excited state donors is low, such that donors do not compete for acceptors. However, the absolute acceptor concentration is required, as shown by Equation 4.3.

4.3.3.4 Special Treatment for Small Domains

As domains become smaller, domain perimeter increases, and a significant fraction of probes are located near the boundary between the domain and surround phases. This boundary population must be considered separately from probes located deep inside a large domain, which, within their "FRET-competent" zone, only sense the acceptor distribution from the same phase. In contrast, donors within small domains see two distinct populations of acceptors with different average spatial densities: those located in the domain, and also those in the surrounding phase. For this boundary population of donors, the local acceptor concentration depends on distance from the donor: a donor very close to the boundary sees more acceptors in the surrounding phase (on average) than a donor a bit further into the domain. This is strictly true in the case of infinite phase separation as well, but the fraction of total donors that lie close to the boundary is much smaller and can be neglected. The FP-FRET model treats the distance dependence of the local acceptor concentrations in the domain and surround phases [1].

4.4 RESULTS AND DISCUSSION

4.4.1 Trajectory Selection

We are interested in determining the sizes of coexisting Ld+Lo nanodomains along a tieline, where the compositions of the coexisting phases remain constant. Toward this end, all experiments were conducted along a tieline trajectory through the Ld+Lo coexistence region which lies directly above the three-phase region in DSPC/DOPC/Chol and DSPC/POPC/Chol, as shown in Figure 4.1 [2].

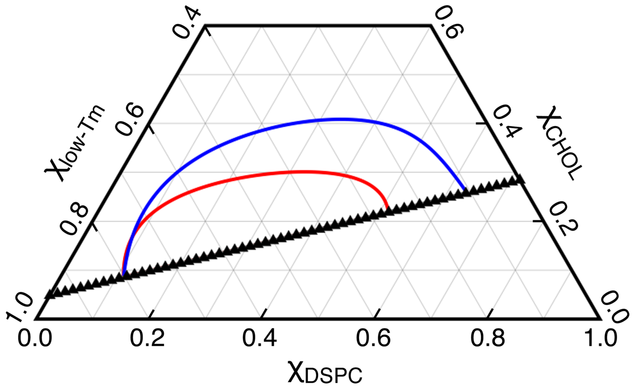

Figure 4.1 Tieline trajectory for FP-FRET experiments. Partial phase diagrams indicate the regions of Ld+Lo phase coexistence for DSPC/DOPC/Chol (blue) and DSPC/POPC/Chol (red). Compositional trajectories with 61 samples (black triangles) were prepared at 1.2 mol% compositional resolution along the tieline at the base of the Ld+Lo phase coexistence region.

4.4.2 Measured FRET Metrics

We aim to measure composition-dependent changes in FRET efficiency E. Given by Equation 4.1, E is dependent on donor quenching q_r. Also called relative donor fluorescence, donor quenching (DQ) can be determined by measuring donor fluorescence with (f_{DA}) and without (f_D) acceptor:

$$q_r = f_{DA}/f_D \qquad 4.6$$

This is one FRET metric, which we refer to as DQ. We have generally used the alternative FRET metric called sensitized acceptor emission (SAE), which requires measurement of donor-excited acceptor fluorescence, f_{SAE} [28]. Changes in E can be observed in the fluorescence of the donor or the acceptor, so the magnitude of the change in E measured for phase-separated vs. one-phase compositions should be similar for either FRET metric.

The physical basis for this linear correspondence is that for every excited donor that is quenched by the FRET mechanism, a photon is lost from the donor emission channel and gained in the acceptor emission channel. More specifically, DQ quantifies loss of donor photon emission due to nonradiative energy transfer to the acceptor, which is then detected in the acceptor emission channel via SAE.

Several distinctions between the DQ and SAE are discussed below. SAE presents several experimental advantages that are relevant in the context of experiments presented in this chapter:

1. The change in FRET efficiency is detected against different fluorescence backgrounds for the two FRET metrics. In both cases, the donor is excited at the wavelength corresponding to its absorption maximum, so donor excitation is efficient. This donor excitation wavelength is generally inefficient for acceptor excitation. DQ measures donor emission, whereas SAE measures acceptor emission. Therefore, the DQ measurement has a much larger fluorescence background than the SAE measurement.
2. Dilute probe concentrations are preferable for reducing probe self-quenching and possible probe-induced artifacts [47–50], which is important for equilibrium phase studies. However, at low probe concentrations, it can be difficult to obtain good signal-to-noise in DQ values. This occurs because the donor quenched fluorescence f_{DA} represents a small change from the donor fluorescence without acceptor f_D. In this way, DQ relies on detecting a small

change in a large signal, so the inherent noise in the measurement can be comparable to the expected change in E with composition. The result is that f_D and f_{DA} are often similar, so the ratio f_{DA}/f_D is often close to unity, and therefore E values are close to zero. This is especially true, for example, when donor and acceptor partition into the same phase, and a significant fraction of that phase is present. While f_{SAE} is often a smaller signal than f_D, no ratio is required when measuring f_{SAE}.

3. Determining E via DQ requires two samples to measure both f_D and f_{DA}, while SAE requires just a single sample at each composition.

We have measured DQ and SAE, as DQ is required for the FP-FRET model but SAE measurements have lower noise. To address the large noise in DQ measurements, we are taking two parallel approaches. First, we are investigating experimental approaches for reducing noise in measurements of DQ. Second, we are exploring the possibility of obtaining noise-reduced DQ by using an experimentally determined DQ/SAE conversion ratio. This ratio is used to calculate DQ from experimentally measured SAE (Section 4.4.4). As discussed above, there should exist a linear correspondence between SAE and DQ.

4.4.3 Enhanced and Reduced FRET Efficiency

We used FRET between fluorescent lipid analogs to examine the composition-dependent phase behavior of DSPC/DOPC/Chol and DSPC/POPC/Chol. FRET is sensitive to changes in the distribution of donor/acceptor distances that accompany phase separation [20]. When a single phase is present, probes are distributed essentially randomly in the plane of the bilayer, and FRET efficiency does not vary appreciably with composition. Relative to this baseline behavior, FRET efficiency changes dramatically in regions of phase coexistence, depending on the relative partitioning behavior of the probes. FRET efficiency is enhanced in composition regions where both probes prefer the same phase, and reduced where probes prefer different phases. Compositional regions exhibiting these two classes of behavior are termed “regions of enhanced or reduced efficiency” (REE and RRE, respectively) [29].

Figure 4.2 shows the influence of probe partitioning on observed FRET along a tieline calculated using the SAE FRET metric

$$f_{SAE}(S_{Lo}, K_D, K_A) = \frac{f_{Ld} + S_{Lo}[f_{Lo}K_D K_A - f_{Ld}]}{[1 + (K_D - 1)S_{Lo}][1 + (K_A - 1)S_{Lo}]} \tag{4.7}$$

where f_{Ld} and f_{Lo} are the f_{SAE} values in the pure Ld and Lo phases at the tieline endpoints, both set to unity for the plots in Fig. 4.2. The influence of probe partitioning on observed f_{SAE} is shown for various K_A values with $K_D = 0.33$ (donor preferring Ld phase).

An REE is observed when the acceptor also prefers the Ld phase (K_A <1). FRET increases abruptly at the phase boundary (S_{Lo} =1.0) when the preferred Ld phase first appears. The peak is located on the right-hand side of the tieline because the probes both partition strongly into Ld phase and are therefore highly concentrated (with a concomitant small average separation distance) at compositions with little Ld phase. In contrast, an RRE is observed when the acceptor prefers the Lo phase (K_A >1). FRET decreases abruptly at each phase boundary and is reduced at all compositions along the tieline. For both REE and RRE, the magnitude of FRET is greater for stronger probe partitioning ($K_A \ll 1$ or $K_A \gg 1$).

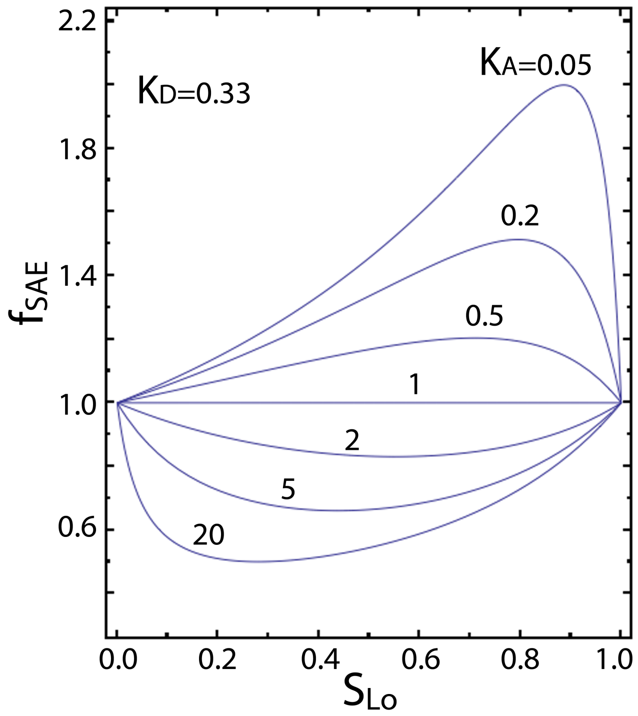

Figure 4.2 Compositional FRET trends depend on probe partitioning. SAE FRET metric plotted as a function of the Lo phase fraction (S_{Lo}) in the Ld+Lo coexistence region. The donor partitions into the Ld phase ($K_D = 0.33$). Curves for various acceptor partition coefficient (K_A) values are shown. Enhanced FRET (REE) is observed when probes colocalize (K_A <1), and reduced FRET (RRE) is observed when probes separate (K_A >1) in the Ld+Lo coexistence region. The magnitude of FRET is greater for stronger probe partitioning.

We used two Ld-preferring probes, Fast-DiO and Fast-DiI, which exhibit REE behavior in coexistence regions containing Ld phase. In separate experiments, samples contained Fast-DiO with the fluorescent cholesterol analog DHE, which modestly favors ordered phases. Together, DHE and Fast-DiO form an RRE pair. To measure DQ, two sets of samples were prepared at the same compositions: FRET samples contained donor and acceptor, and single-dye samples contained donor only. In DHE/Fast-DiO FRET experiments, the single-dye samples contained DHE. In Fast-DiO/Fast-DiI FRET experiments, the single-dye samples contained Fast-DiO. The FRET samples were also used to measure sensitized acceptor emission (SAE).

4.4.4 Determining Optimal Probe Concentrations for Domain Size Experiments

Our first studies were aimed at determining the optimal probe concentrations for FP-FRET experiments. We measured both FRET metrics DQ and SAE along the tieline (Fig. 4.1) in DSPC/POPC/Chol using the probe pair Fast-DiO/Fast-DiI with probe/lipid ratio 1/3000. In this discussion, we make the distinction between SAE measured directly, E determined from measurements of DQ (termed E_{DQ}), and E calculated from comparing SAE and E_{DQ} measurements (termed E_{SAE}). In this initial set of experiments, we anticipated that three factors would limit our signal-to-noise ratio, especially for compositions with significant fractions of Ld phase: dilute probe concentrations; the requirement of measuring E; and the preference to measure extruded samples.

Anticipating these issues, we prepared four replicates at each composition, removed outliers, averaged the remaining replicates, and calculated error bars as the standard deviation of the averaged replicates. Results are shown in Fig. 4.3. A region of enhanced efficiency (REE) is detected when Ld-preferring probes Fast-DiO and Fast-DiI co-localize in the minority Ld phase. Strong partitioning of both probes into Ld phase results in FRET increasing abruptly at the phase boundary ($S_{Lo}=1.0$, $\chi_{DSPC}\sim0.55$) when the preferred Ld phase first appears (as shown in Fig. 4.2 for curves with $K_A \ll 1$). SAE values are only slightly noisier for extruded vs. non-extruded samples. However, DQ is noisy in both cases and unphysically negative for many extruded samples with significant fractions of Ld phase (where transfer efficiencies are low). We note also that error bars are larger where the signal is changing most rapidly, which occurs when Ld is the minority phase. For future experiments, we decided to increase the number of replicates at these compositions.

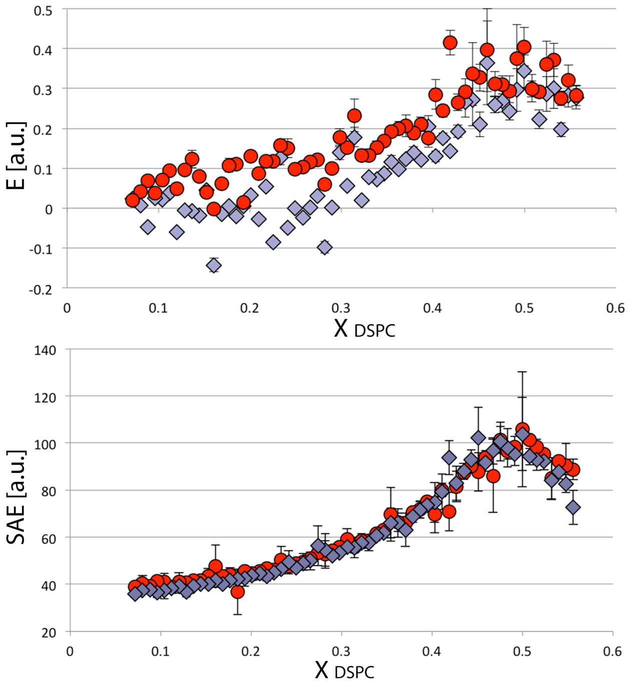

Figure 4.3 Experimental E values determined from DQ measurements can be negative for extruded samples. E_{DQ} *(top)* and SAE *(bottom)* were measured along the DSPC/POPC/Chol tieline using the probe pair Fast-DiO/Fast-DiI with probe/lipid ratio 1/3000. Data for both extruded (purple) and non-extruded (red) samples is shown. Error bars were calculated as the standard deviation of four replicates at each composition. SAE values are only slightly noisier for extruded vs. non-extruded samples.

Given the negative E_{DQ} values measured at some compositions, the acceptor concentration was increased from 1/3000 (probe/lipid ratio) to 1/1500 for the next experiments to increase the baseline transfer efficiency. In these experiments, three replicates were prepared for Ld-rich samples, and four replicates were prepared for Lo-rich samples, based on the error bars determined for the previous experiment (Fig. 4.3). Experimental E_{DQ} values were non-negative at all compositions, but the results were still noisy (Fig 4.4, bottom, white) despite the increase in probe concentration.

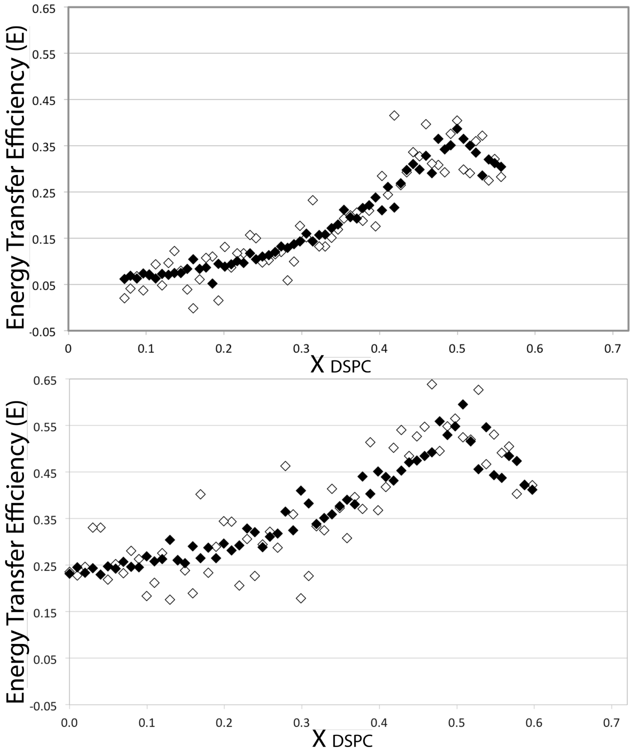

Figure 4.4 Noise-reduced E_{SAE} can be calculated from measured SAE. E determined from measured FRET metrics DQ (E_{DQ}, white) and SAE (E_{SAE}, black) along the DSPC/POPC/Chol tieline using the probe pair Fast-DiO/Fast-DiI with probe/lipid ratio 1/3000 *(top)* and 1/1500 *(bottom)* for non-extruded samples. Plots of experimental E_{DQ} values vs. experimental SAE values (Fig. 4.5) were used to calculate noise-reduced E_{SAE} values that exhibit significantly less noise than experimental E_{DQ} values.

We then explored whether E could be calculated from the measured SAE, given that SAE exhibits much less noise than experimental E values determined from measured DQ. We plotted E_{DQ} values vs. the corresponding normalized SAE values for both probe concentrations 1/3000 and 1/1500 (Fig. 4.5). As expected the relationship between E_{DQ} and SAE is linear. However, the y-intercept is not zero:

indeed, the y-intercept is -0.127 for the probe concentration 1/3000 and much closer to zero (-0.0128) for the probe concentration 1/1500. This means that at zero E, a positive reading is still detected in the SAE measurement at the lower probe concentration. This indicates that there is some background being detected in the SAE channel that is not being accounted for in the corrections described above. We will investigate whether this nonzero background can be reduced, but it certainly varies with the probe pair and probe concentrations employed. Subsequent experiments described in Section 4.4.5 yielded a positive y-intercept of 0.018 for probe concentration 1/1500 when four sample replicates were prepared at each composition.

Nevertheless, E_{SAE} (Fig. 4.4, black) exhibits significantly less noise than E_{DQ} (Fig. 4.4, white), as expected. This method of using experimentally measured SAE to obtain noise-reduced E_{SAE} is worth further consideration. The best way to obtain E_{SAE} may be to measure E_{DQ} and SAE for each experiment, instead of using a previously determined relationship between E_{DQ} and SAE to calculate E_{SAE}.

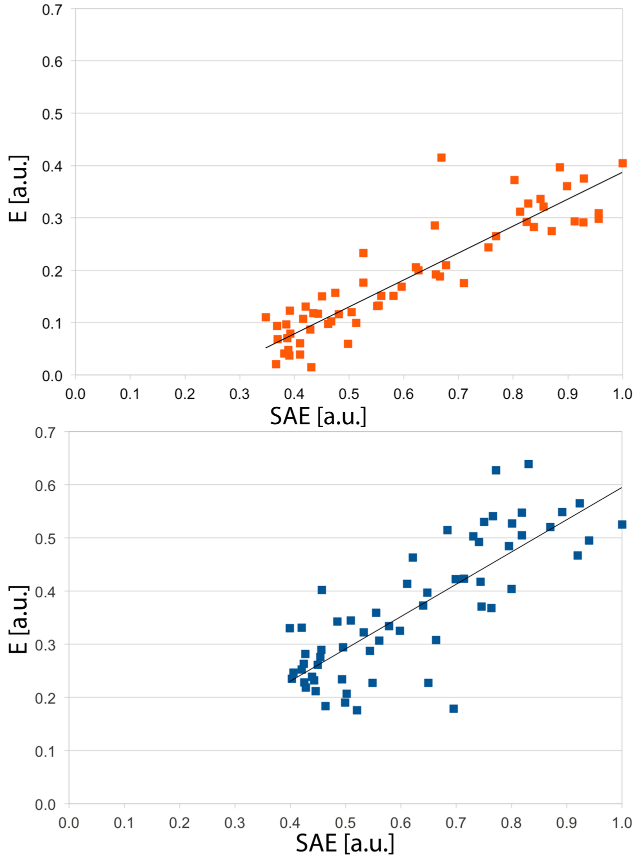

Figure 4.5 Plots of experimental E vs. SAE values reveal a linear relationship between these FRET metrics. The relationship between E_{DQ} (E determined from DQ) and normalized SAE measured along the DSPC/POPC/Chol tieline using the probe pair Fast-DiO/Fast-DiI is linear for probe/lipid ratio 1/3000 *(top)* and 1/1500 *(bottom)* for non-extruded samples.

An alternative approach would be to explore experimental approaches for reducing noise in measurements of E_{DQ}. This approach is attractive because efforts to reduce noise in measurements of single-dye fluorescence intensity used for determining probe partition coefficients are already underway [37].

4.4.5 Exploring Global Analysis and Extremes of Experimental Conditions

In order to ensure that the methods we develop for preparing experimental FP-FRET data for analysis with the FP-FRET model are broadly applicable for the range of probe pairs and experimental conditions we anticipate exploring, we undertook additional experiments in DSPC/POPC/Chol in parallel with DSPC/DOPC/Chol. The latter system exhibits coexisting macroscopic Ld+Lo phases and serves as a good control, since domains in DSPC/DOPC/Chol are known to be describable within the regime of the infinite-phase limit FP-FRET sensitivity. In addition to larger domain sizes, partition coefficients for our Ld-preferring probes are greater for DSPC/DOPC/Chol, resulting in SAE and E_{DQ} signals of greater magnitude. If the methods that we pursue do not significantly improve signal-to-noise without distorting essential curve features for DSPC/DOPC/Chol, the methods will not be useful for DSPC/POPC/Chol.

We plan to perform a global analysis with multiple probe pairs that exhibit different partitioning behavior. Results for fitting simulated FRET data to the FP-FRET model have indicated that the accuracy of recovered domain sizes and probe partition coefficients is improved and the range of spatial sensitivity is extended when global analysis is performed [1]. This is true because both increasing domain size and probe partitioning strength have the same qualitative effect of increasing the REE and RRE FRET magnitude, so these parameters will exhibit strong correlations that can be separated with additional data that enable distinction of subtle differences in parameter effects.

Since we have measured REE FRET between probes that partition into the same phase, we next chose a probe pair that exhibits partitioning into different phases to produce an RRE. In this case, FRET decreases abruptly at each phase boundary and is reduced at all phase-separated compositions along the tieline ($0.1 < \chi_{DSPC} < 0.65$). This is shown in Fig. 4.2 for $K_A > 1$. We chose the probe pair DHE/Fast-DiO because it shares the Fast-DiO probe with the Fast-DiO/Fast-DiI studies described above in Section 4.4.4. Since each probe partition coefficient is an additional fitting parameter in the FP-FRET model, using Fast-DiO as both acceptor in one experiment and donor in the other eliminates one fitting parameter.

We measured E_{DQ} and SAE along the tieline trajectory for DSPC/DOPC/Chol and DSPC/POPC/Chol using the probe pairs DHE/Fast-DiO and Fast-DiO/Fast-DiI. Probe/lipid ratios were 1/100 for DHE and 1/1500 for Fast-DiO and Fast-DiI. Two-three replicates were measured per composition for DSPC/DOPC/Chol, and four replicates were measured per composition for DSPC/POPC/Chol. Each error bar was calculated as the standard deviation in the value averaged from replicates.

Figure 4.6 compares SAE for Fast-DiO/Fast-DiI in DSPC/DOPC/Chol (blue) and DSPC/POPC/Chol (red). As reported in Section 4.4.4, a region of enhanced efficiency (REE) is detected when Ld-preferring probes Fast-DiO and Fast-DiI co-localize in the minority Ld phase. Strong partitioning of both probes into Ld phase results in FRET increasing abruptly at the phase boundary ($S_{Lo} = 1.0, \chi_{DSPC} \sim 0.70$) when the preferred Ld phase first appears (as shown in Fig. 4.2 for curves with $K_A \ll 1$). Additional replicates reduced noise for DSPC/POPC/Chol.

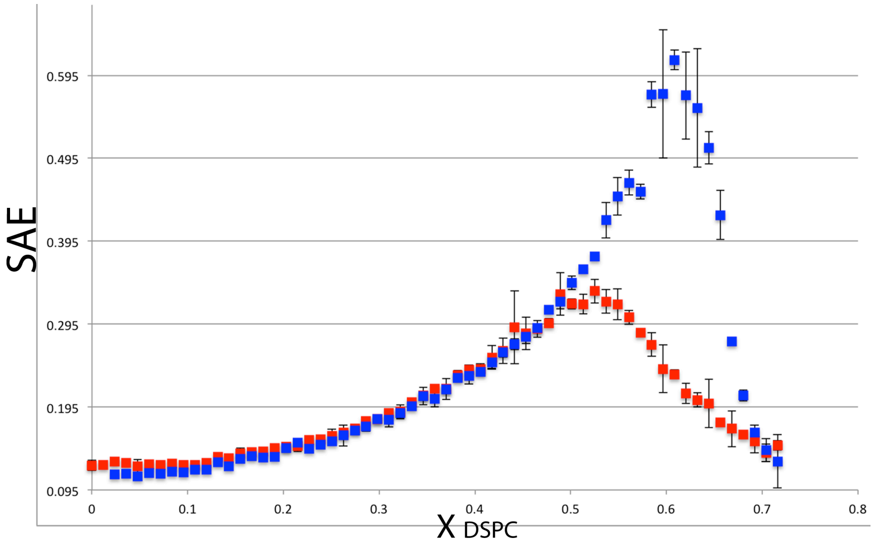

Figure 4.6 REE is detected for DSPC/DOPC/Chol and DSPC/POPC/Chol via SAE with Fast-DiO/Fast-DiI. Weaker probe partitioning and/or smaller phase domains reduced the magnitude of the REE peak for DSPC/POPC/Chol (red) compared to DSPC/DOPC/Chol (blue). Additional replicates reduced noised for DSPC/POPC/Chol compared to DSPC/DOPC/Chol.

Figure 4.7 compares SAE for DHE/Fast-DiO in DSPC/DOPC/Chol (blue) and DSPC/POPC/Chol (red). A region of reduced efficiency (RRE) is detected when Lo-preferring probe DHE separates from Ld-preferring probe Fast-DiI. Despite additional replicates, noise is greater for DSPC/POPC/Chol than DSPC/DOPC/Chol.

The magnitude of both enhanced and reduced SAE is greater for DSPC/DOPC/Chol than DSPC/POPC/Chol due to larger phase domains and greater partitioning of Fast-DiO and Fast-DiI into the DOPC-rich Ld phase. The reduced signal for DHE/Fast-DiO SAE in DSPC/POPC/Chol is cause for concern. The small R_0 for DHE results in less energy transfer for a given acceptor concentration. In addition, the relatively low DHE extinction coefficient results in less donor fluorescence.

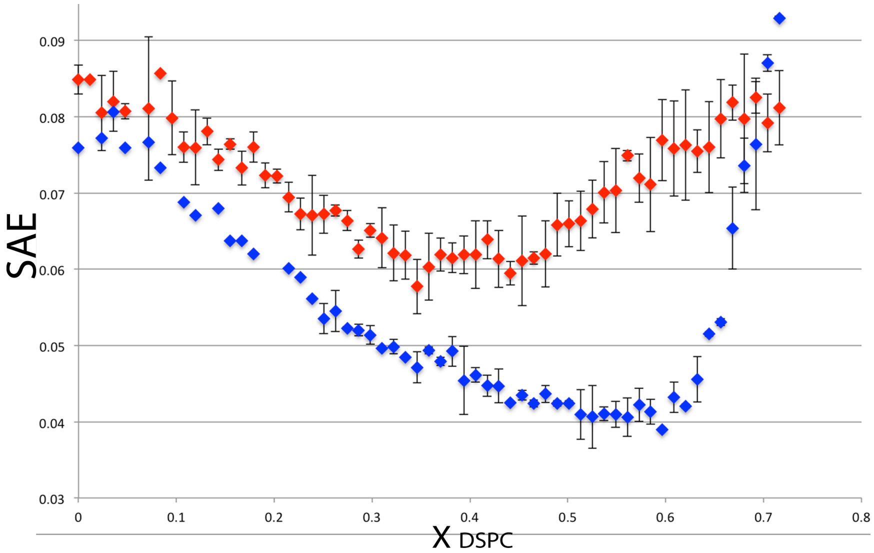

Figure 4.7 RRE is detected for DSPC/DOPC/Chol and DSPC/POPC/Chol via SAE with DHE/Fast-DiO. Weaker Fast-DiO partitioning and/or smaller domains reduced the magnitude of the RRE for DSPC/POPC/Chol (red) compared to DSPC/DOPC/Chol (blue). Despite additional replicates, noise is greater for DSPC/POPC/Chol than DSPC/DOPC/Chol.

Figure 4.8 plots E_{DQ} for DSPC/DOPC/Chol (blue) and DSPC/POPC/Chol (red) with DHE/Fast-DiO. The signal is low and error bars are large such that there is very little distinguishable trend in E_{DQ} with composition. Error bars are calculated from the standard deviation of four f_D and four f_{DA} independently prepared replicates at each composition. The average E_{DQ} value for DSPC/DOPC/Chol is negative, and the average error is larger for DSPC/POPC/Chol than DSPC/DOPC/Chol (0.14 vs. 0.06).

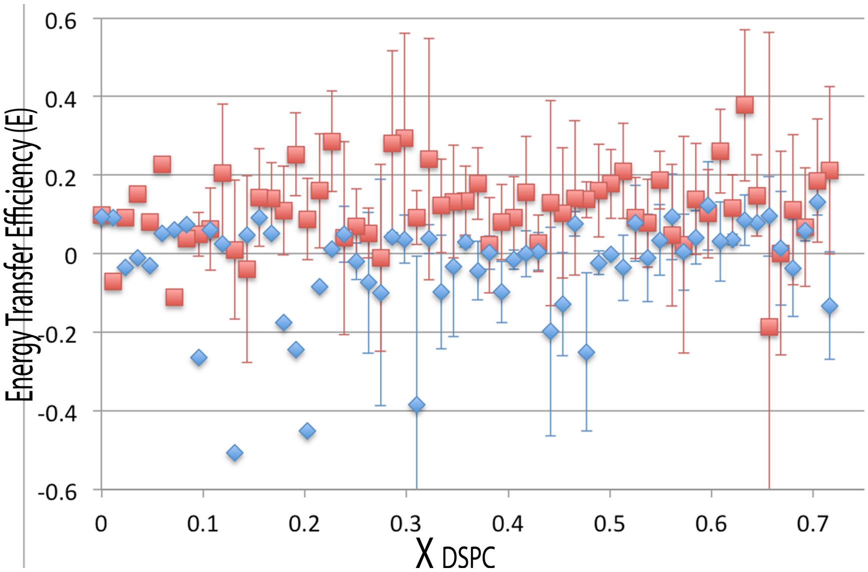

Figure 4.8 No RRE is detected via E_{DQ} with DHE/Fast-DiO. Very little distinguishable trend in E_{DQ} with composition can be observed for DSPC/DOPC/Chol (blue) or DSPC/POPC/Chol (red) due to low E_{DQ} signal. Together with the SAE results (Fig. 4.7), these results suggest that efforts to determine E_{SAE} from measured SAE should be pursued.

Since we expect the E_{DQ} to vary smoothly with composition within the phase coexistence region and follow trends similar to those observed for SAE (Fig. 4.7), we could explore whether improvements to measured E_{DQ} can be obtained through noise reduction efforts and/or measurements with additional replicates. However, the huge error bars on these results suggest that efforts to reduce noise in measurements of E_{DQ} are not likely to produce E values for DHE/Fast-DiO that can be fit with the FP-FRET model.

Approaches to determine E_{SAE} from measured SAE may be more promising. We have shown that E_{SAE} can be determined reliably from measured SAE when E_{DQ}

exhibits a discernable trend with composition (Fig. 4.4). However, additional exploration of the relationship between the SAE and DQ FRET metrics may permit recovery of E_{SAE} when experimental determination of E_{DQ} is not possible.

Further, we can take advantage of the parallel analysis we are conducting with two different probe pairs. The FP-FRET model should give similar domain sizes in both cases. Therefore, a comparison of recovered domain sizes for DHE/Fast-DiO and Fast-DiO/Fast-DiI will serve as an indication whether efforts to improve experimental determinations of E_{DQ} for DHE/FastDiO are sufficient. This line of analysis will prove more useful with additional comparisons. For example, probe pairs with other fluorescent lipid analogs that include the DiO and DiI chromophores are possible. We have conducted preliminary experiments in DSPC/POPC/Chol using the acceptor probes DiI-C18:0 (1,1'-dioctadecyl-3,3,3',3'- tetramethylindocarbocyanine perchlorate) and DiI-C18:1 (1,1'-dioleoyl-3,3,3',3'-tetramethylindocarbocyanine perchlorate) with donor FastDiO (data not shown). These probes do not partition into Ld phase as strongly as Fast-DiO and Fast-DiI [51].

Additional future directions, including comparisons with SANS measurements of domain size, are proposed in Chapter 5.

4.5 CONCLUSION

We have presented approaches for acquiring experimental FRET data to test the FP-FRET model and determine the sizes of coexisting nanoscopic domains in the Ld+Lo coexistence region for DSPC/POPC/Chol. The FP-FRET model describes energy transfer efficiency between freely diffusing membrane probes in bilayers exhibiting Ld+Lo phase separation in the form of finite-sized phase domains. Future work aims to acquire high quality data suitable for fitting to the FP-FRET model.

Several parallel approaches will be pursued to achieve high quality data. First, methods for correcting current data for probe self-quenching will be investigated. Second, connections between the E_{DQ} and SAE FRET metrics will be explored using experimental and analytical approaches. Finally, a global analysis of data acquired using multiple probe pairs, including those known to exhibit less self-quenching, will be undertaken. Once a reasonable experimental protocol has been developed and the sizes of nanoscopic domains have been measured in DSPC/POPC/Chol, we plan to examine the influence of temperature and vesicle diameter on domain size. We will extend these approaches to measure the sizes of nanoscopic domains in the more biologically relevant membrane model bSM/POPC/Chol, and compare size results to those obtained via SANS.

4.6 REFERENCES

[1] F.A. Heberle, G.W. Feigenson, Finite Phase-separation FRET: A Model for the Robust Determination of Lipid Bilayer Domain Size, In Preparation, (2012).

[2] F.A. Heberle, J. Wu, S.L. Goh, R.S. Petruzielo, G.W. Feigenson, Comparison of three ternary lipid bilayer mixtures: FRET and ESR reveal nanodomains, Biophysical Journal, 99 (2010) 3309–3318.

[3] F.A. Heberle, R.S. Petruzielo, J. Pan, P. Drazba, N. Kucerka, R.F. Standaert, G.W. Feigenson, J. Katsaras, Bilayer thickness mismatch controls raft size in model membranes, Submitted, (2012).

[4] A. Pralle, P. Keller, E.L. Florin, K. Simons, J.K. Hörber, Sphingolipid-cholesterol rafts diffuse as small entities in the plasma membrane of mammalian cells, The Journal of Cell Biology, 148 (2000) 997–1008.

[5] P. Sharma, R. Varma, R.C. Sarasij, Ira, K. Gousset, G. Krishnamoorthy, M. Rao, S. Mayor, Nanoscale organization of multiple GPI-anchored proteins in living cell membranes, Cell, 116 (2004) 577–89.

[6] S.J. Sahl, M. Leutenegger, M. Hilbert, S.W. Hell, C. Eggeling, Fast molecular tracking maps nanoscale dynamics of plasma membrane lipids, Proceedings of the National Academy of Sciences of the United States of America, 107 (2010) 6829–34.

[7] D. Lingwood, H.-J. Kaiser, I. Levental, K. Simons, Lipid rafts as functional heterogeneity in cell membranes, Biochemical Society Transactions, 37 (2009) 955–60.

[8] M. Rao, S. Mayor, Use of Forster's resonance energy transfer microscopy to study lipid rafts, Biochimica Et Biophysica Acta, 1746 (2005) 221–33.

[9] J. Pencer, T. Mills, V. Anghel, S. Krueger, R.M. Epand, J. Katsaras, Detection of submicron-sized raft-like domains in membranes by small-angle neutron scattering, The European Physical Journal E, Soft Matter, 18 (2005) 447–58.

[10] T. Masui, N. Urakami, M. Imai, Nano-meter-sized domain formation in lipid membranes observed by small angle neutron scattering, The European Physical Journal E, Soft Matter, 389 (2008) 379–389.

[11] E.I. Goksu, J.M. Vanegas, C.D. Blanchette, W.-C. Lin, M.L. Longo, AFM for structure and dynamics of biomembranes, Biochimica Et Biophysica Acta, 1788 (2009) 254–66.

[12] C. Eggeling, C. Ringemann, R. Medda, G. Schwarzmann, K. Sandhoff, S. Polyakova, V.N. Belov, B. Hein, C. von Middendorff, A. Schönle, S.W. Hell, Direct observation of the nanoscale dynamics of membrane lipids in a living cell, Nature, 457 (2009) 1159–62.

[13] F. Tokumasu, A.J. Jin, G.W. Feigenson, J.A. Dvorak, Nanoscopic lipid domain dynamics revealed by atomic force microscopy, Biophysical Journal, 84 (2003) 2609–18.

[14] M. Roark, S.E. Feller, Structure and dynamics of a fluid phase bilayer on a solid support as observed by a molecular dynamics computer simulation, Langmuir, 24 (2008) 12469–73.

[15] R.M. Clegg, The History of FRET: From conception through the labors of birth, in: C. Geddes (Ed.), Reviews in Fluorescence, Springer, New York, 2006: pp. 1–45.

[16] T.N. Estep, T.E. Thompson, Energy transfer in lipid bilayers, Biophysical Journal, 26 (1979) 195–207.

[17] P.K. Wolber, B.S. Hudson, An Analytic Solution to the Forster Energy Transfer Problem in Two Dimensions, Biophysical Journal, 28 (1979) 197–210.

[18] B.K. Fung, L. Stryer, Surface density determination in membranes by fluorescence energy transfer, Biochemistry, 17 (1978) 5241–8.

[19] J.R. Silvius, Fluorescence Energy Transfer Reveals Microdomain Formation at Physiological Temperatures in Lipid Mixtures Modeling the Outer Leaflet of the Plasma Membrane, Biophysical Journal, 85 (2003) 1034–1045.

[20] G.W. Feigenson, J.T. Buboltz, Ternary Phase Diagram of Dipalmitoyl-PC/Dilauroyl-PC/Cholesterol: Nanoscopic Domain Formation Driven by Cholesterol, Biophysical Journal, 80 (2001) 2775–2788.

[21] L.M.S. Loura, A. Fedorov, M. Prieto, Fluid–Fluid Membrane Microheterogeneity: A Fluorescence Resonance Energy Transfer Study, Biophysical Journal, 80 (2001) 776–788.

[22] R.F.M. de Almeida, L.M.S. Loura, A. Fedorov, M. Prieto, Lipid rafts have different sizes depending on membrane composition: a time-resolved fluorescence resonance energy transfer study, Journal of Molecular Biology, 346 (2005) 1109–20.

[23] K.B. Towles, A.C. Brown, S.P. Wrenn, N. Dan, Effect of membrane microheterogeneity and domain size on fluorescence resonance energy transfer, Biophysical Journal, 93 (2007) 655–67.

[24] A.C. Brown, K.B. Towles, S.P. Wrenn, Measuring raft size as a function of membrane composition in PC-based systems: Part 1-binary systems, Langmuir, 23 (2007) 11180–7.

[25] A.C. Brown, K.B. Towles, S.P. Wrenn, Measuring Raft Size as a Function of Membrane Composition in PC-Based Systems: Part II - Ternary Systems, Langmuir, 23 (2007) 11188.

[26] J.T. Buboltz, G.W. Feigenson, A novel strategy for the preparation of liposomes: rapid solvent exchange, Biochimica Et Biophysica Acta, 1417 (1999) 232–45.

[27] F.A. Heberle, J.T. Buboltz, D. Stringer, G.W. Feigenson, Fluorescence methods to detect phase boundaries in lipid bilayer mixtures, Biochimica Et Biophysica Acta, 1746 (2005) 186–192.

[28] J.T. Buboltz, C. Bwalya, S. Reyes, D. Kamburov, Stern-Volmer modeling of steady-state Forster energy transfer between dilute, freely diffusing membrane-bound fluorophores, The Journal of Chemical Physics, 127 (2007) 215101.

[29] J.T. Buboltz, Steady-state probe-partitioning fluorescence resonance energy transfer: A simple and robust tool for the study of membrane phase behavior, Physical Review E, 76 (2007) 021903.

[30] C. Hofsäss, E. Lindahl, O. Edholm, Molecular dynamics simulations of phospholipid bilayers with cholesterol, Biophysical Journal, 84 (2003) 2192–206.

[31] M. Alwarawrah, J. Dai, J. Huang, A molecular view of the cholesterol condensing effect in DOPC lipid bilayers, The Journal of Physical Chemistry B, 114 (2010) 7516–23.

[32] W.J. Sun, S. Tristram-Nagle, R.M. Suter, J.F. Nagle, Structure of gel phase saturated lecithin bilayers: temperature and chain length dependence, Biophysical Journal, 71 (1996) 885–91.

[33] N. Kucerka, S. Tristram-Nagle, J.F. Nagle, Structure of fully hydrated fluid phase lipid bilayers with monounsaturated chains, The Journal of Membrane Biology, 208 (2005) 193–202.

[34] K. Florine-Casteel, G.W. Feigenson, On the use of partition coefficients to characterize the distribution of fluorescent membrane probes between coexisting gel and fluid lipid phases: an analysis of the partition behavior of 1,6-diphenyi-l,3,5-hexatriene, Biochimica Et Biophysica Acta, 941 (1988) 102–106.

[35] W. Vaz, E. Melo, Fluorescence spectroscopic studies on phase heterogeneity in lipid bilayer membranes, Journal of Fluorescence, 11 (2001) 255.

[36] J.R. Silvius, Partitioning of membrane molecules between raft and non-raft domains: insights from model-membrane studies, Biochimica Et Biophysica Acta, 1746 (2005) 193–202.

[37] S.Y. Kim, Personal Communication: Partition Coefficients and Self-Quenching in DSPC/DOPC/POPC/Chol, (2012).

[38] T.M. Konyakhina, S.L. Goh, J. Amazon, F.A. Heberle, J. Wu, G.W. Feigenson, Control of a Nanoscopic-to-Macroscopic Transition: Modulated Phases in Four-Component DSPC/DOPC/POPC/Chol Giant Unilamellar Vesicles, Biophysical Journal, 101 (2011) L8–L10.

[39] S.L. Goh, J. Amazon, G.W. Feigenson, Towards a better raft model: Modulated phases in the 4-component bilayer DSPC/DOPC/POPC/CHOL, Submitted, (2012).

[40] W.L. Vaz, Percolation properties of two-component, two-phase phospholipid bilayers, Molecular Membrane Biology, 12 (1995) 39–43.

[41] V.A.J. Frolov, Y.A. Chizmadzhev, F.S. Cohen, J. Zimmerberg, "Entropic traps" in the kinetics of phase separation in multicomponent membranes stabilize nanodomains, Biophysical Journal, 91 (2006) 189–205.

[42] S. Rozovsky, Y. Kaizuka, J.T. Groves, Formation and spatio-temporal evolution of periodic structures in lipid bilayers, Journal of the American Chemical Society, 127 (2005) 36–7.

[43] R.R. Gullapalli, M.C. Demirel, P.J. Butler, Molecular dynamics simulations of DiI-C18(3) in a DPPC lipid bilayer, Physical Chemistry Chemical Physics, 10 (2008) 3548–60.

[44] D. Ackerman, F.A. Heberle, G.W. Feigenson, Limited Perturbation of a DPPC Bilayer by Fluorescent Lipid Probes: A Molecular Dynamics Study, In Preparation, (2012).

[45] A. Leonard, C. Escrive, M. Laguerre, E. Pebay-Peyroula, W. Neri, T. Pott, J. Katsaras, E.J. Dufourc, Location of Cholesterol in DMPC Membranes A Comparative Study by Neutron Diffraction and Molecular Mechanics Simulation, Langmuir, 17 (2001) 2019–2030.

[46] D. Wüstner, Fluorescent sterols as tools in membrane biophysics and cell biology, Chemistry and Physics of Lipids, 146 (2007) 1–25.

[47] A.G. Ayuyan, F.S. Cohen, Lipid peroxides promote large rafts: effects of excitation of probes in fluorescence microscopy and electrochemical reactions during vesicle formation, Biophysical Journal, 91 (2006) 2172–83.

[48] J. Zhao, J. Wu, H. Shao, F. Kong, N. Jain, G. Hunt, G.W. Feigenson, Phase studies of model biomembranes: macroscopic coexistence of Lalpha+Lbeta, with light-induced coexistence of Lalpha+Lo Phases, Biochimica Et Biophysica Acta, 1768 (2007) 2777–86.

[49] S.L. Veatch, S.S.W. Leung, R.E.W. Hancock, J.L. Thewalt, Fluorescent probes alter miscibility phase boundaries in ternary vesicles, Journal of Physical Chemistry B, 111 (2007) 502–4.

[50] N.F. Morales-Penningston, J. Wu, E.R. Farkas, S.L. Goh, T.M. Konyakhina, J.Y. Zheng, W.W. Webb, G.W. Feigenson, GUV Preparation and Imaging: Minimizing Artifacts, Biochimica Et Biophysica Acta, 1798 (2010) 1324–1332.

[51] T. Baumgart, G. Hunt, E.R. Farkas, W.W. Webb, G.W. Feigenson, Fluorescence probe partitioning between Lo/Ld phases in lipid membranes, Biochimica Et Biophysica Acta, 1768 (2007) 2182–2194.

Chapter 5:
Conclusions and Future Directions

5.1 CONCLUSIONS

5.1.1 Temperature-Dependent Phase Behavior in Sphingomyelin-Containing Ternary Lipid Mixtures

Using high compositional resolution FRET along with DSC, we found similar phase diagrams for the ternary mixtures bSM/DOPC/Chol and bSM/POPC/Chol at 15 and 25°C. The miscibility gap is slightly smaller in the POPC-containing system compared to the DOPC-containing system at comparable temperatures. FRET and SANS do not detect immiscibility for PSM/POPC/Chol between 35-45°C, and miscibility for PSM/DOPC/Chol between 45-55°C. The magnitude of the FRET is significantly reduced for bSM/POPC/Chol compared with bSM/DOPC/Chol, consistent with significantly smaller Ld+Lo phase domains for POPC than DOPC.

5.1.2 Ld+Lo Phase Coexistence in bSM/POPC/Chol

FRET and ESR show the presence of an Ld+Lo phase coexistence region for bSM/DOPC/Chol and bSM/POPC/Chol. Differences in ESR acyl chain order parameter were observed in the DOPC- and POPC-rich Ld phases, with greater order observed for POPC than DOPC. The more similar order in Ld and Lo phases for bSM/POPC/Chol is consistent with smaller phase domains in this system, compared to bSM/DOPC/Chol.

5.1.3 Domain Sizes in bSM/POPC/Chol

FRET results indicated Ld+Lo heterogeneity in the form of coexisting domains with sizes on the order of the 2-6 nm detection resolution of the probe pairs employed.

SANS results did not detect coexisting Ld+Lo domains in bSM/POPC/Chol above the 7 nm minimum detection limit for this technique. Together, these FRET and SANS results enabled us to constrain the sizes of coexisting Ld+Lo domains in bSM/POPC/Chol to a radius of 2-6 nm. Experimental techniques and analyses are being developed to further investigate the sizes of coexisting domains using FRET.

5.2 FUTURE DIRECTIONS

5.2.1 FRET Measurements for Sizes of Coexisting Ld+Lo Domains

To test the FP-FRET model, we will first attempt to fit the data that we currently have to recover domain sizes for DSPC/POPC/Chol [1]. The DSPC/DOPC/Chol data will serve as a good control: since domains in this system are known to be macroscopic, they will fall within the infinite-phase limit of FP-FRET sensitivity. In addition, we plan to employ a wider range of fluorescent lipid analogs in the DSPC/POPC/Chol system. Global analysis can be performed using a series of DiI probes with different partitioning behavior. Additional probes that suffer less self-quenching will also be used. Acquiring data for probe pairs with different R_0 values enhances the sensitivity and reliability of the FP-FRET model.

5.2.2 Domain Size Variation with Temperature

Temperature is also expected to affect domain sizes. Domains should get smaller approaching the upper miscibility transition temperature, which was found to be 45-55°C in bSM/DOPC/Chol and 35-45°C in bSM/POPC/Chol via FRET and SANS. Our FRET results in bSM/DOPC/Chol and bSM/POPC/Chol indicate that the tieline and phase boundaries do not shift appreciably from 15-25°C, but further high-resolution FRET studies are needed to determine phase boundaries at higher temperatures.

5.2.3 Domain Sizes in Four-Component Systems

It is possible that the mammalian PM may have raft size that is regulated by adjusting the local concentrations of certain lipids. Given the existence of macroscopic fluid phase domains in bSM/DOPC/Chol and nanoscale phase domains in bSM/POPC/Chol, a transition between these size regimes occurs in the four-component mixture bSM/DOPC/POPC/Chol. Recent work has explored this transition with fluorescence microscopy of GUV's of mixtures bSM/DOPC/POPC/Chol [2,3] and DSPC/DOPC/POPC/Chol [4,5]. If we can estimate the tielines in the four-component systems, it should be possible to recover domain sizes from FRET measurements.

In particular, by varying the low-melting lipid composition between POPC and DOPC in the mixture DSPC/DOPC/POPC/Chol, we can acquire data with different domain sizes. As the fraction of DOPC is increased, the size of coexisting Ld+Lo domains increases. Fluorescence microscopy studies have qualitatively assessed macroscopic domain sizes [4,5], and SANS studies have determined that domain sizes vary linearly within the nanodomain regime for this four-component mixture [6].

SANS is a complementary experimental technique for measuring domain sizes. Determining domain sizes in the four-component system bSM/DOPC/POPC/Chol should prove especially useful to corroborate domain size estimates in bSM/POPC/Chol, where domains are too small to be resolved with SANS. As domain sizes have been shown to decrease linearly as DOPC is replaced with POPC in the nanodomain regime of DSPC-containing mixtures via SANS [6], similar replacement studies could be used to extrapolate domain sizes in bSM/POPC/Chol from SANS measurements.

5.2.4 Domain Sizes for SM/POPC/Chol with Various SM Species

Characterization of the size transitions that occur with variation of the low-melting lipid is well underway. Less appreciated is the role of the high-melting lipid in controlling the sizes of fluid phase domains. For the same SM/POPC/Chol composition, our SANS results indicate that coexisting Ld+Lo domains are smaller for bSM than PSM, SSM, or egg SM.

We will also measure the bilayer thicknesses for the pure phase Ld and Lo compositions in these mixtures. SANS studies in the four-component system DSPC/DOPC/POPC/Chol indicate that the Ld phase thickness decreases as domain sizes grow upon replacing POPC with DOPC [6]. When comparing different SM species, greater similarity of the Ld and Lo phase thicknesses should correlate with smaller domain sizes. We therefore expect the thicknesses of the Ld and Lo phases are more similar for bSM than PSM.

Modeling data to determine the sizes of coexisting domains requires knowledge of a well-defined tieline [7] which we have now determined for bSM/POPC/Chol. Future high-resolution FRET trajectory experiments will determine phase boundaries along this tieline in SM/POPC/Chol with different SM species.

5.2.5 Vesicle Curvature Effects on Domain Sizes

Even macroscopic phase coexistence manifests as nanoscale domains on vesicles with 60-nm diameter [6]. Several techniques will provide complementary approaches for measuring domain sizes in freely suspended) bilayer vesicles. SANS measurements can be conducted on 60 and 100 nm diameter vesicles, while FRET can be measured for vesicles of these sizes in addition to larger paucilamellar vesicles. Models used to recover domain sizes from these measurements must assume domain morphologies, with round domains as the simplest case. Domain morphologies for macroscopic domains are being investigated using fluorescence microscopy of GUVs [2,3].

Combining these techniques, we can investigate how domain size varies with vesicle size and curvature [8]. This work is important to inform theoretical treatments of nanodomains. Simulation studies indicate competing roles for line tension and curvature energies in regulating domain morphology on GUVs [9], and will be extended to investigate nanoscopic domains and smaller vesicles.

5.3 REFERENCES

[1] F.A. Heberle, G.W. Feigenson, Finite Phase-separation FRET: A Model for the Robust Determination of Lipid Bilayer Domain Size, In Preparation, (2012).

[2] M.B. Kim, Personal Communication: Modulated Phase Morphologies in bSM/DOPC/POPC/Chol, (2012).

[3] S. Wickramasinghe, Personal Communication: Modulated Phase Morphologies in bSM/DOPC/POPC/Chol, (2012).

[4] T.M. Konyakhina, S.L. Goh, J. Amazon, F.A. Heberle, J. Wu, G.W. Feigenson, Control of a Nanoscopic-to-Macroscopic Transition: Modulated Phases in Four-Component DSPC/DOPC/POPC/Chol Giant Unilamellar Vesicles, Biophysical Journal, 101 (2011) L8–L10.

[5] S.L. Goh, J. Amazon, G.W. Feigenson, Towards a better raft model: Modulated phases in the 4-component bilayer DSPC/DOPC/POPC/CHOL, Submitted, (2012).

[6] F.A. Heberle, R.S. Petruzielo, J. Pan, P. Drazba, N. Kucerka, R.F. Standaert, G.W. Feigenson, J. Katsaras, Bilayer thickness mismatch controls raft size in model membranes, Submitted, (2012).

[7] F.A. Heberle, J. Wu, S.L. Goh, R.S. Petruzielo, G.W. Feigenson, Comparison of three ternary lipid bilayer mixtures: FRET and ESR reveal nanodomains, Biophysical Journal, 99 (2010) 3309–3318.

[8] J. Pencer, A. Jackson, N. Kucerka, M.-P. Nieh, J. Katsaras, The influence of curvature on membrane domains, European Biophysics Journal, 37 (2008) 665–71.

[9] J.J. Amazon, S.L. Goh, G.W. Feigenson, Competition between line tension and curvature stabilizes modulated phase patterns on the surface of giant unilamellar vesicles: A simulation study, Submitted, (2012).

Appendix A
FRET Surface Experiment Details

This Appendix accompanies Chapter 2.

A.1 Temperature Controlled FRET Measurements

Temperature control measures were taken during sample preparation and measurement to ensure equilibrium phase behavior. All samples and controls were randomized during sample preparation and measurement to reduce any systematic disparities in environment or instrument conditions that would affect measurements over time. After rapid solvent exchange (RSE), samples were placed in a water bath at 45°C (above the bSM melting temperature) and ramped at 2°C per hour to 15°C, the first measurement temperature. Samples were incubated at 15°C for three days before measurement. After measurement (which took ~ 12 h), the temperature was increased by 10°C, and samples were incubated for ~ 10 h before measurement at the new temperature. Measurement at all four temperatures was completed within four days. While different sample aliquots were used at each measurement temperature, all four aliquots came from the same culture tube in which the multilamellar vesicles (MLVs) were initially prepared.

Various measures were used to maintain a constant sample temperature at the time of measurement. The water bath holding the samples was maintained to within 1°C. Buffer used to dilute the sample in the cuvette was stored in a glass container in the water bath, and pumped directly into the cuvette. The cuvette temperature was maintained within 1°C using a Quantum Northwest temperature controller with circulating water bath. A dry block heater and Stir Kool peltier, both with home-built

PID control, were used to maintain temperatures for pipette tips and samples immediately before and after measurement. Samples were gently stirred in the cuvette throughout measurement to prevent concentration and temperature gradients. After measurement, the sample was removed from the cuvette by aspiration, and new buffer was immediately added to maintain the cuvette temperature.

FRET measured using these temperature controls is shown at 15, 25, 35°C (Fig. 2.1), and 45°C (Fig. A.1) for bSM/DOPC/Chol, and at 15, 25, and 35°C (Fig. 2.3) for bSM/POPC/Chol. Some compositional variation in FRET persisted at high temperature (Fig. A.1, Fig. 2.3), which was expected due to gradual changes in interfacial polarity and chain order that accompany changes in mixture composition. However, the large compositional variation in FRET observed at lower temperatures for bSM/DOPC/Chol is not present at 45°C (Fig. A.1), suggesting that the bilayer is well-mixed at this higher temperature. Given that the SANS results indicated a lower miscibility transition for SM/POPC/Chol compared to SM/DOPC/Chol (Fig. 2.8), the FRET surfaces for bSM/POPC/Chol at 35°C (Fig. 2.3) were presumed to exhibit complete miscibility.

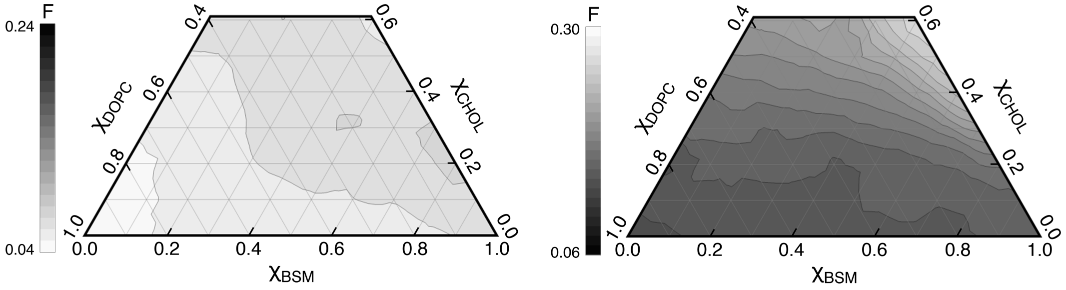

Figure A.1 FRET for bSM/DOPC/Chol at 45°C. Contour plots constructed from FRET measurements at 360 compositions, using the probe pairs BoDIPY-PC/LR-DOPE (*left*) and DHE/BoDIPY-PC (*right*). Regions of enhanced or reduced FRET efficiency that result from non-uniform probe partitioning in phase coexistence regions are not seen at 45°C, indicating nearly complete miscibility. Data were smoothed with nearest-neighbor averaging. FRET surfaces measured at 15°C, 25°C, and 35°C are shown in Fig. 2.1.

A.2 Difference FRET Surfaces

To interpret variations in FRET signal, we subtracted the bSM/DOPC/Chol 45°C surfaces (Fig. A.1) and bSM/POPC/Chol 35°C surfaces (Fig. 2.3) from the corresponding surfaces measured at 15, 25, 35°C for bSM/DOPC/Chol (Fig. 2.1) and 15 and 25°C for bSM/POPC/Chol (Fig. 2.3). The resulting difference FRET surfaces shown in Figs. A.2 and A.3 enabled us to distinguish trends in FRET due to compositional heterogeneity from those due to gradual changes that persist in well-mixed bilayers.

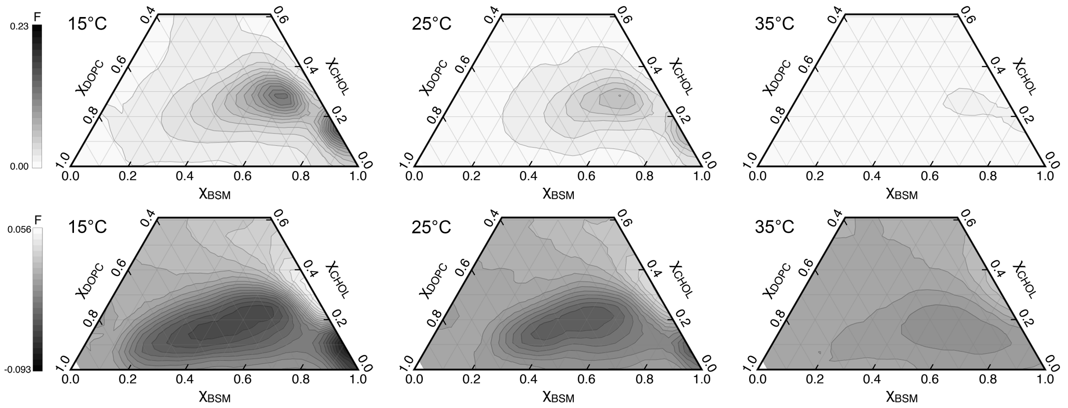

Figure A.2 Difference FRET surfaces reveal phase coexistence regions in bSM/DOPC/Chol. FRET surfaces measured at 45°C (Fig. A.1) were subtracted from FRET surfaces measured at 15°C, 25°C, and 35°C (Fig. 2.1) to obtain difference FRET surfaces shown here for the probe pairs BoDIPY-PC/LR-DOPE (upper panel) and DHE/BoDIPY-PC (lower panel) at 15°C, 25°C, and 35°C. Regions of enhanced (upper panel) or reduced (lower panel) FRET efficiency result from non-uniform probe partitioning in phase coexistence regions.

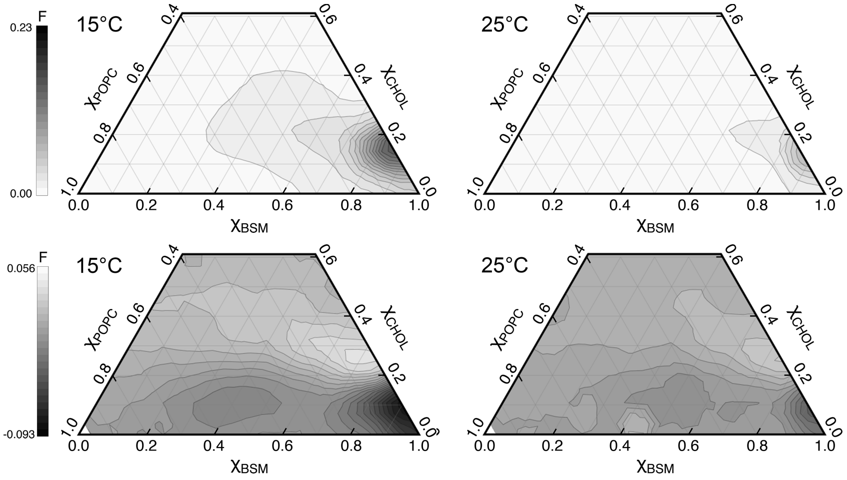

Figure A.3 Difference FRET surfaces reveal phase coexistence regions in bSM/POPC/Chol. FRET surfaces measured at 35°C (Fig. 2.3) were subtracted from FRET surfaces measured at 15°C and 25°C (Fig. 2.3) to obtain difference FRET surfaces shown here for the probe pairs BoDIPY-PC/LR-DOPE (upper panel) and DHE/BoDIPY-PC (lower panel) at 15°C and 25°C. Regions of enhanced (upper panel) or reduced (lower panel) FRET efficiency result from non-uniform probe partitioning in phase coexistence regions.

Appendix B
Differential Scanning Calorimetry Analysis and Thermograms

This Appendix accompanies Chapter 2.

B.1 DSC Data Analysis

Baseline subtraction was performed with Mathematica v7. DSC scans were acquired over a wide temperature range in order to include baseline behavior on either end. The baseline ranges were selected and fit to a second order polynomial over the temperature range of the entire scan, which was then subtracted from the raw data. Onset and completion temperatures were determined using the model-free tangent construction method [1,2]. The maximum slope at the low- and high-temperature ends of the thermogram correspond to the onset and completion temperatures, respectively. Starting from baseline-subtracted data, the first derivative of the thermogram was evaluated numerically, and smoothing was performed using a Gaussian filter to average local points. The first peak on the low-temperature end and the last valley on the high-temperature end of the first derivative plot were identified. The tangent to each of these features was constructed, and the intersection of the tangent with the baseline (*i.e.*, y=0 for baseline-subtracted data) was taken to be the onset (completion) of the transition.

Analysis was performed separately for heating and cooling scans, and results were averaged. Heating scans for samples with unreliable low-temperature baselines were omitted, even though these scans produced completion temperature values comparable to those determined from the cooling scans. For samples on which the temperatures of interest were below 0°C, results are reported for cooling scans alone.

We note that cooling to -10°C was possible during slow cooling (scan rate 0.2°C/min) because the samples became supercooled [3]. Since the lipid dispersions were in excess water, full hydration was assured due a tightly bound population of 'non-frozen water' [4].

B.2 DSC Thermograms

Thermograms for bSM/DOPC, bSM/POPC, and bSM/POPC with 10 mol% Chol are shown in Figs. B.1-B.3. The resulting phase diagrams are shown in Fig. 2.5 of the main text.

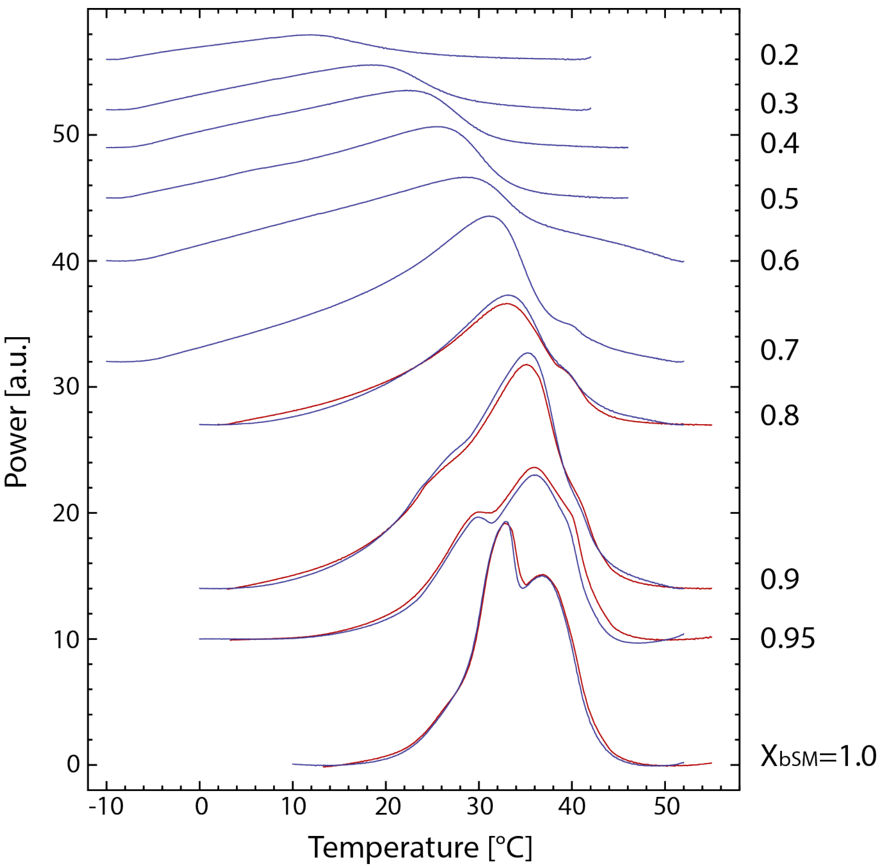

Figure B.1 DSC thermograms for bSM/DOPC. Onset and completion temperatures for each sample were determined from heating (red) and cooling (blue) scans. Scans include χ_{bSM}= 0.2, 0.3, 0.4, 0.5, 0.6, 0.7, 0.8, 0.9, 0.95, and 1.0 from top to bottom, offset for better viewing. These thermograms were used to construct the phase diagram shown in Fig. 2.5 (triangles).

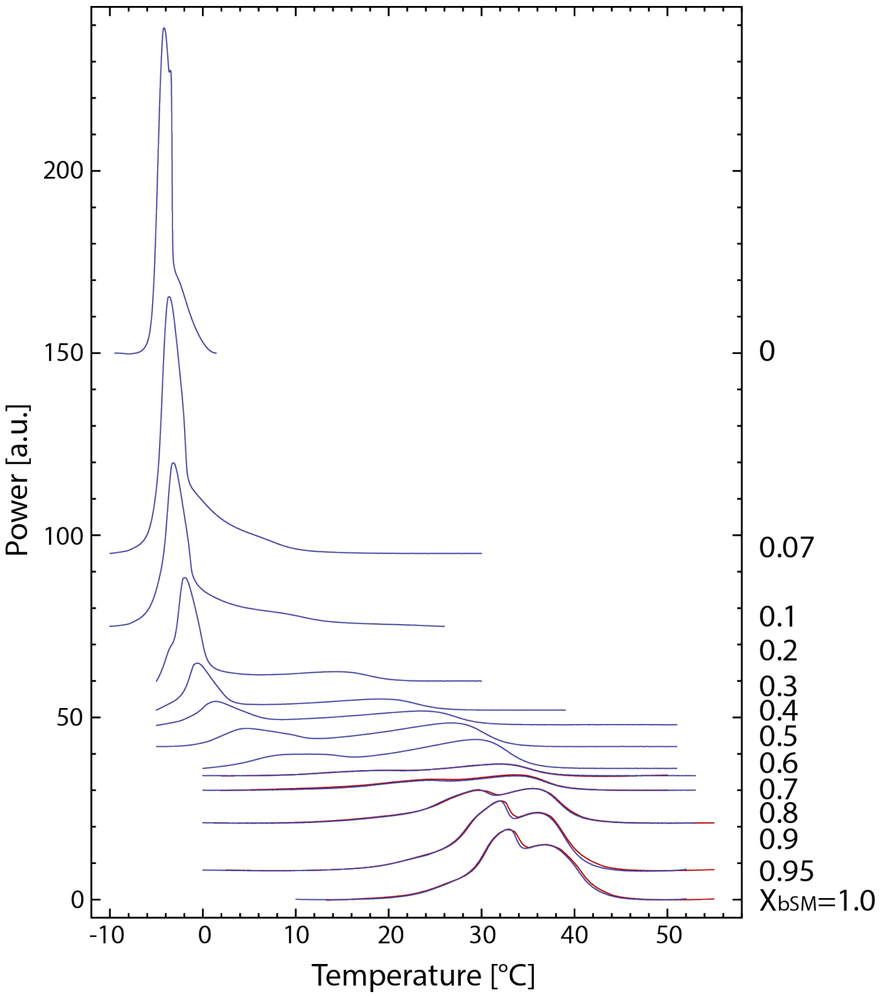

Figure B.2 DSC thermograms for bSM/POPC. Onset and completion temperatures for each sample were determined from heating (red) and cooling (blue) scans. Scans include χ_{bSM}= 0, 0.07, 0.1, 0.2, 0.3, 0.4, 0.5, 0.6, 0.7, 0.8, 0.9, 0.95, and 1.0 from top to bottom, offset for better viewing. These thermograms were used to construct the phase diagram shown in Fig. 2.5 (squares).

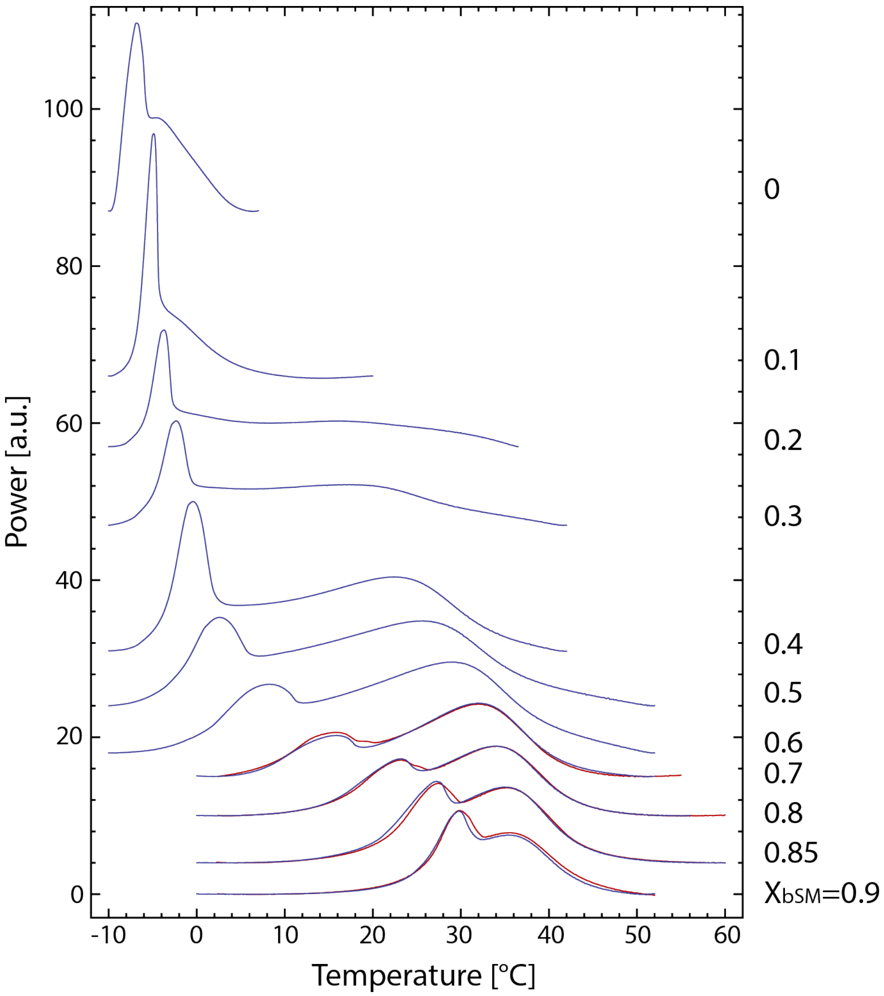

Figure B.3 DSC thermograms for bSM/POPC with 10 mol% Chol. Onset and completion temperatures for each sample were determined from heating (red) and cooling (blue) scans. Scans include χ_{bSM}= 0, 0.1, 0.2, 0.3, 0.4, 0.5, 0.6, 0.7, 0.8, 0.85, and 0.9 from top to bottom, offset for better viewing. These thermograms were used to construct the phase diagram shown in Fig. 2.5 (circles).

B.3 References

[1] E.B. Ferreira, M.L. Lima, E.D. Zanotto, DSC Method for Determining the Liquidus Temperature of Glass-Forming Systems, Journal of the American Ceramic Society, 93 (2010) 3757–3763.

[2] D.M. Price, Temperature Calibration of Differential Scanning Calorimeters, Journal of Thermal Analysis, 45 (1995) 1285–1296.

[3] R.N.A.H. Lewis, D.A. Mannock, R.N. McElhaney, Differential Scanning Calorimetry in the Study of Lipid Phase Transitions in Model and Biological Membranes: Practical Considerations, Methods in Molecular Biology, Methods in Membrane Lipids, 400 (2007) 171–195.

[4] M. Kodama, M. Kuwabara, S. Seki, Successive Phase-Transition Phenomena and Phase Diagram of the Phosphatidylcholine-Water System as Revealed by Differential Scanning Calorimetry, Biochimica Et Biophysica Acta, 689 (1982) 567–570.

Appendix C
Small-Angle Neutron Scattering

This Appendix accompanies Chapter 2.

C.1 SANS Experiment Methodology

SANS is a probe-free technique uniquely capable of characterizing nanometer-scale lateral heterogeneity in freely suspended lipid vesicles. SANS was used to investigate liquid phase separation in SM/DOPC/Chol and SM/POPC/Chol using the methodology of Pencer et al. [1]. Briefly, lipid phase separation is driven by the immiscibility of saturated and unsaturated acyl chains. Domains are detected when a difference in scattering length density (SLD) exists between the coexisting phases. Since the SLDs of lipids and cholesterol are similar without deuteration, contrast is achieved by deuterating the saturated acyl chain of one component. In these experiments, the deuterated component was PSM-d31 (dPSM) or POPC-d31 (dPOPC).

The ratio of deuterated to non-deuterated lipid, as well as the D_2O/H_2O ratio for the solvent, were adjusted such that the mean SLD of the average bilayer composition matched the solvent SLD at high temperature. Figure C.1 shows a schematic diagram of the experiment. In these experiments, the ratio of deuterated to total lipid was 94/100 for dPSM/DOPC/Chol = 0.40/0.43/0.17 (Fig. 2.7, downward-pointing triangles) and 0.54/0.20/0.26 (Fig. 2.7, upward-pointing triangles) and 100/100 in all other cases. At high temperature, the lipids in the bilayer are randomly mixed, resulting in zero contrast between the bilayer and solvent. No scattering is observed at these contrast matching conditions. As the temperature is lowered, phase separation due to segregation of saturated and unsaturated acyl chains into membrane domains results in a scattering signal from lateral SLD fluctuations. Aside from the contrast series described below, all measurements were performed under contrast matching conditions.

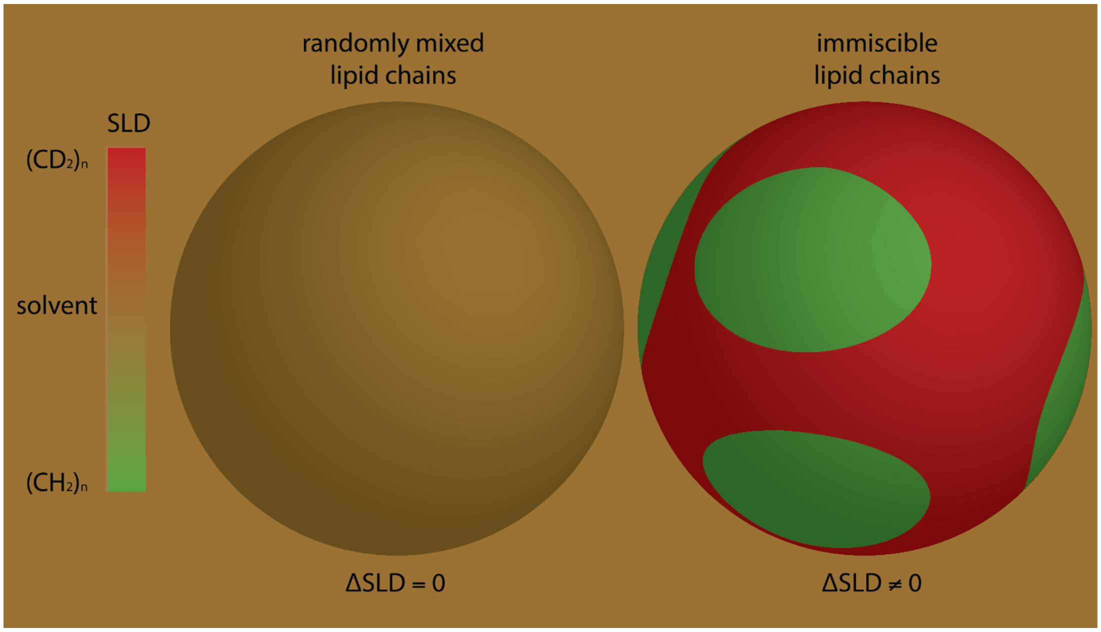

Figure C.1 Schematic of SANS contrast matching experiment. Lipid phase separation into coexisting domains results in segregation of lipids with saturated (*e.g.*, palmitoyl) and unsaturated (*e.g.*, oleoyl) acyl chains. A scattering length density (SLD) difference between the coexisting phases is required for domain detection via SANS. Contrast is achieved by perdeuterating the palmitoyl chain of PSM or POPC, resulting in a significantly higher SLD than protiated bSM, DOPC, or POPC. ULVs are used to depict differences in contrast observed as a function of temperature. *Left*, the SLD of the aqueous medium is matched to the average SLD of the bilayer such that no contrast is detected throughout the sample at high temperature, where the lipids are randomly mixed within the plane of the bilayer (ΔSLD = 0). *Right*, SLD fluctuations within the plane of the bilayer give rise to an SLD difference between the aqueous medium and the acyl chain region of the ULV such that scattering is detected at lower temperatures where phase separation of saturated and unsaturated chains occurs.

C.2 Contrast Matching Conditions: Experimental Series

Contrast matching calculations for lipid and aqueous solvent were performed as described previously [1]. The SLD of each lipid molecule was calculated using the neutron coherent scattering lengths for their constituent atoms [2] and lipid molecular volumes, and are shown in Table C.1:

Table C.1 Neutron scattering lengths (*b*), molecular volumes (*V*) at 45°C, and corresponding scattering length densities (SLD) of species relevant to this study.

Molecule	Chemical Formula	*b* [fm]	*V* [Å^3]	SLD [fm/ Å^3]
PC headgroup	$C_{10}H_{18}NO_8P$	60.1	331[a]	0.181
SM headgroup	$C_9H_{19}N_2O_6P$	47.4	331[b]	0.143
bSM chains (18:0 SM)	$C_{32}H_{64}$	-26.6	856[c]	-0.031
PSM chains (16:0 SM)	$C_{30}H_{60}$	-24.96	856[c]	-0.029
PSMd31 chains	$C_{30}\ H_{29}D_{31}$	297.75	856[c]	0.348
DOPC chains	$C_{34}H_{66}$	-20.8	988[d]	-0.021
POPC chains	$C_{32}H_{64}$	-26.6	939[e]	-0.028
POPCd31 chains	$C_{32}H_{33}\ D_{31}$	296.1	939[e]	0.315
cholesterol	$C_{27}H_{46}O$	13.3	629[f]	0.021
water	H_2O	-1.68	30.4	-0.055
heavy water	D_2O	19.15	30.5	0.628
33.9% heavy water	$H_{1.32}D_{0.68}O$	5.38	30.4	0.177
28.0% heavy water	$H_{1.44}D_{0.56}O$	4.15	30.4	0.137
27.6% heavy water	$H_{1.45}D_{0.55}O$	4.07	30.4	0.134
26.0% heavy water	$H_{1.48}D_{0.52}O$	3.74	30.4	0.123
18.8% heavy water	$H_{1.62}D_{0.38}O$	2.24	30.4	0.074

[a] [3]

[b] Assumed SM headgroup volume similar to PC headgroup volume.

[c] Determined bSM molecular volume 1187 Å^3 from [4].

[d] [5]

[e] [6]

[f] [4]

In some cases, molecular volumes at 45°C were extrapolated from linear fits to lower temperature data. PSM-d31 and POPC-d31 molecular volumes were taken to be equivalent to their protiated analogues. As the calculated bilayer SLD was found to be relatively insensitive to SM molecular volumes between 1050 and 1200 $Å^3$, a value of 1187 $Å^3$ was used for both bSM and PSM.

The solvent D_2O/H_2O contrast match conditions were confirmed experimentally, and found to be within 1.5% of calculated values. Replicates of the lipid mixture were prepared with different D_2O/H_2O solvent ratios. Scattering curves were then measured at high temperature (55°C), where the bilayer exists in a homogenous, randomly mixed fluid phase. The incoherent background was estimated from the region $0.05 < q < 0.10$ $Å^{-1}$. Plots of the incoherent background *vs.* D_2O fraction yielded a roughly linearly decreasing curve. A line was fit to the three points centered at the calculated contrast match point to determine the incoherent background contributions to the scattering for all samples measured. This incoherent background was then subtracted from each scattering curve. The integrated intensity for each curve was then plotted as a function of D_2O fraction and fit to a quadratic function, as shown in Figure C.2:

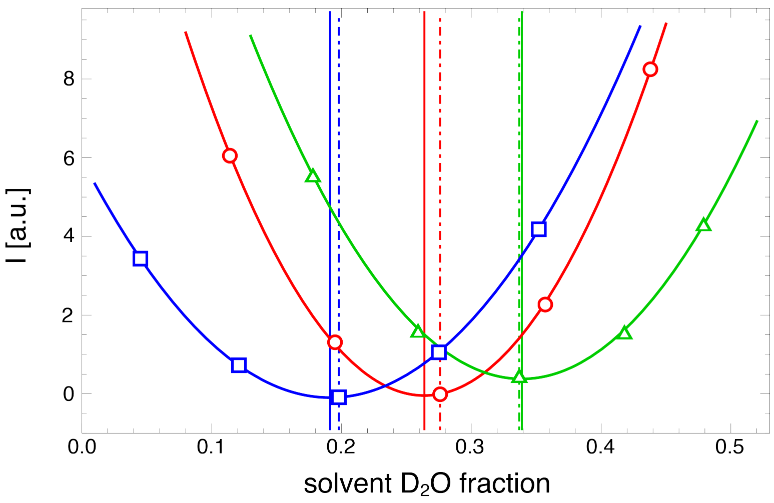

Figure C.2 SANS contrast match series performed at 55°C. Contrast match points were determined experimentally for dPSM/DOPC/Chol = 0.54/0.20/0.26 (triangles), bSM/dPOPC/Chol = 0.54/0.20/0.26 (squares), and bSM/dPOPC/Chol = 0.375/0.375/0.25 (circles). Dashed lines indicate calculated contrast match points; solid lines were obtained by fitting the experimental data points to a parabola. Sample compositions, SLD values, and contrast match conditions are listed in Table C.2. Scattering curves for these contrast matched samples appear in Fig. 2.7.

The minimum value of the best-fit quadratic function was taken as the contrast match point (Table C.2). For each composition, the calculated and experimental contrast match D_2O fractions are in good agreement. The solvent D_2O fraction was adjusted to the experimental value for each sample before measurements investigating lateral heterogeneity at lower temperatures.

Table C.2 Sample compositions, scattering length densities (SLD), and contrast match conditions for samples from Fig. 2.8. Colors correspond to trace colors in Figs. 2.7 and C.2.

$\chi_{\mathbf{PSM}}$	$\chi_{\mathbf{bSM}}$	$\chi_{\mathbf{DOPC}}$	$\chi_{\mathbf{POPC}}$	$\chi_{\mathbf{Chol}}$	**SLD**[c]	$\mathbf{f_{D20}}$[d]
0.54[a]	-	0.20	-	0.26	0.175	0.339
0.40[a]	-	0.43	-	0.17	0.137	0.28
-	0.54	-	0.20[b]	0.26	0.081	0.188
-	0.375	-	0.375[b]	0.25	0.134	0.261

[a] The %PSMd31 is 94%.

[b] The %POPCd31 is 100%.

[c] Average bilayer scattering length density (SLD) in fm/A^3 at 45°C.

[d] Fraction of D_20 in the D_2O/H_2O aqueous medium.

C.3 Total Scattered Intensity

The total scattered intensity $Q=\int Iq^2dq$ provides a quantitative measure of lateral segregation [7]. For the type of contrast matched samples described here, Q takes on relatively low values at temperatures where the bilayer is randomly mixed, but increases at temperatures where the sample is phase separated. Plotting Q as a function of temperature therefore yields an estimate of the miscibility transition temperature. Since this method compares scattering at different temperatures, it is important to properly subtract the incoherent background at each temperature. Indeed, the incoherent background in many cases was observed to increase with temperature. As described above for the contrast series measurements, the incoherent background was estimated from the high-q region and subtracted from each sample measurement. The total scattered intensity was then determined by integrating over the same q range at each temperature. The calculated Q values for samples listed in Table C.3 are shown in Fig. 2.8 of the main text. The corresponding scattering curves are shown in Fig. C.3:

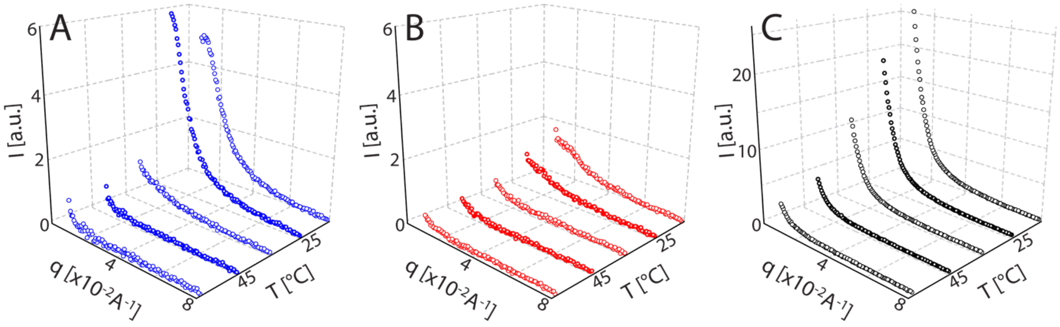

Figure C.3 SANS reveals phase separation in PSM/POPC/Chol. Scattering curves for PSM/dPOPC/Chol (*A*), dPSM/POPC/Chol (*B*), and dPSM/DOPC/Chol (*C*) at 15, 25, 35, 45, and 55°C. All compositions have mole fractions 0.39/0.39/0.22. Enhanced scattering in all three samples indicates coexisting domains between 15 and 35°C. Minimal scattering at 45–55°C indicates a miscibility transition between 35–45°C for both POPC-containing samples (*A* and *B*). Residual scattering at 35 and 45°C is more significant for DOPC-containing (*C*) than for POPC-containing samples. This result is consistent with observations made with FRET. Switching the deuterated species in the mixture PSM/POPC/Chol from dPSM (*B*) to dPOPC (*A*) results in a significant increase in scattering, indicating stronger partitioning of POPC into the Ld phase, in contrast to the partitioning of PSM into Lo phase. Therefore, dPOPC should provide better contrast than dPSM for detecting domains in SM/POPC/Chol mixtures. Sample compositions, scattering length densities, and contrast match conditions are listed in Table C.3.

Table C.3 Sample compositions, scattering length densities (SLD), and contrast match conditions for samples from Figs. 2.8 and C.3. Colors correspond to Figs. 2.8 and C.3.

χ_{PSM}	$\chi_{PSM\text{-}d31}$	χ_{DOPC}	χ_{POPC}	$\chi_{POPC\text{-}d31}$	χ_{Chol}	SLD[c]	f_{D20}[d]
	0.39[a]	-	0.39	-	0.22	0.137	0.276
0.39	-	-	-	0.39[b]	0.22	0.137	0.276
-	0.39[a]	0.39	-	-	0.22	0.081	0.276

[a] The %PSMd31 is 100%.
[b] The %POPCd31 is 100%.
[c] Average bilayer scattering length density (SLD) in fm/A^3 at 45°C.
[d] Fraction of D_20 in the D_2O/H_2O aqueous medium.

C.4 References

[1] J. Pencer, T. Mills, V. Anghel, S. Krueger, R.M. Epand, J. Katsaras, Detection of submicron-sized raft-like domains in membranes by small-angle neutron scattering, The European Physical Journal E, Soft Matter, 18 (2005) 447–58.

[2] V.F. Sears, Neutron scattering lengths and cross sections, Neutron News, 3 (1992) 26–37.

[3] S. Tristram-Nagle, Y. Liu, J. Legleiter, J.F. Nagle, Structure of gel phase DMPC determined by X-ray diffraction, Biophysical Journal, 83 (2002) 3324–35.

[4] A.I. Greenwood, S. Tristram-Nagle, J.F. Nagle, Partial molecular volumes of lipids and cholesterol, Chemistry and Physics of Lipids, 143 (2006) 1–10.

[5] S. Tristram-Nagle, H.I. Petrache, J.F. Nagle, Structure and interactions of fully hydrated dioleoylphosphatidylcholine bilayers, Biophysical Journal, 75 (1998) 917–25.

[6] N. Kučerka, M.-P. Nieh, J. Katsaras, Fluid phase lipid areas and bilayer thicknesses of commonly used phosphatidylcholines as a function of temperature, Biochimica Et Biophysica Acta, 1808 (2011) 2761–71.

[7] J. Pencer, V.N.P. Anghel, N. Kučerka, J. Katsaras, Scattering from laterally heterogeneous vesicles I Model-independent analysis, Journal of Applied Crystallography, 39 (2006) 791–796.

Appendix D
Vesicle Structures and Solvent Conditions

D.1 Introduction

The four experimental techniques employed in this work (described in Chapter 2, 3, and 4) require slightly different sample preparation, including solvent conditions. We discuss vesicle structures and solvent conditions employed in Förster resonance energy transfer (FRET), differential scanning calorimetry (DSC), and small-angle neutron scattering (SANS) in Chapter 2. The vesicle structures employed in electron spin resonance (ESR) are discussed in Chapter 3. Issues regarding extrusion of vesicles to obtain unilamellar vesicles (ULV) for FRET measurements requiring consistent sample concentrations are discussed in Chapter 4.4.4. More explicit discussion of and comparison between the vesicle structures and solvent conditions employed in all four techniques in this thesis are provided in this Appendix. We also discuss solvent equilibration across multilayers.

D.2 Variants on the Bilayer Lyotropic Phase

D.2.1 Vesicle Lamellarity

Throughout the thesis, the term paucilamellar vesicle (PLV) has been substituted for the more common term multilamellar vesicle (MLV). This change was made since the average lamellarity of vesicles prepared via rapid solvent exchange (RSE) is 1.4 [1], and therefore these vesicles are more accurately described as PLV's than MLV's. In the abbreviations section of the front matter (page xvii), we define MLV's as having lamellarity >2 and PLV's as having lamellarity between 1 and 2.

This terminology is used consistently through the dissertation. MLV’s or PLV’s may be extruded to obtain ULV’s with well-defined vesicle diameter.

The lamellarity of the vesicles is related to the sample preparation method. The lamellarity is relevant for several reasons including (1) possible FRET between different bilayers, (2) equilibration of ions across bilayers, and (3) proper hydration of vesicle structures via adequate water equilibration across bilayers.

D.2.2 Probe Communication Across Bilayers

FRET data may be fit to the finite phase separation FRET (FP-FRET) model to determine the sizes of coexisting domains as described in Chapter 4. Since energy transfer via FRET is a distance-dependent effect, geometric constraints must be taken into account. In the simplest case, FRET occurs between probes in a single leaflet of the bilayer. The description can be expanded to include FRET between probes in opposite leaflets, and ultimately across different bilayers. For first efforts to produce experimental data that may be fit to the FP-FRET model, we simplified the geometry by extruding PLV’s prepared by RSE to obtain ULV’s.

D.2.3 Vesicle Hydration

Proper vesicle hydration requires adequate water equilibration across bilayers. Many studies have investigated lipid phase behavior as a function of hydration (for example, [2]). Most studies now employ fully hydrated vesicles, since these conditions better model the cell membrane.

It is possible to check for water equilibration via DSC. Without adequate hydration, the DSC signal exhibits additional peaks beyond those indicating familiar bilayer phase transitions [2]. This occurs because pockets of bilayer exist with inadequate hydration; these exhibit different transition temperatures. We compared DSC scans for vesicles prepared via two methods at three compositions in the binary system DSPC (1,2-distearoyl-*sn*-glycero-3-phosphocholine)/SOPC (1-stearoyl-2-oleoyl-*sn*-glycero-3-phosphocholine). These compositions included DSPC/SOPC 0/1, 0.5/0.5, and 1/0 in order to span a range of phase transition temperatures. The two vesicle preparation methods included (1) RSE and (2) dry film hydration followed by five freeze/thaw cycles. Even on the first DSC scan, the only peaks present were those due to familiar bilayer phase transitions. This indicates that samples prepared by both methods were adequately hydrated and equilibrated prior to measurement.

We were also able to check for sample heterogeneity due to inadequate hydration via ESR. In all ternary lipid systems examined via ESR (Chapter 3), we examined a control trajectory that passes through the one-phase region and exhibits a continuous, gradual change in phase properties between liquid-disordered (Ld) and liquid-ordered (Lo) phases. ESR spectra for samples along these trajectories were always fit by one order parameter, consistent with homogeneity and equilibration of water across the lipid multilayers.

In the studies described in this dissertation, we used RSE to prepare vesicles for FRET and DSC, and we used dry film hydration followed by freeze/thaw to prepare vesicles for ESR and SANS. Our DSC and ESR results indicate that all lipid samples exhibited adequate hydration. In future studies, it will be possible and preferable to prepare all PLV samples via RSE.

D.2.4 Vesicle Size

For the SANS studies described in Chapter 2, MLV's prepared via dry film hydration and freeze/thaw were extruded to produce ULV's with 60 nm diameter. For some of the FRET studies described in Chapter 4, PLV's prepared by RSE were extruded to produce ULV's with 100 nm diameter. For all other studies, vesicles were employed as PLV's. For SANS, extrusion was necessary to avoid complication of the measured scattering intensity by the interparticle structure factor [3]. For FRET in Chapter 4, ULV's were required to simplify geometry for the FP-FRET model (as discussed in Chapter 4 and Appendix D2.2).

Extruding vesicles to small diameter increases the bilayer curvature, which certainly has an effect on the sizes of detected coexisting phase domains and may also have additional effects on membrane phase behavior [4]. As discussed in Chapter 6.2, we plan to investigate the influence of vesicle size on membrane phase behavior using FRET and SANS.

D.3 Solvent Conditions

Where possible, bilayer samples were prepared under physiological buffer conditions (200 mM KCl, 5 mM PIPES, and 1 mM EDTA at pH 7.0). This was possible for FRET samples. Limitations for ESR, DSC, and SANS are discussed below. Discussion of the influence of solvent conditions on membrane phase behavior follows.

D.3.1 Solvent Condition Limitations

D.3.1.1 Electron Spin Resonance (ESR)

For ESR, excess water attenuates the measured ESR signal. Therefore, it was necessary to pellet lipid samples by centrifugation before measurement. For the mixtures examined, the samples most difficult to pellet included low-melting lipids with ~10 mol% cholesterol (Chol). These samples could be pelleted in buffer of reduced ionic strength (10 mM KCl, 5 mM PIPES, and 1 mM EDTA at pH 7.0). Lowering the ionic strength reduced the density of the solvent, enabling the sample to be pelleted by making the solvent density lower than the lipid density.

D.3.1.2 Differential Scanning Calorimetry (DSC)

For DSC, higher concentration samples yield peaks of greater intensity. It was especially important to maximize intensity for the compositions explored in these studies because the DSC signal is broad for lipid mixtures. In the DSC studies described in Chapter 2, the high-melting lipid bSM (brain-sphingolymelin) is itself a mixture exhibiting a broad transition. Further, coexisting Ld and gel (Lβ) phases broaden the DSC signal. Finally, addition of Chol further broadens the DSC signal.

DSC samples were prepared by RSE. This vesicle preparation technique has an empirically determined maximum concentration. Above this maximum lipid concentration, it is not possible to complete the solvent exchange process without loss of lipid sample due to foaming. This issue is avoided by performing RSE at lipid concentrations below 2 mg/mL. Therefore, the RSE process was carried out on dilute lipid mixtures. Samples were then pelleted by centrifugation, and the supernatant was removed to concentrate the PLV sample. For samples with significant fractions of low-melting lipids, it was not possible to pellet the samples in physiological buffer conditions. The samples most difficult to pellet included low-melting lipids with 0% Chol. The ionic strength of the solvent had to be lowered to zero in order to pellet these samples. Zero ionic strength (water) was then used for all DSC samples.

D.3.1.3 Small-Angle Neutron Scattering (SANS)

The contrast-matching technique used to conduct the SANS experiments described in Chapter 2 requires a solvent mixture of H_2O and D_2O. It was important to match the scattering length density of the solvent to the mean bilayer scattering length density. It is difficult to do so if additional components were added to the solvent to achieve physiological buffer conditions. Therefore, zero ionic strength (water) was used for all SANS samples.

D.3.2 Solvent Effects on Membrane Phase Behavior

To construct phase diagrams by compiling results from techniques requiring samples in solvents of different ionic strengths, it is important to understand the degree to which solvent conditions influence phase boundaries. Examples of studies conducted with mixtures of neutral lipids under different solvent conditions are discussed below.

D.3.2.1 Phase Boundaries Agree for Neutral Lipid Mixtures in Various Solvent Conditions

Several studies in our lab have confirmed that samples prepared at zero ionic strength exhibit the same phase boundaries as samples prepared in physiological buffer conditions for neutral lipids like those employed in this thesis.

1. Observations were made for DSPC (1,2-distearoyl-*sn*-glycero-3-phosphocholine)/DOPC (1,2-dioleoyl-*sn*-glycero-3-phosphocholine)/Chol and DSPC/POPC (1-palmitoyl-2-oleoyl-*sn*-glycero-3-phosphocholine)/Chol [5]. In these studies, over 500 giant unilamellar vesicles (GUV's) were prepared at zero ionic strength, and an additional 500 GUV's were prepared in physiological buffer conditions. Phase boundaries determined by examining these GUV's with fluorescence microscopy were in agreement for both solvent conditions. In addition, the phase boundaries determined in these fluorescence microscopy studies agreed with phase boundaries determined via fluorescence spectroscopy measurements on PLV's prepared in physiological buffer by RSE.

2. Further observations were made for DSPC/DOPC/Chol, DSPC/POPC/Chol, and DSPC/SOPC/Chol using FRET and ESR. In experiments similar to those described in Chapters 2 and 3, physiological buffer was employed for FRET studies, and lower ionic strength was used for ESR studies. Phase boundaries determined using these two techniques are in excellent agreement [6].

3. Similar observations were made for DPPC (1,2-dipalmitoyl-*sn*-glycero-3-phosphocholine)/DLPC (1,2-dilauroyl-*sn*-glycero-3-phosphocholine) /Chol: phase boundaries coincided for fluorescence microscopy of GUV's from zero up to 100 mM ionic strength, and these phase boundaries were additionally in agreement with those determined via via fluorescence spectroscopy for vesicles with 200 mM ionic strength [7].

D.3.2.2 Phase Boundaries May Vary with Solvent Conditions in Some Cases

Solvent conditions may affect phase boundaries for mixtures containing negatively charged lipids and near the gel/fluid transition for neutral lipids. For mixtures containing negatively charged lipids, the change in the gel/fluid transition temperature is only a few degrees when monovalent cations are employed in the solvent [8,9]. For neutral lipids such as DPPC, the gel/fluid transition temperature may change by a degree or two (Celsius) in 1M salt compared to zero ionic strength [10].

D.4 References

[1] J.T. Buboltz, G.W. Feigenson, A novel strategy for the preparation of liposomes: rapid solvent exchange, Biochimica Et Biophysica Acta, 1417 (1999) 232–45.

[2] G.G. Shipley, L.S. Avecilla, D.M. Small, Phase behavior and structure of aqueous dispersions of sphingomyelin, Journal of Lipid Research, 15 (1974) 124–31.

[3] J. Pan, F.A. Heberle, R.S. Petruzielo, J. Katsaras, The Usage of Small-Angle Neutron Scattering in Exploiting Nanoscopic Lipid Domains, Chemistry and Physics of Lipids, (2013).

[4] N. Kucerka, J. Pencer, J.N. Sachs, J.F. Nagle, J. Katsaras, Curvature effect on the structure of phospholipid bilayers, Langmuir, 23 (2007) 1292–9.

[5] J. Zhao, J. Wu, F.A. Heberle, T.T. Mills, P. Klawitter, G. Huang, G. Costanza, G.W. Feigenson, Phase studies of model biomembranes: complex behavior of DSPC/DOPC/cholesterol, Biochimica Et Biophysica Acta, 1768 (2007) 2764–76.

[6] F.A. Heberle, J. Wu, S.L. Goh, R.S. Petruzielo, G.W. Feigenson, Comparison of three ternary lipid bilayer mixtures: FRET and ESR reveal nanodomains, Biophysical Journal, 99 (2010) 3309–3318.

[7] G.W. Feigenson, J.T. Buboltz, Ternary Phase Diagram of Dipalmitoyl-PC/Dilauroyl-PC/Cholesterol: Nanoscopic Domain Formation Driven by Cholesterol, Biophysical Journal, 80 (2001) 2775–2788.

[8] A.C. Cowley, N.L. Fuller, R.P. Rand, V.A. Parsegian, Measurement of repulsive forces between charged phospholipid bilayers, Biochemistry, 17 (1978) 3163–8.

[9] G. Feigenson, On the Nature of Calcium Ion Binding between Phosphatidylserine Lamellae, Biochemistry, 25 (1986) 5819–5825.

[10] R.P. Rand, V.A. Parsegian, J.A. Henry, L.J. Lis, M. McAlister, The effect of cholesterol on measured interaction and compressibility of dipalmitoylphosphatidylcholine bilayers, Canadian Journal of Biochemistry, 58 (1980) 959–68.

Appendix E
Experimental Detection of Nanoscale Heterogeneity and Critical Fluctuations

E.1 Phase Separation Terminology

In this thesis, we use the terminology of phase separation in describing liquid heterogeneity detected in lipid mixtures modeling the cell membrane. To avoid confusion, we point out that the classical definition of phase separation in statistical mechanics describes coexisting phases as macroscopic and separated by a well-defined boundary [1]. In particular, 'A phase is a part of a system, uniform throughout in chemical composition and physical properties, which is separated from other homogeneous parts of the system by boundary surfaces' [2]. The properties that are uniform throughout the extent of the phase exhibit an infinite correlation length. For example, the density is constant throughout a fluid phase, the magnetization is constant in the Ising model, and concentration of the various lipid components is uniform throughout the liquid-ordered (Lo) phase.

What terminology is useful for describing liquid heterogeneity on small size scales? The terminology of phase separation has proven especially useful in describing nanoscale heterogeneity, even though domains this small do not meet the classical definition of phase separation in statistical mechanics.

Nevertheless, others have found that related mixtures exhibit continuous nano- to macroscopic domain size transitions [3]. In work directly following from this thesis, we have used small-angle neutron scattering (SANS) to confirm continuous domain size transitions between the ternary mixtures sphingomyelin (SM)/DOPC (1,2-dioleoyl-*sn*-glycero-3-phosphocholine)/cholesterol (Chol) and SM/POPC (1-

palmitoyl-2-oleoyl-*sn*-glycero-3-phosphocholine)/Chol using an approach developed by Heberle and coworkers [4].

An important conclusion of this thesis is the confirmation of coexisting domains on the order of 2-7 nm (25-300 nm lipids per leaflet) in ternary lipid mixtures. The existence of these domains is confirmed by several techniques (Chapters 2-3). Experimental results from this thesis are important inputs for theoretical models that aim to explain why nanoscale domains are stable and do not coalesce into macroscopic phases.

E.2 Overview

We discuss experimental methods that have been used to detect critical fluctuations in lipid mixtures. We provide background on detection of critical fluctuations in systems exhibiting liquid-disordered (Ld) and liquid-ordered (Lo) phase coexistence. We elaborate on the use of techniques employed in this thesis for future evaluation of critical fluctuations in lipid mixtures.

E.3 Experimental Detection of Critical Fluctuations

A review of experimental detection of critical fluctuations in two-dimensional systems reveals many instances in which these fluctuations are shown to be consistent with predictions of the Ising model in two-dimensions [5]. In these experiments, temperature-dependent measurements of order parameter, line tension, correlation length, or heat capacity are made in order to quantitatively determine critical exponents ν and β. Comparison is then made between critical exponents determined experimentally and those predicted by various theoretical models.

Experimental conditions needed for detecting critical fluctuations include extremely sensitive temperature control, with some estimates indicating temperature fluctuations greater than 0.05 K [5] or even 0.005 K [6] may not be tolerated. Therefore, strict evaluation of the data presented in thesis in terms of the Ising model is impossible because the experiments were not designed to be performed under temperature control conditions in which critical exponents may be determined.

E.3.1 Systems Exhibiting Macroscopic Phase Coexistence

Critical fluctuations have been detected directly in systems exhibiting macroscopic Ld+Lo phase coexistence. A region of two-phase coexistence must be bounded by a region of one- or three-phase coexistence unless the two-phase region extends to a binary axis on the phase diagram [7]. Many ternary phase diagrams for lipid mixtures modeling the outer leaflet of the cell membrane exhibit a region of Ld+Lo phase coexistence that connects to a one-phase region. In this case, the Ld+Lo coexistence region must terminate in a critical point.

The tielines in the Ld+Lo coexistence region become shorter as the compositions of the coexisting phases become more similar approaching the critical point. It is therefore possible to estimate the position of the critical point through accurate knowledge of the phase diagram at a given temperature [8]. For systems exhibiting macroscopic Ld+Lo phase coexistence, the connectivity of the coexisting phases is observed to switch at the percolation threshold (discussed in Chapter 4.3.3.2). That is, Lo domains within surrounding Ld phase are observed for compositions closer to the Ld boundary, while Ld domains within surrounding Lo phase are observed on the opposite side of the Ld+Lo region. At the percolation threshold, both phases are observed to be continuous. The percolation threshold can be determined experimentally as a function of lipid composition at constant temperature within the phase coexistence region. The percolation threshold terminates in the critical point at the upper boundary of the Ld+Lo phase coexistence region.

For example, fluorescence microscopy of GUV's has been used to determine the percolation threshold and critical point at room temperature in the ternary lipid mixture DSPC (1,2-distearoyl-*sn*-glycero-3-phosphocholine)/DOPC/ Chol [9]. Further, micropipette aspiration was used to determine the line tension at the domain boundaries between coexisting Ld+Lo phases along the percolation threshold approaching the critical point in eSM (egg sphingomyelin)/DOPC/Chol [8].

Critical phenomena in bilayer lipid mixtures is characterized by low line tension and composition fluctuations. In ternary lipid mixtures exhibiting macroscopic phase coexistence, it is possible to directly measure line tension via techniques including micropipette aspiration [8] or calculate line tension from analysis of domain boundary fluctuations [5] via fluorescence microscopy of giant unilamellar vesicles (GUV). Extrapolation from these experiments suggests that line tension decreases to zero as a critical point is approached in composition space at constant temperature.

Domain boundary fluctuations also provide evidence of fluctuations about the average lipid composition. As discussed by Honerkamp-Smith and coworkers, these compositional fluctuations are quantified by the two-point correlation function, which is used to obtain the structure factor. They rescaled the experimental structure factor by the correlation length over which the fluctuations persist in order to fit predictions of the two-dimensional Ising model [5]. Scattering data may be analyzed to determine correlation lengths using this approach, as discussed below in Appendix E.3.3.2.

Spectroscopic techniques including NMR [10] and electron spin resonance (ESR) [7,11] have also been used to infer critical fluctuations. These methods are useful for detecting heterogeneity on length scales below optical resolution.

E.3.2 Systems Exhibiting Nanoscale Heterogeneity

There is considerable interest in understanding the mechanisms responsible for nanoscale heterogeneity. Line tension favors minimization of the interface between coexisting liquid domains. Perimeter decreases as domains grow in size. However, more biologically relevant lipid mixtures as well as the cellular plasma membrane exhibit nanoscale heterogeneity on the order of 2 to 200 nm (as discussed in Chapter 1). Several lines of inquiry are being pursued to determine the mechanisms responsible for the maintenance of nanoscale heterogeneity. Experimental observations and methods are described below and in Appendix E.3.3.

Phase diagrams for ternary lipid mixtures exhibiting coexisting nanoscale phase domains have been reported, and critical points have been inferred using spectroscopic techniques with nanoscale resolution (as discussed in Chapter 1.5.2). Considerable disagreement has existed regarding the phase boundaries and the sizes of coexisting domains in some of these mixtures, suggesting difficulty in distinguishing between heterogeneity within a single phase and coexisting phases (Chapter 2.5.4).

Our results indicate that careful consideration of the spatial resolution of the techniques employed (Chapter 2.5.4, Fig. 2.9*A*) and attention to the effects of impurities enable these disparate results to be interpreted within the context of the bSM (porcine brain sphingomyelin)/POPC/Chol phase diagram we have constructed via Förster resonance energy transfer (FRET) and differential scanning calorimetry (DSC) measurements (Fig. 2.6).

Further, our use of complementary techniques with different spatial detection limits have enabled us to provide a model-independent estimate of the size of coexisting liquid domains between 2 and 7 nm radius (25 to 300 lipids per leaflet). Some disagreement exists as to whether domains of this size constitute phase domains or are better termed as clusters or fluctuations. Interpreting these heterogeneities as phase domains permits the use of phase rules in determining the compositions of coexisting phases, which in turn provides more experimental inputs for theoretical models being developed to explain the mechanisms responsible for nanoscale heterogeneity.

Our future studies are aimed at determining the sizes of coexisting domains as a function of composition and temperature via FRET (Chapter 4) and SANS (Chapter 5.2). With sufficiently precise temperature control, SANS may be employed to explore critical fluctuations (Appendix E.3.3.2).

E.3.3 Systems Examined and Methods Employed in This Dissertation

Our FRET and DSC studies enabled us to construct phase diagrams for two ternary lipid systems including bSM/DOPC/Chol and bSM/POPC/Chol (Fig. 2.6). The critical point for bSM/DOPC/Chol was inferred from enhanced FRET in single-phase compositions just above the Ld+Lo region that persists at 45°C (Fig. A.1). The location of the critical point determined via FRET is consistent with the critical point inferred from geometric considerations including reasonable extrapolation of tielines from the upper face of the three-phase triangle and the shape of the upper boundary of the Ld+Lo phase coexistence region (Appendix E.3.1). These results were used to infer the critical point composition for bSM/POPC/Chol, which exhibits similar phase boundaries to bSM/DOPC/Chol (Fig. 2.6).

In addition, ESR and SANS are two techniques used in this thesis which have been employed by others to investigate critical fluctuations in lipid mixtures [7,11–14]. For this reason, we comment here as to how critical fluctuations could be detected using the ESR and SANS methods presented in Chapters 2 and 3.

E.3.3.1 Electron Spin Resonance (ESR)

ESR studies consistently report critical point compositions with greater low-melting lipid fractions than other methods [7,11]. As discussed in Chapter 2.5.2.2, this discrepancy is thought to be due to the difficulty in discerning distinct ESR spectral components from coexisting phases that have nearly identical physical properties near a critical point.

Our ESR studies (Chapter 3) included compositions above the Ld+Lo coexistence region. ESR spectra collected at these compositions are well described by single-component fits, indicating a single order parameter.

E.3.3.2 Small-Angle Neutron Scattering (SANS)

Use of SANS to investigate critical fluctuations dates back three decades to the detection of a critical point terminating a region of solid-solid coexistence within the fluid-solid coexistence region of a binary lipid mixture with equal mole fractions of DSPC and DMPC (1,2-dimyristoyl-sn-glycero-3-phosphocholine) [12]. The analysis of Knoll and coworkers included testing the Ornstein–Zernike law using measured data for scattering intensity I as a function of scattering vector q (Chapter 2). If this law holds and a correlation length is extracted, the existence of composition fluctuations on this length scale is inferred.

The Ornstein-Zernicke model describes the scattering intensity at small angles (small q values)

$$I(q) \ =\propto \frac{\xi^2}{1+q^2\xi^2}$$

where ξ is the correlation length. Plotting the inverse scattering intensity $I(q)^{-1}$ vs. the squared scattering vector q^2 tests the Ornstein-Zernicke law. Extrapolating the experimental curve to $I(q)^{-1} = 0$ on the $-q^2$ axis yields the correlation length ξ. A negative value for this x-intercept indicates critical-like composition fluctuations. A positive value for this x-intercept is interpreted to indicate that critical-like composition fluctuations are not present [13].

More recently, this analysis has been applied to investigate possible critical fluctuations in sphingomyelin-containing ternary mixtures prepared at the canonical raft composition with equal mole fractions bSM/low-melting lipid/Chol [13]. In both bSM/DOPC/Chol and bSM/POPC/Chol, no evidence of critical fluctuations was found.

We have applied this analysis to the SANS data presented in Chapter 2. For mixtures of PSM (palmitoyl sphingomyelin)/DOPC/Chol, we obtained a positive x-intercept indicating no critical fluctuations at the compositions examined. This result was expected since these compositions are not close to a critical point (Fig 2.6). For mixtures of bSM/POPC/Chol and PSM/POPC/Chol, we obtained correlation lengths on the order of the sizes of coexisting domains determined via model-dependent analysis of SANS data fit to a partitioning model for coexisting phase domains [15].

In performing these analyses, we noticed several limitations. First, experimental detection of critical fluctuations via SANS may not be possible with either of the instruments we used, since the temperature control is not more precise than 1 K. Second, the correlation length obtained from a fit to the Ornstein-Zernicke model depends strongly on the range of q values over which the model is applied. Both previous studies [12,13] measured minimum q values a factor of 10 lower in magnitude than the q values accessible in our experiments. Our detection geometry was selected to maximize the neutron flux on our sample and thereby sacrificed detection at lower q values. Future studies aimed at testing the Ornstein-Zernicke model should employ more precise temperature control and extend the detection range to lower q values. In contrast, sufficient data was acquired for performing domain size analysis assuming coexisting liquid domains.

E.4 References

[1] J.P. Sethna, Statistical Mechamics: Entropy, Order Parameters, and Complexity, Clarendon Press, Oxford, UK, 2011.

[2] F. Daniels, R.A. Alberty, Physical Chemistry, Third, John Wiley & Sons, Inc., New York, 1961.

[3] T.M. Konyakhina, J. Wu, J.D. Mastroianni, F.A. Heberle, G.W. Feigenson, Phase Diagram of a Four-Component Lipid Mixture: DSPC/DOPC/POPC/Chol, Submitted, (2012).

[4] F.A. Heberle, R.S. Petruzielo, J. Pan, P. Drazba, N. Kucerka, R.F. Standaert, G.W. Feigenson, J. Katsaras, Bilayer thickness mismatch controls raft size in model membranes, Submitted, (2012).

[5] A.R. Honerkamp-Smith, P. Cicuta, M.D. Collins, S.L. Veatch, M. den Nijs, M. Schick, S.L. Keller, Line tensions, correlation lengths, and critical exponents in lipid membranes near critical points, Biophysical Journal, 95 (2008) 236–46.

[6] E.R. Farkas, W.W. Webb, Precise and millidegree stable temperature control for fluorescence imaging: application to phase transitions in lipid membranes, The Review of Scientific Instruments, 81 (2010) 093704.

[7] A.K. Smith, J.H. Freed, The Determination of Tie-Line Fields for Coexisting Lipid Phases: an ESR Study, Journal of Physical Chemistry B, 113 (2009) 3957–3971.

[8] A. Tian, C. Johnson, W. Wang, T. Baumgart, Line Tension at Fluid Membrane Domain Boundaries Measured by Micropipette Aspiration, Physical Review Letters, 98 (2007) 18–21.

[9] F.A. Heberle, J. Wu, S.L. Goh, R.S. Petruzielo, G.W. Feigenson, Comparison of three ternary lipid bilayer mixtures: FRET and ESR reveal nanodomains, Biophysical Journal, 99 (2010) 3309–3318.

[10] S.L. Veatch, O. Soubias, S.L. Keller, K. Gawrisch, Critical fluctuations in domain-forming lipid mixtures, Proceedings of the National Academy of Sciences, 104 (2007) 17650–5.

[11] I. V. Ionova, V.A. Livshits, D. Marsh, Phase Diagram of Ternary Cholesterol/ Palmitoylsphingomyelin/ Palmitoyloleoyl-Phosphatidylcholine Mixtures: Spin-Label EPR Study of Lipid-Raft Formation, Biophysical Journal, 102 (2012) 1856–1865.

[12] W. Knoll, G. Schmidt, E. Sackmann, K. Ibel, Critical demixing in fluid bilayers of phospholipid mixtures A neutron diffraction study, The Journal of Chemical Physics, 79 (1983) 3439.

[13] C. Nicolini, P. Thiyagarajan, R. Winter, Small-scale composition fluctuations and microdomain formation in lipid raft models as revealed by small-angle neutron scattering, Physical Chemistry Chemical Physics, 6 (2004) 5531.

[14] K. Vogtt, C. Jeworrek, V.M. Garamus, R. Winter, Microdomains in lipid vesicles: structure and distribution assessed by small-angle neutron scattering, The Journal of Physical Chemistry B, 114 (2010) 5643–8.

[15] J. Pan, F.A. Heberle, R.S. Petruzielo, J. Katsaras, The Usage of Small-Angle Neutron Scattering in Exploiting Nanoscopic Lipid Domains, Chemistry and Physics of Lipids, (2013).